AD-A031 212

A Specular Chamber for Off-Axis Response Evaluations of High-Rejection Optical Baffling Systems

Utah State Univ Logan Electro-Dynamics Lab

1 Jun 76

303089

AFGL-TR-76-0144

ADA031212

A SPECULAR CHAMBER FOR OFF-AXIS RESPONSE EVALUATIONS
OF HIGH-REJECTION OPTICAL BAFFLING SYSTEMS

John C. Kemp and Clair L. Wyatt

Electro-Dynamics Laboratories
Utah State University
Logan, Utah 84322

1 June 1976

Scientific Report No. 4

Approved for public release; distribution unlimited

AIR FORCE GEOPHYSICS LABORATORY
AIR FORCE SYSTEMS COMMAND
UNITED STATES AIR FORCE
HANSCOM AFB, MASSACHUSETTS 01731
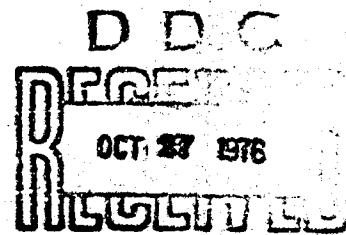
D D C

OCT 27 1976

REPORT DOCUMENTATION PAGE	READ INSTRUCTIONS BEFORE COMPLETING FORM

1 REPORT NUMBER	2. GOVT ACCESSION NO.	3. RECIPIENT'S CATALOG NUMBER
AFGL-TR-76-0144		

4. TITLE (and Subtitle)	5. TYPE OF REPORT & PERIOD COVERED
A SPECULAR CHAMBER FOR OFF-AXIS RESPONSE EVALUATIONS OF HIGH-REJECTION OPTICAL BAFFLING SYSTEMS	Scientific Report #4
	6. PERFORMING ORG. REPORT NUMBER

7. AUTHOR(s)	8. CONTRACT OR GRANT NUMBER(s)
John C. Kemp and Clair L. Wyatt	F19628-73-C-0048

9. PERFORMING ORGANIZATION NAME AND ADDRESS	10. PROGRAM ELEMENT, PROJECT, TASK AREA & WORK UNIT NUMBERS
Electro-Dynamics Laboratories Utah State University Logan, Utah 84322	P.E. 62710H, Proj:K11BAX HX534, Work Unit 10 CDNA-00-10

11. CONTROLLING OFFICE NAME AND ADDRESS	12. REPORT DATE
Air Force Geophysics Laboratory Hanscom AFB, Massachusetts 01731 Monitor/A. T. Stair /OPR	1 June 1976
	13. NUMBER OF PAGES
	116

14. MONITORING AGENCY NAME & ADDRESS(if different from Controlling Office)	15. SECURITY CLASS. (of this report)
	Unclassified
	15a. DECLASSIFICATION DOWNGRADING SCHEDULE

16. DISTRIBUTION STATEMENT (of this Report)

Approved for Public Release, distribution unlimited.

17. DISTRIBUTION STATEMENT (of the abstract entered in Block 20, if different from Report)

18. SUPPLEMENTARY NOTES

This research was sponsored by the Defense Nuclear Agency under
Subtask K11BAXHX534, Work Unit 10
Entitled: Infrared Instrument Development and Certification

19. KEY WORDS (Continue on reverse side if necessary and identify by block number)

Baffle, optical baffle, calibration, off-axis response, atmospheric scattering, atmospheric measurements, specular.

20. ABSTRACT (Continue on reverse side if necessary and identify by block number)

A special chamber for measuring the off-axis response of high-rejection optical baffling systems was designed and constructed. The ambient background power level caused by atmospheric scattering was reduced by using high-efficiency particulate filters to remove the atmospheric aerosols and produce a clean-room environment. The effects of surface scattering were reduced by using specular surfaces in a modified cylindrical shape to direct the scattered radiation away from the baffle entrance. Two computer programs were used to predict the magnitudes of the atmospheric and surface scattering.

DD FORM 1473 EDITION OF 1 NOV 65 IS OBSOLETE

Item 20 (Continued)

Measurements which separated the atmospheric scattering from the surface scattering were performed. Rayleigh (molecular) scattering was determined to be the limiting mechanism in achieving a low background. The background power at 40° off axis was found to be 1×10^{-9} of the on-axis incident power for a 5° full-angle baffle when illuminated by a 10.2 cm diameter collimated beam. The background power from surface scattering in the specular chamber is about 4×10^{-11} of the on-axis incident power. A two-step process was used to measure a baffle response at 40° off axis down to less than 1×10^{-11} of the on-axis incident power.

LIST OF CONTRIBUTERS

Doran J. Baker -- Principal Investigator

Kay D. Baker -- Co-principal Investigator
Ronald J. Huppi -- Co-principal Investigator
Clair L. Wyatt -- Co-principal Investigator

D. Gary Frodsham -- Engineer
John C. Kemp -- Engineer
Glen A. Meldrum -- Programmer

A.T. Stair, Jr. -- AFGL Program Scientist
James C. Ulwick -- AFGL Program Scientist

RELATED CONTRACTS AND PUBLICATIONS

F19628-70-C-0280
F19628-70-C-0289
F19628-72-C-0255

TABLE OF CONTENTS

TABLE OF CONTENTS (Continued)

LIST OF FIGURES

LIST OF FIGURES (Continued)

INTRODUCTION

The basic problem of obtaining measured values of a relatively weak remote source in the presence of a relatively strong source is not new. The invention of the solar coronagraph (Newkirk and Bohlin, 1963), a telescope that effectively blocks out radiation from the sun's disk, has made it possible to study the brighter parts of the solar corona independently of a solar eclipse. However, the presence of dust or haze particles in the atmosphere scatters solar light coming from the corona itself; therefore, especially clear skies are required for good measurements.

Other examples are the infrared missile seeker that must be designed to reject radiation from an off-axis source like the sun or the earth, and a radiometer or spectrometer designed to make scientific measurements of various atmospheric emission species in the presence of the sun or the earth.

The geometric problem of the design of electro-optical sensors (regardless of application) is best understood in terms of the objective of the measurement as follows: the objective (Wyatt, 1976) of an electro-optical field measurement of a remote source is to obtain the total flux from a specific geometrical region centered about the optical axis. This specific region is determined by the instrument field of view. The geometrical problem is therefore a problem of spatial purity. The output indication of the instrument for a spatially pure measurement is a function of the flux originating within the specified region and is completely independent of any flux arriving at the instrument aperture from outside that region.

The actual performance of an optical system may be severely limited by the environmental conditions under which it must be applied. For example, the solar coronagraph is limited by scattering that takes place in the intervening atmosphere. Scattering by the atmosphere may be reduced, for a solar coronagraph, by seeking a high altitude observatory or perhaps even a space-lab platform orbiting above the earth's atmosphere.

The research reported herein is concerned primarily with the off-axis

response evaluation of radiometric or spectrometric instruments that have been designed for in situ measurements of atmospheric emission species in the visible and infrared. These instruments, carried into the upper atmosphere on rocket or balloon carriers, are designed to measure the total emission and scattering of the atmosphere within the volume extending from the instrument aperture along the optical axis, and must reject any flux incident upon the instrument aperture that emanates from off-axis sources such as the sun, moon, or earth.

Figure 1 is a representation of a typical measurement situation. The earth and the sun are shown as sources of radiation which could contaminate the desired measurement unless the optical baffling is sufficient to reject the flux from the sun at the angle θ_{sun} and the earth's flux at the angle θ_{earth}.

The off-axis response of an optical baffling system is evaluated by illuminating the instrument aperture with unidirectional (collimated) light at various angles. Such measurements yield an off-axis point source response function (normalized to unity on axis), which for high-rejection systems with angles beyond the nominal field of view may fall many orders of magnitude.

The Research Problem

The general rule of instrument calibration (Nicodemus and Zissis, 1962, quoted by Wyatt, 1976) should apply to the case of the evaluation of the off-axis response; namely, the calibration should be conducted under conditions which reproduce, as completely as possible, the conditions under which the measurements are made for which the instrument was calibrated. However, the space-background conditions are not easily simulated in an earthbound laboratory. The evaluation of the off-axis response may be limited by a relatively high-level ambient background. This background results from the laboratory environment: air, walls, and equipment which radiates and scatters flux into the aperture from all directions.

Thus, more specifically, this research deals with the development of a special calibration facility. This facility is designed to reduce scattering
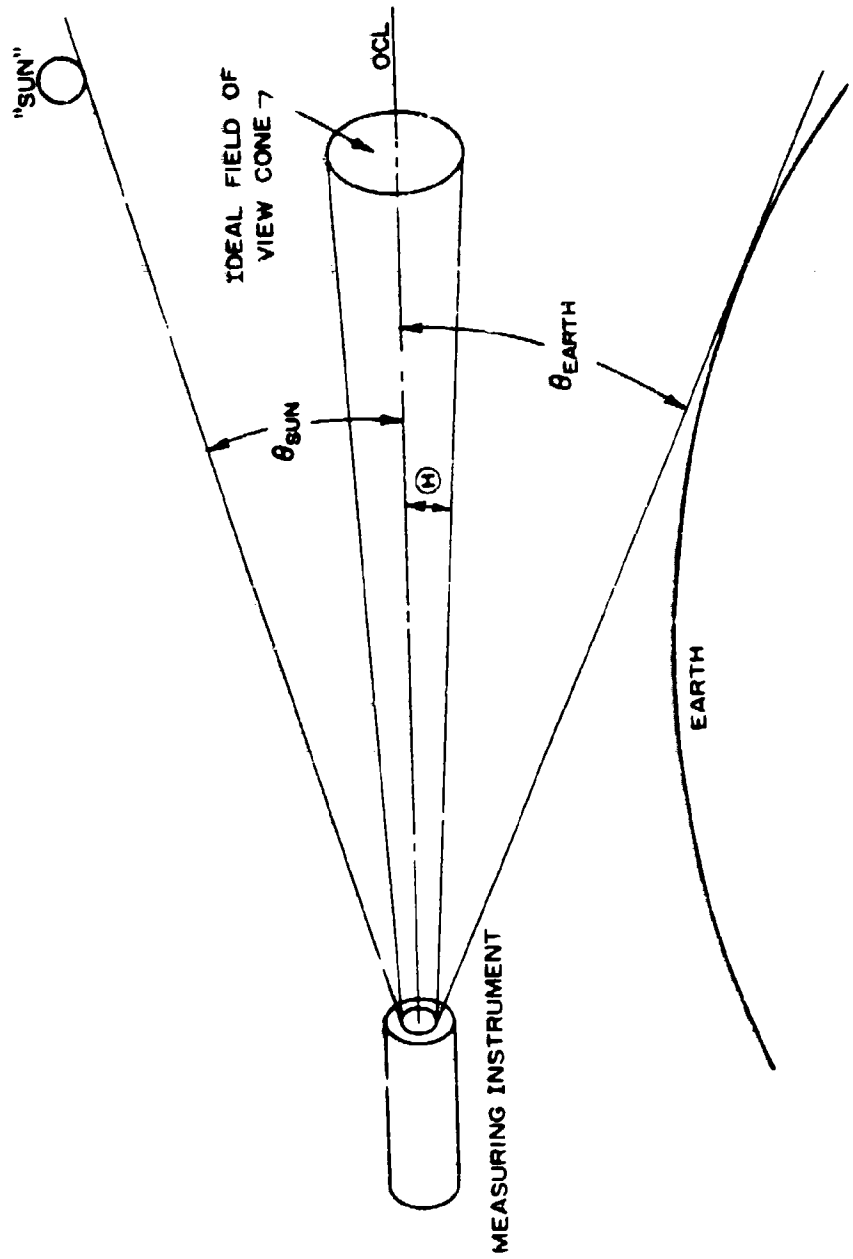
Figure 1. Representation of a typical measurement situation.

backgrounds to as low a value as possible in an attempt to simulate space-background conditions in accordance with the general rule of instrument calibration.

The off-axis response of an instrument is evaluated by measuring the field of view of the instrument. The field of view is defined as the normalized off-axis response to a point source and may be specified in terms of spherical coordinates over the entire responsive domain of the instrument. The value of the transfer function for a given direction (θ, ϕ) is defined as the ratio of the response at (θ, ϕ) to the peak (on-axis) response (i.e., $\theta = \phi = 0$).

The actual response at a direction (θ, ϕ) is a function of the instrument baffle design, the Mie scattering from the atmospheric aerosols (dust, smoke, water, etc), the Rayleigh (molecular) scattering, and the scattering off the walls of the calibration chamber. The transfer function is independent of the absolute value of the areance [irradiance]* of the source as it cancels out in the ratio of on-axis to off-axis values. The ideal system that best approaches the conditions of measurement (the space-background conditions) is one in which the response at the direction (θ, ϕ) is a function of the baffle design only. Such a response would provide an exact evaluation of the instrument baffle.

It was considered beyond the scope of this research project to attempt to reduce the thermal emissions of the chamber walls by cryogenic cooling techniques; therefore, the design and theory apply primarily in the visible where thermal emissions are negligible compared with scattering. The evaluation of infrared systems is possible only through measurements in the visible and extrapolation to the IR.

It was also beyond the scope of this research project to consider evacuating the chamber to provide an atmosphere-free environment. However, the Mie scattering can be reduced through the use of a cleanroom environment, and the chamber wall scatter can be reduced by the design of the shape and surface characteristics of the chamber walls.

*Areance, a term based upon the concepts of phluometry as suggested by Jones (1963), Spiro (1974), and Wyatt (1976) is the generalized term for irradiance and has units of flux per square centimeter.

4

backgrounds to as low a value as possible in an attempt to simulate space-background conditions in accordance with the general rule of instrument calibration.

The off-axis response of an instrument is evalu ted by measuring the field of view of the instrument. The field of view is defined as the normalized off-axis response to a point source and may be specified in terms of spherical coordinates over the entire responsive domain of the instrument. The value of the transfer function for a given direction (θ, ϕ) is defined as the ratio of the response at (θ, ϕ) to the peak (on-axis) response (i.e., $\theta = \phi = 0$).

The actual response at a direction (θ, ϕ) is a function of the instrument baffle design, the Mie scattering from the atmospheric aerosols (dust, smoke, water, etc), the Rayleigh (molecular) scattering, and the scattering off the walls of the calibration chamber. The transfer function is independent of the absolute value of the areance [irradiance][*] of the source as it cancels out in the ratio of on-axis to off-axis values. The ideal system that best approaches the conditions of measurement (the space-background conditions) is one in which the response at the direction (θ, ϕ) is a function of the baffle design only. Such a response would provide an exact evaluation of the instrument baffle.

It was considered beyond the scope of this research project to attempt to reduce the thermal emissions of the chamber walls by cryogenic cooling techniques; therefore, the design and theory apply primarily in the visible where thermal emissions are negligible compared with scattering. The evaluation of infrared systems is possible only through measurements in the visible and extrapolation to the IR.

It was also beyond the scope of this research project to consider evacuating the chamber to provide an atmosphere-free environment. However, the Mie scattering can be reduced through the use of a cleanroom environment, and the chamber wall scatter can be reduced by the design of the shape and surface characteristics of the chamber walls.

_____

[*]Areance, a term based upon the concepts of phluometry as suggested by Jones (1963), Spiro (1974), and Wyatt (1976) is the generalized term for irradiance and has units of flux per square centimeter.

6

2. It was to be determined if the Mie scattering had been effectively eliminated.

3. The background power level due to the scattering off the walls was to be evaluated.

A state-of-the-art measurement of the off-axis response of a typical sunshade baffle was to be performed as a demonstration of the effectiveness of the specular clean chamber.

BACKGROUND AND REVIEW OF THE LITERATURE

There are few articles in the open literature dealing specifically with the design and/or performance of optical baffles. This may be due, in part, to the specialized nature of systems requiring baffling and also to the fact that designs for military systems remain classified and generally unavailable.

Leinert and Klüppelberg (1974) discuss the difficulty of measuring stray light suppression for high orders of rejection. They give a value for the scattering of visible light by air as about 4×10^{-12} of the incident flux into a 1° field of view per cm. Stray light contributions from scattering off lenses, mirrors, and knife edges, as well as from diffraction by apertures are discussed. A two-step measurement process of measuring the performance of each stage of the baffle separately and then combining the results to get an overall attenuation factor is discussed. An attenuation factor of 2×10^{-9} at 85° claimed for a particular baffle was apparently determined in such a two-step measurement.

Heinisch and Jollife (1971) given practical baffle design criteria and compare seven different types. Monte Carlo analysis is introduced as an evaluation tool. They report the measured background illumination level of the room used for their measurements to be seven orders of magnitude lower than the source. Yap (1974) discusses in a general manner the optical coupling of straylight into sensing systems. Some conventional measurement techniques and design considerations to improve out-of-field rejection are discussed but no measured or predicted numbers are reported. Schenkel (1973) gives good background into the difficulties of measuring off-axis response beyond a few orders. Measurement of seven orders of rejection at 60° is reported but the off-axis response curve seems to show the background of the measuring facility at about five orders. He states that operation in a space environment proved the system rejection was ten orders of 60° for that condition.

Marette and Gérard, (1976), give a brief description of a two-stage baffling system for a photometer. They state that their laboratory tests

demonstrated that Rayleigh and Mie scattered signals dominated the instrumentally scattered signals. However, the measured curve shown to support this claim extends less than five orders of magnitude below the on-axis response and also extends less than 20° off axis. A second figure shows the two baffle stages measured independently and extends from five orders below the on-axis response at 69° off axis to eight orders down at 87°. Their claim of limitation by atmospheric scattering is not justified by the results given.

Newkird and Bohlin (1963) discuss five sources of scattered light in a refractive Lyot coronagraph. Their article is particularly useful in designing an imaging baffle with refractive optics. An electrostatic cleaner and air circulating system was used by MacQueen (1968) to reduce scattering in a measurement facility. Measurement of seven orders of rejection for a coronagraph is reported but it is also stated that this was approaching the background illumination levels of the measurement chamber.

Shaeffer and Fastie (1972) made off-axis measurements by using a small screen to scatter light from a constant intensity source into the instruments field of view. Laboratory tests indicating that Rayleigh scattering dominated the instrument scattered signals are reported. Flight data was used to infer a rejection of 4×10^{-11} at 85° in space. Boksenberg et al., (1970, 1971) describe a baffle system and mention Monte Carlo Analysis.

The relationship of the reflection or scattering of incident radiation by a surface to the roughness of the surface is discussed by Beckmann and Spizzichino (1961), Bennett and Porteus (1961), and Davies (1954). Several investigators, including Agnew and McQuistan (1953), Aughey and Baum (1954), Blazey (1967), and Torrance (1966) have described instruments and techniques for measuring the angular variation of light scattered by a particular surface. The nomenclature used in describing the directional reflectance characteristics of surfaces are given by Kasten and Raschki (1974) and Nicodemus (1970). The geometrical properties of radiation transfer will be described using the concepts and terms of phluometry as suggested and developed by Jones (1963), Nicodemus (1973), Spiro (1974) and Wyatt (1976).

The scattering of incident radiation by the molecules and aerosols of the atmosphere is discussed by Bullrich (1964), Kerker (1969), and Kondratyev (1969). Excellent tabulations of atmospheric scattering parameters are given by McClatchey et al., (1972) and Penndorf (1957).

An excellent survey of Monte Carlo methods including the application of this technique to thermal radiative transfer is given by Howell (1968). Energy partitioning techniques are discussed by Shamsundar, Sparrow and Heinisch (1973). A Monte Carlo approach to optical analysis is discussed by Chou (1972, 1974) and Heinisch and Chou (1971).

FIELD-OF-VIEW MEASUREMENTS

The objective of this section is to introduce the basic theory dealing with
spatial purity concepts and also to describe the basic techniques used in
measuring or calculating the field of view* of an optical system. The same
theory applies and the same measurement techniques are used whether the
field of view is to be characterized to only a few orders of magnitude below the
on-axis response or whether an evaluation of many orders is required. The
extension of these visible measurement techniques into the infrared region is
briefly discussed along with the prediction of baffle performance beyond
measurement ability.

The objective of any radiometric measurement, so far as spatial purity
considerations are concerned, is to determine the total flux from a specific
region within the viewing field of the instrument. The measurement is accurate
only if the instrument response is proportional to the total flux from within the
desired region and is completely independent of any off-axis sources. Two ideal
conditions which satisfy this requirement are given.

Summary of Field-Of-View Theory

Consider an instrument viewing in the vertical (+Z) direction with its
entrance aperture in the Z = 0 plane and its optical axis coincident with the Z
axis. Although it is desired to measure the flux from a narrow conical region
centered about the Z axis within the half angle θ (the field of view angle), it is
possible for radiation from any point whose Z coordinate is greater than zero
to enter the entrance aperture and contribute to the instrument output. It is
convenient to represent this flux as originating from the inside surface of a
hemisphere centered at the origin with its base in the Z = 0 plane as shown in

---

*The phrase field of view is often abbreviated fov, which term will also be used
in this paper.

Figure 2. Then the sterance [radiance][*] of the flux incident to the instrument can be represented as a function of the spherical coordinates θ and ϕ and is given by $L(\theta, \phi)$ with units of flux per square cm per steradian (ϕ cm^{-2} sr^{-1}).

The total flux within the field of view is given by the integral of the sterance over the field of view

$$\phi = A_c \iint_{fov} L(\theta, \phi) \, d\Omega \quad , \tag{1}$$

where $\iint_{fov}$ indicates that the integral is taken over the solid angle field of view, A_c is the collector area, and $d\Omega$ is the differential solid angle subtended at the instrument entrance aperture.

As a radiometric instrument views a source its output Γ is proportional to the sterance of the source and to the instrument response function $R_o R(\theta, \phi)$ which relates the output to the directionally incident flux, where R_o is the absolute on-axis responsivity, and $R(\theta, \phi)$ is the relative angular response normalized to unity on the optical axis. The actual instrument response to a sterance distribution $L(\theta, \phi)$ is found by integrating the product of the instrument response function and the source sterance over the entire hemisphere

$$\Gamma = R_o A_c \iint_{2\pi} R(\theta, \phi) \, L(\theta, \phi) \, d\Omega \quad \text{output units} \tag{2}$$

where $\iint_{2\pi}$ indicates that the integral is taken over the hemisphere.

The practical (nonideal) solid angle field of view of an instrument may be determined from the normalized response to a uniform extended optical source of sterance L_o and may be defined by

$$\Omega = \frac{1}{R_o L_o} \iint_{2\pi} R_o L_o \, R(\theta, \phi) \, d\Omega = \iint_{2\pi} R(\theta, \phi) \, d\Omega \quad \text{steradians} \quad . \tag{3}$$

---

[*] Sterance, a term based upon the concepts of phluometry is the generalized term for radiance to denote the positional and directional aspects of flux and has units of flux per unit projected area and solid angle (ϕ cm^2 sr^{-1}).
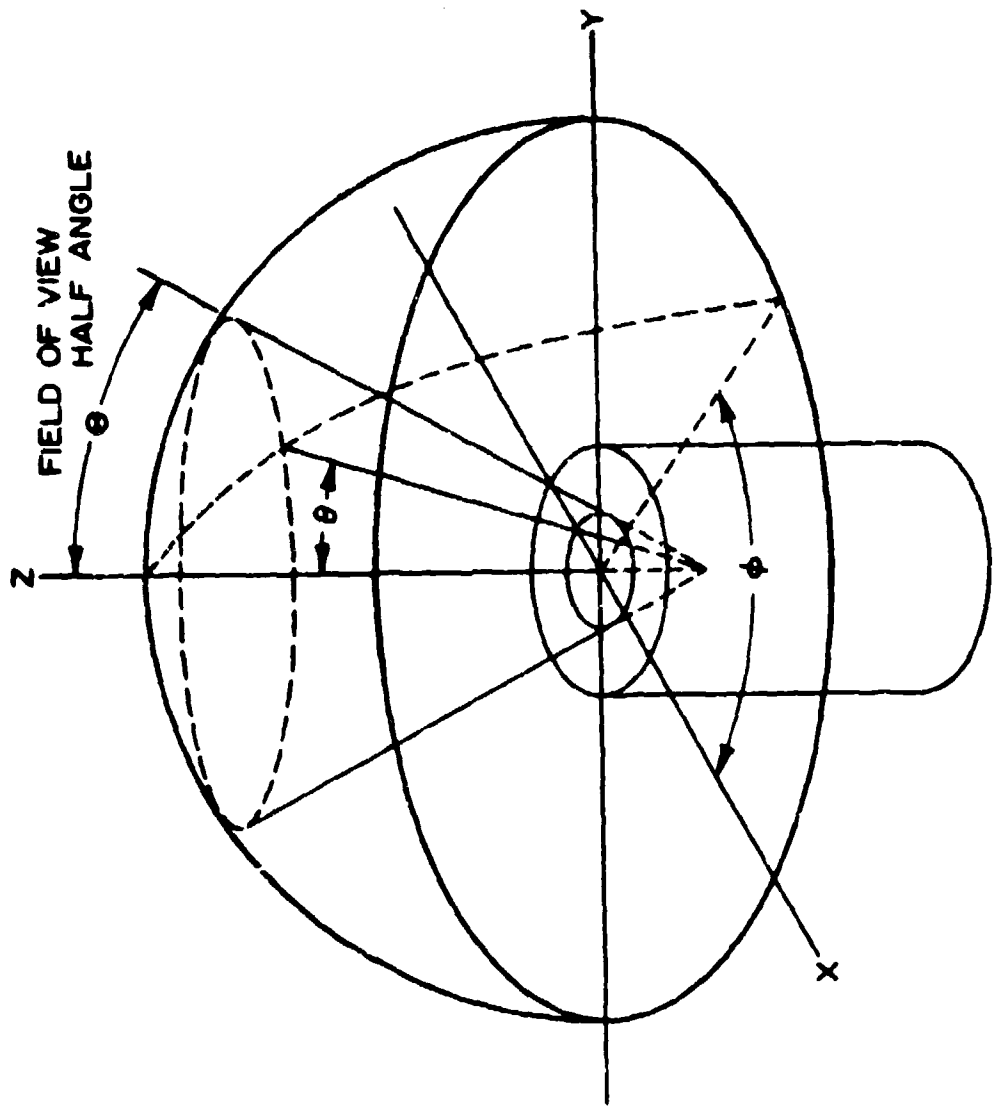
Figure 2. The geometry of the field of view of a vertically viewing instrument with the incident flux represented as coming from the inside of a hemisphere.

14

On the other hand, an ideal field of view has a relative angular response $R(\theta, \phi)$ equal to unity for all (θ, ϕ) included within Θ, the desired field of view, and zero elsewhere. Thus $R(\theta, \phi)$ is a unity constant over Θ and passes through the integral. In this case Equation (3) becomes

$$\Omega = \iint_{2\pi} R(\theta, \phi) d\Omega = \iint_{\text{fov}} d\Omega \qquad , \qquad \text{sr} \qquad (4)$$

and the limits of integration may be diminished to cover the field of view region only.

The apparent target flux ϕ_a is given by the quotient of the output and the absolute on-axis responsivity

$$\phi_a = \frac{\Gamma}{R_o} = A_c \iint_{2\pi} R(\theta, \phi) L(\theta, \phi) d\Omega \qquad . \qquad (5)$$

The apparent target flux ϕ_a will equal the total target flux ϕ when

$$\iint_{\text{fov}} L(\theta, \phi) d\Omega = \iint_{2\pi} R(\theta, \phi) L(\theta, \phi) d\Omega \qquad . \qquad (6)$$

There are two conditions under which Equation (6) is valid:

1. When the instrument has an ideal field of view then $R(\theta, \phi)$ is a unity value constant and passes through the integral as in Equation (4) and the two sides of the equation become identical.

2. When the flux sterance is uniform then $L(\theta, \phi) = L_o$ for all θ and ϕ, L_o passes through the integrals and both sides of Equation (6) become equal to $L_o \Omega$. Thus, the best that can be done when the measuring instrument has a nonideal field of view is to state that ϕ_a, as measured, is correct if the source sterance is spatially uniform.

.ne first condition is definitely more powerful than the second in terms of lack of qualification necessary for the measured data. Consequently, great effort is expended to achieve practical systems that approach an ideal field of view.

Practical Measurement Techniques

The basic techniques used in evaluating the field of view of an optical baffling system are now discussed. There are two regimes of off-axis response. The "near-field" extends from the optical axis to just beyond the field-of-view cutoff angle θ. The off-axis response in this region is determined by the convolution of the source-image with the field stop in the focal plane and generally extends down about three orders of magnitude from the on-axis response. Because of the relatively high values of response in this region, the near-field is easy to measure. The second regime, the "far-field" response is determined by the scattering and diffraction performance of the baffle and extends from the near-field region out to 90 degrees to include the whole hemisphere. The far-field can be characterized only to the limit imposed by the ambient levels of background radiation to which the instrument is also sensitive.

The spatial response function (the field of view) is defined as the response to a point source over θ and ϕ. Therefore, a source of unidirectional or collimated light is required to simulate a point source. A collimator, consisting of the aperture of a radiation source located at the focal point of a lens or mirror, provides a practical method of obtaining unidirectional light. The mirror system is preferred because the aberrations of a reflecting system are less than those of refracting system (Smith, 1966), there is no bulk scattering as occurs in the lens material, and also reflectivity is not as strong a function of wavelength as is refraction. The collimated beam must overfill the entrance aperture of the instrument so that as the instrument is rotated the aperture will always be fully illuminated.

16

The divergence of the collimated beam must be kept small in relation to the angular resolution required in the measurement. The total divergence angle Y can be found from

$$Y = \arctan \frac{d}{f} \quad , \tag{7}$$

where   d is the diameter of the source aperture, and

f is the collimator focal length.

Various radiation sources can be used with a collimator. Xenon arcs, high-temperature blackbodies, lasers, and tungsten-halogen lamps are common (Heinisch and Jolliffe, 1971; Leinert and Klüppelberg, 1974; Yap, 1974).

Some means of interrupting or "chopping" the radiation from the source should be provided to enable improved rejection of any background or stray radiation signals by the use of phase-locked signal processing techniques. The source should be stable for the duration of the measurement although it does not need to be calibrated. For precision measurements it is appropriate to have a detector to monitor the collimated beam areance [irradiance] so that compensation can be accomplished in the data reduction for any changes in areance during the measurement.

A means must be provided to reduce the collimated beam areance during the measurement of the near-field response, because the system response is so much greater for the near-field measurements than for the far-field. Often, neutral density filters are inserted in the optical path to provide high attenuation on axis and then selectively removed to provide progressively less attenuation as the measurement is extended further into the far-field region.

A fold-back technique can be used to eliminate the need for external attenuators if a stable but variable power source is available. The source is set at a low power for the near-field measurements; as the off-axis angle is increased the source power is incrementally increased. The instrument response is recorded at both power levels before any positional changes are made. The ratio of the low response to the high response at the same coordinates is calculated and measurements made after this are then multiplied by this ratio to unfold the data. This

procedure can be repeated several times during a scan so that the dynamic range of the measuring equipment can be extended; however, this approach may suffer from accumulative errors.

A method must be provided to change the relative orientation of the source and the instrument. It would be ideal to take all measurements by sweeping along the radial "rays" extending from the optical axis of the instrument. This can be done by mounting the instrument in a cradle such that between each azimuth sweep it could be rotated around its optical center line by some specified angle. There are practical reasons why this cannot always be done. The cryogenic requirements, for example, may preclude physical rotation of the instrument package; also, the actual location of the optical axis may not be known.

Any field-of-view measurement facility will be designed to shield the experiment from unwanted external radiation as well as ambient dust. The measurements should be conducted in conditions of darkness in spite of the phase-locked detection techniques used to eliminate background effects, because a large offset on the detector from room lights can cause nonlinearities with unpredictable results. All surfaces in the measurement room are typically painted a dull black to increase the absorption.

Often the platform for changing the instrument azimuth, the source, and the collimator are placed on a lab bench or on a table for convenience and ease of alignment. This gives a scattering surface very close to the entrance aperture of the instrument. It would be much better to have at least the instrument itself mounted on a pedestal to increase the separation between it and any scattering surfaces.

Extension to Infrared Wavelengths

Field-of-view measurements for infrared instruments are complicated by the thermal emissions from the ambient environment which may be more than sufficient to saturate a sensitive instrument. The background flux can be

reduced by means of a thermally-cold pinhole placed in the entrance aperture; however, the field of view is modified in a way difficult to qualify.

Special calibration chambers have been constructed that provide for vacuum and cryogenic continuity with the instrument. Such a chamber may be equipped with a collimator, a source, and remote control capabilities for driving the source through the field of view. Scattering off the chamber walls provides a limit to off-axis measurements as in any facility. Large chambers with cooled walls have improved scattering characteristics but are very costly to use.

Measurements can be made under ambient conditions in the near infrared (to about 1.8 μm) even for sensitive instruments. However, in the case of cryogenic instruments an IR window must be used to maintain the system vacuum integrity. Such a window interferes with the measurement of the instrument off-axis response as is shown in Figure 3. In this case a quartz window was used. The magnitude of the degradation depends upon the wavelength and the field of view of the optical system and upon the thickness and quality of the vacuum window.

The field of view of a cryogenic infrared instrument can be evaluated at ambient temperature by substituting an ambient temperature detector for the cold detector. The substitute detector must be of the same size so that the field of view is the same. A multiplier phototube equipped with a field stop to simulate the IR detector is often used to match the system for field-of-view measurements. However, the visible measurements made with the pm tube must be extrapolated to the wavelengths for which the instrument was designed. There are three limiting mechanisms whose effects must be considered: atmospheric scattering, rough surface scatter and diffraction at apertures. The computation of the magnitude of these effects involves considerable detail and only a very brief qualitative description is given.

Atmospheric scattering has two components: Rayleigh scattering is due to air molecules and has a cross section inversely proportional to the fourth power of the wavelength (Penndorf, 1957). Mie scattering is due to atmospheric aerosols and is dependent upon the aerosol number density, size distribution and index of refraction. Mie scattering is an oscillatory function of the ratio of particle size
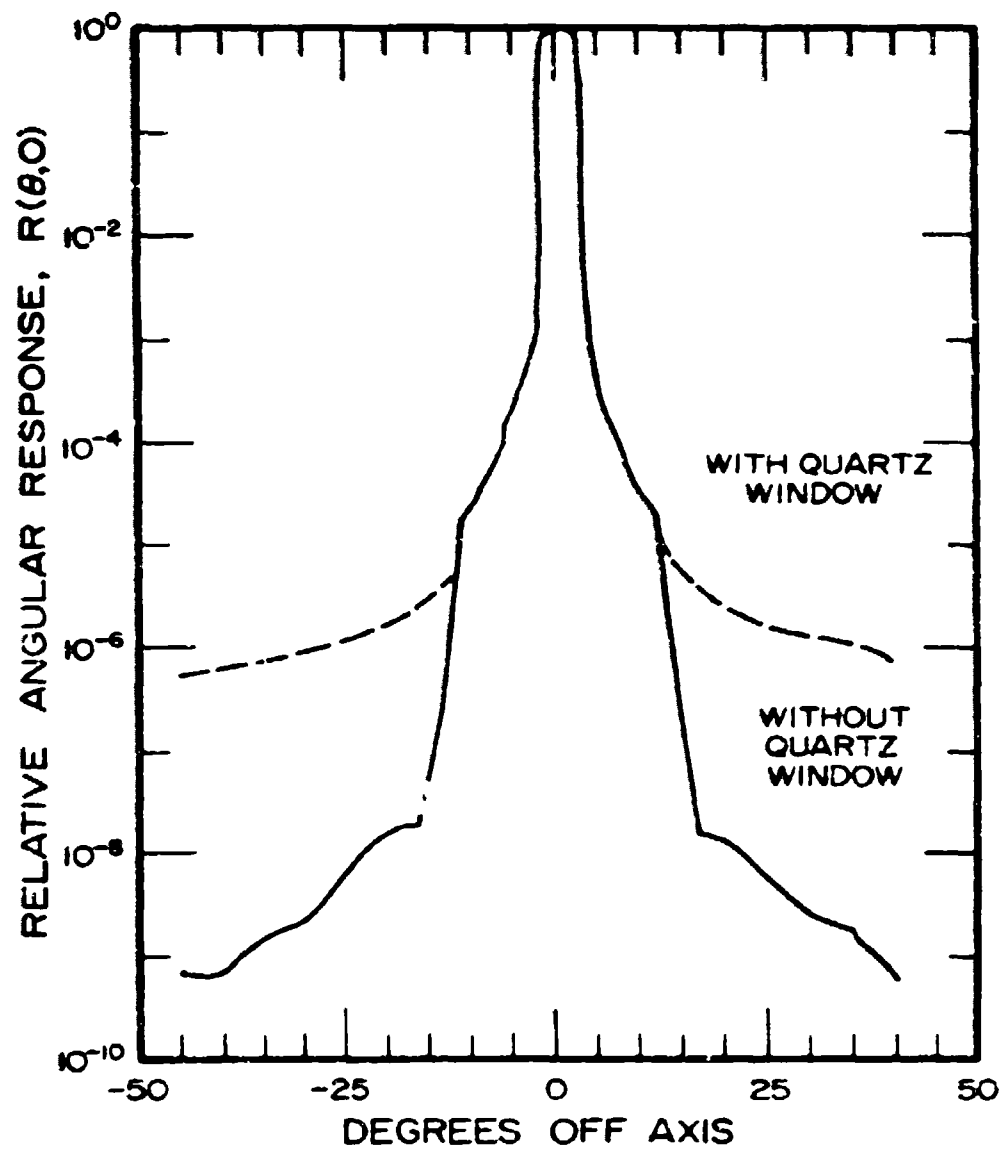
Figure 3. Measured field-of-view plot showing the background limitation caused by a one quarter inch thick quartz vacuum window.

to wavelength. Bullrich (1964) gives useful graphs of scattered light intensity as functions of wavelength and angle for several aerosol size distributions. Penndorf (1956) has compiled an extensive table of computed values and McClatchy (1972) gives useful information on angular dependence. Rayleigh scattering becomes negligible when compared to Mie scattering at longer wavelengths.

The absolute level and the spatial distribution of the flux scattered off the surfaces of the baffle are dependent upon the material, surface roughness in relation to the wavelength, and also the angle of incidence (Beckmann and Spizzichino, 1963). The surface becomes more specular and less diffuse as it becomes smoother. Of course, the smoothness of a surface is a function of wavelength--surfaces appearing to be smoother at longer wavelengths. However, the reflectance may exhibit anomalies at particular wavelengths where molecular absorption occurs or because of restrahlen effects. Thus, extrapolation to longer wavelengths must take into account such effects (Blazey, 1967; Heinisch, 1971; Hostetter et al., 1968; Look, 1965; Wilson and Wade, 1974).

Diffraction is a very complicated phenomena, but in general the sine of the angle of diffraction is proportional to the wavelength (Fowles, 1968; Klein, 1970), and thus will cause more degradation of the off-axis rejection in the infrared than in the visible. Diffraction effects are difficult to calculate but recently a model based upon probability theory has been useful for such calculations (Heinisch and Chou, 1971).

Prediction Beyond Measurement Ability

Because of the limitations imposed by both atmospheric and surface scattering, off-axis measurements of more than seven orders are very difficult (Schenkel, 1973; Heinisch and Jolliffe, 1971). However, it is often necessary to predict off-axis rejection of nine or more orders. In this case the measured data must be extrapolated by calculations using the mathematical model.

There are several considerations involved in the prediction of baffle performance. All surfaces must be characterized by an absorption coefficient

and specular and diffuse reflection coefficients. It is often necessary to make educated assumptions about surface reflectance characteristics, since it is not practical to measure every surface under every condition in which it may be used. These same coefficients must be determined for refractive elements and, in addition, the diffuse and specular transmission coefficients. Knife edges must also be characterized in terms of diffuse and specular reflectivity.

Diffraction effects will be vastly overshadowed by surface scattering and can be neglected when the apertures are large compared with the wavelength of light being considered. Diffraction must be considered in the case of baffles where the field of view is very narrow (on the order of a degree or less). The assumptions used in these predictions can be tested by calculating the response for some angles at which the measurement can be performed and then comparing the measured values with those predicted.

All possible paths for light radiation entering the entrance aperture at the specified angle must be considered. The complexity of this process is demonstrated by the multiplicity of paths possible for the simple baffle shown in Figure 4, where each of the surfaces and knife edges as well as the entrance and exit apertures are numbered for identification. A topological power transfer graph can be drawn to provide a pictorial representation of the power transfer as shown in Figure 5.

The numbered nodes correspond to the numbered surfaces, knife edges and apertures, and the directed branches connecting the nodes represent possible power transfer processes. Each branch connecting two nodes has an associated power transfer coefficient. Each node thus represents a variable (the power available for reflection or diffraction from the surface or knife edge) and each branch represents a functional relation for the power transfer between the two surfaces.

The available power at each node can be determined by use of the power transfer coefficients for the connecting branches until the power transferred from node 1 to node 2 is obtained. The numerous feedback paths and cross links evident from Figure 5 make this an enormous task unless gross simplifying assumptions can be made.

22
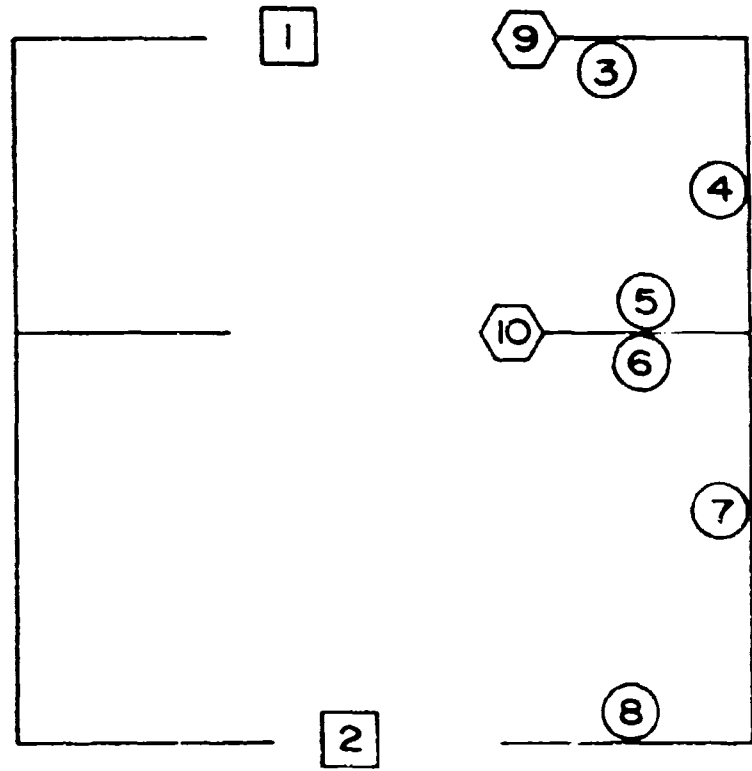
□ ENTRANCE OR EXIT APERTURE

⬡ KNIFE EDGE SCATTERING SURFACE

◯ BROAD SCATTERING SURFACE

Figure 4. Cross section of a simple baffle used as a model for the power transfer graph of Figure 5.

POWER INPUT

POWER LOST THROUGH
ENTRANCE APERTURE

EXIT

☐ ENTRANCE OR EXIT APETURE   ⟶ DIFFUSE REFLECTION

⬡ KNIFE EDGE SCATTERING SURFACE   ─·─► SPECULAR REFLECTION

◯ BROAD SCATTERING SURFACE   ---► DIFFRACTION PROCESS
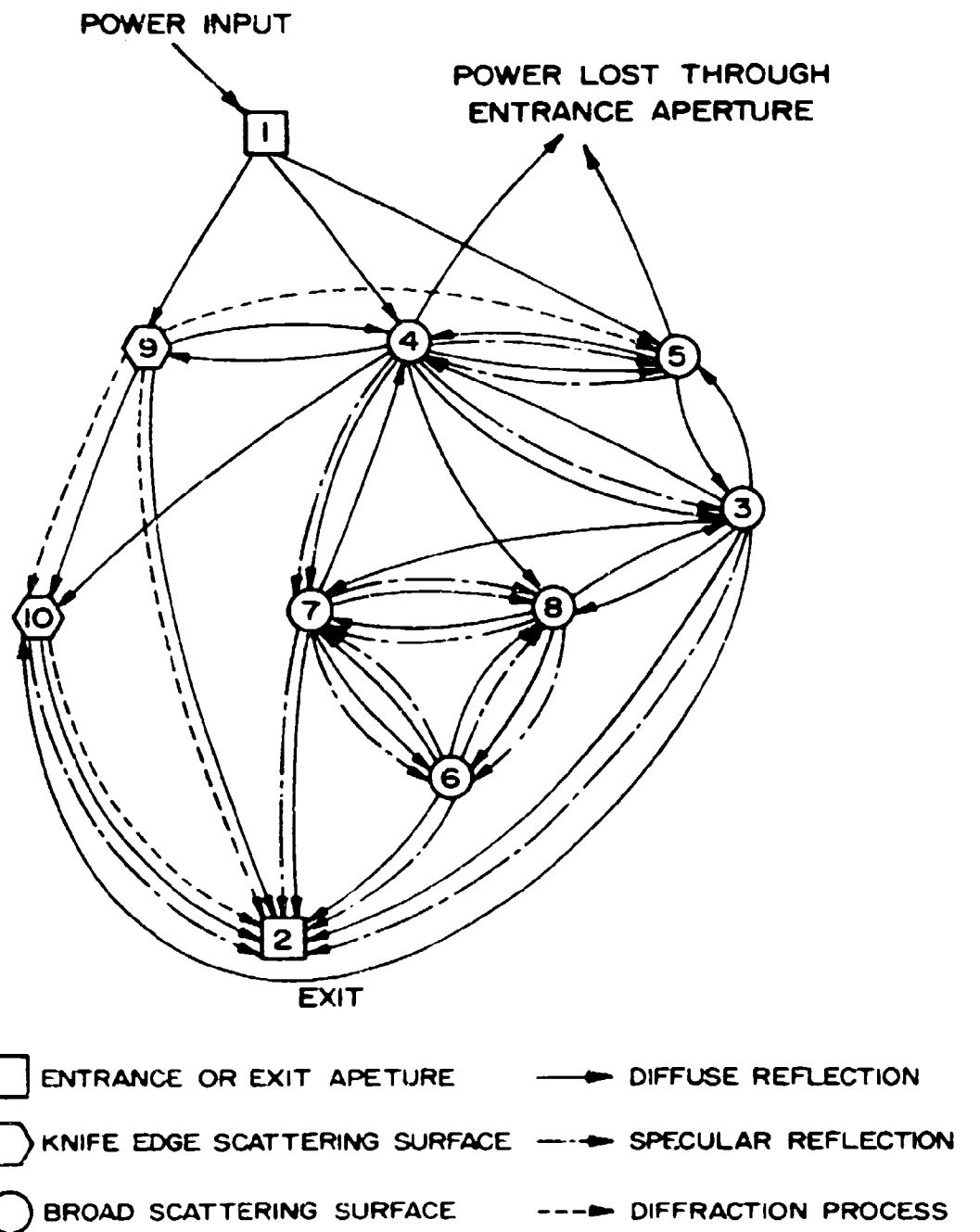
Figure 5. Topological power transfer graph corresponding to Figure 4.

The following is an example of the calculation of a power transfer coefficient where the power transfer from a diffuse surface (node 1) to a second surface (node 2) is determined. A diffuse source (node 1) of power P_1 will have a radiant pointance [intensity] $I(\theta)$

$$I(\theta) = \frac{P_1 \cos \theta}{\pi} \quad , \quad (8)$$

where θ is the polar angle from the normal to the surface.

The power incident at surface 2 from surface 1, P_{211}, is found by integrating the pointance $I(\theta)$ over the solid angle subtended by surface 2 at surface 1,

$$P_{211} = \int_{\Omega_2} I(\theta)d\Omega_2 = \frac{P_1}{\pi} \int_{\Omega_2} \cos \theta \, d\Omega_2 \quad . \quad (9)$$

As only a fraction Γ_2 of the incident energy P_{211} is available for reflection off surface 2, the useable power at surface 2 because of radiation from surface 1 is

$$P_{21} = \Gamma_2 P_{211} = \frac{\Gamma_2 P_1}{\pi} \int_{\Omega_2} \cos \theta \, d\Omega_2 \quad . \quad (10)$$

The power transfer coefficient T_{21} is defined as the ratio of the power at surface 2 from surface 1 to the original power at surface 1,

$$T_{21} = \frac{P_{21}}{P_1} = \frac{T_2}{\pi} \int_{\Omega_2} \cos \theta \, d\Omega_2 \quad . \quad (11)$$

The power available at node 2 is the sum of the contributions from all of the other surfaces,

$$P = \sum_i T_{21} P_i \quad . \tag{12}$$

The evaluation of the power at the final node is not so simple as Equation (12) seems to indicate because of the interdependence of P_i and P_2.

Equation (9) is valid only when node 1 is small and has a uniform power. Generally for real surfaces P is not a constant over node 1 and is better specified in terms of the radiant areance [exitance] $M(x, y)$ and integrated over surface 1.

$$P_{21i} = \frac{1}{\pi} \int_{\Omega_2} \int_{A_1} \cos \theta M_1(x_1, y) dA_1 \quad . \tag{13}$$

The above example is an illustration of the simplest possible situation, because the prior history of the ray was neglected and the reflecting surface was considered as an emitting source. The surface cannot always be considered to be perfectly diffuse; in this case a different model must be used that includes a specular component. The bidirectional reflectance-distribution function of Nicodemus (1970) or Kasten and Raschke (1974) must be considered, which allows the reflected radiation to be dependent upon the angles involved in the incident radiation. These additional considerations create a situation in which the problem becomes so unwieldy as to be nearly impossible to solve.

The power transfer coefficient for diffraction is an extremely difficult problem and a simplified model must be used. Fortunately, diffraction effects are often small relative to scattering effects. However, this must be justified using the simplified difraction model.

Honeywell Aerospace Division has developed a computer program GUERAP (General Unwanted Energy Rejection Analysis Program) (Chou, 1974), which can be used to calculate the off-axis rejection of baffles. However, a Monte Carlo approach is used rather than the complex calculation of the power transfer coefficient, as described above.

A number of ray bundles is admitted to the entrance aperture at any desired direction and each ray bundle is traced through the system. Each ray bundle is treated as a discrete packet of energy. As the rays intersect any surface, a fraction of the energy is deleted according to the probability of absorption at the surface. The remaining energy is divided between specular and diffuse components with the energy in each component assigned according to the appropriate probability. Random numbers are used to assign directions within the limits set by the assigned probabilities for the diffuse components. The energy of each ray bundle that reaches the exit of the baffle is tallied and the energy at the exit is compared with the energy at the entrance to obtain the baffle rejection properties.

Special energy partitioning techniques allow the programmer to force rays in desired directions by appropriately reducing the associated energy so that the probability distribution functions are still satisfied. This importance sampling technique allows dramatic computer time reduction over more standard Monte Carlo techniques.

DESIGN OF A FIELD-OF-VIEW MEASUREMENT FACILITY

A special field-of-view calibration facility was required to measure the
off-axis response of high-rejection optical baffling systems developed at USU.
The objective was to create a chamber in which space-background conditions
could be simulated as nearly as possible. The design goal was to achieve a
facility in which the off-axis background is dominated by molecular scattering
and in which the effects of surface scattering and aerosol scattering are
negligible.

Rationale

It was recognized that using black diffuse surfaces to absorb scattered
radiation would not provide sufficiently low backgrounds to measure the off-axis
response of high-rejection optical baffling systems. In addition, the Mie
scattering from atmospheric aerosols would make a significant contribution
to the background at shorter wavelengths. Therefore, a unique approach to
off-axis measurements is obtained by constructing a non-diffuse (specular)
chamber within a clean-room environment where the specular surfaces are
shaped to direct the unwanted radiation to a non-critical region.

The idea of using specular surfaces in baffles is not new (Schenkel, 1973;
Leinert and Klüppelberg, 1974). Many materials such as very highly polished
metal or glass provide a specular surface but they are not very absorptive.
The use of a material having a black specular surface which is both highly
absorbing and specular is desirable.

The chamber shape was designed following ray trace analysis of several
candidate shapes. The key to successfully using specular walls is to orient
them so that no rays scattered off the entrance aperture can intersect the walls
in a normal or near normal direction. Any rays intersecting the specular walls
in a near normal direction will be directed back very close to the region from
whence they came. Thus, improper application of a specular surface can

actually result in scattered radiation from the baffle edges being specularly directed back to the entrance aperture. A successful approach lies in choosing a shape that will maintain an absence of near normal scattered rays over a wide range of baffle orientations.

The ray trace analysis indicated serious limitations from using rectangular shapes because the right-angled corners tend to direct any rays approaching the corners back very close to their origin; therefore, a smoothly curved surface with no right angles is desired. A circular shape maximizes the ratio of enclosed volume, yielding the minimum scattering surface per unit clean volume.

Analysis indicates that a circular specular shape will reflect the scattered rays away from the entrance aperture as long as no rays are allowed to pass through the center of the circular shape. Any ray traveling in a direction that passes through the center will be reflected back still close to the center but on the other side, away from the point of origin. A modified circular shape which has two centers with the entrance aperture placed between them has the desired directional properties as shown in Figure 6. The spacing between circle centers is made large enough so that the scattering surface presented by the front plate of any instrument to be tested fits well inside of the two centers. Any rays scattered from between the two centers will be specularly reflected back outside of the centers and away from the instrument.

The modified circular shape was extended into a modified cylinder in three dimensions because the cylinder is so well adapted to a vertical flow clean room and also because of other construction advantages.

Practical Implementation

A practical implementation of the specular chamber for off-axis response evaluations (SCORE) has been constructed at USU using readily available materials. A laboratory room 3.25 m wide by 6.1 m long with a ceiling 3.4 m high was used for construction of the facility. A clean room enclosure was first erected and then the specular chamber was constructed inside this enclosure.
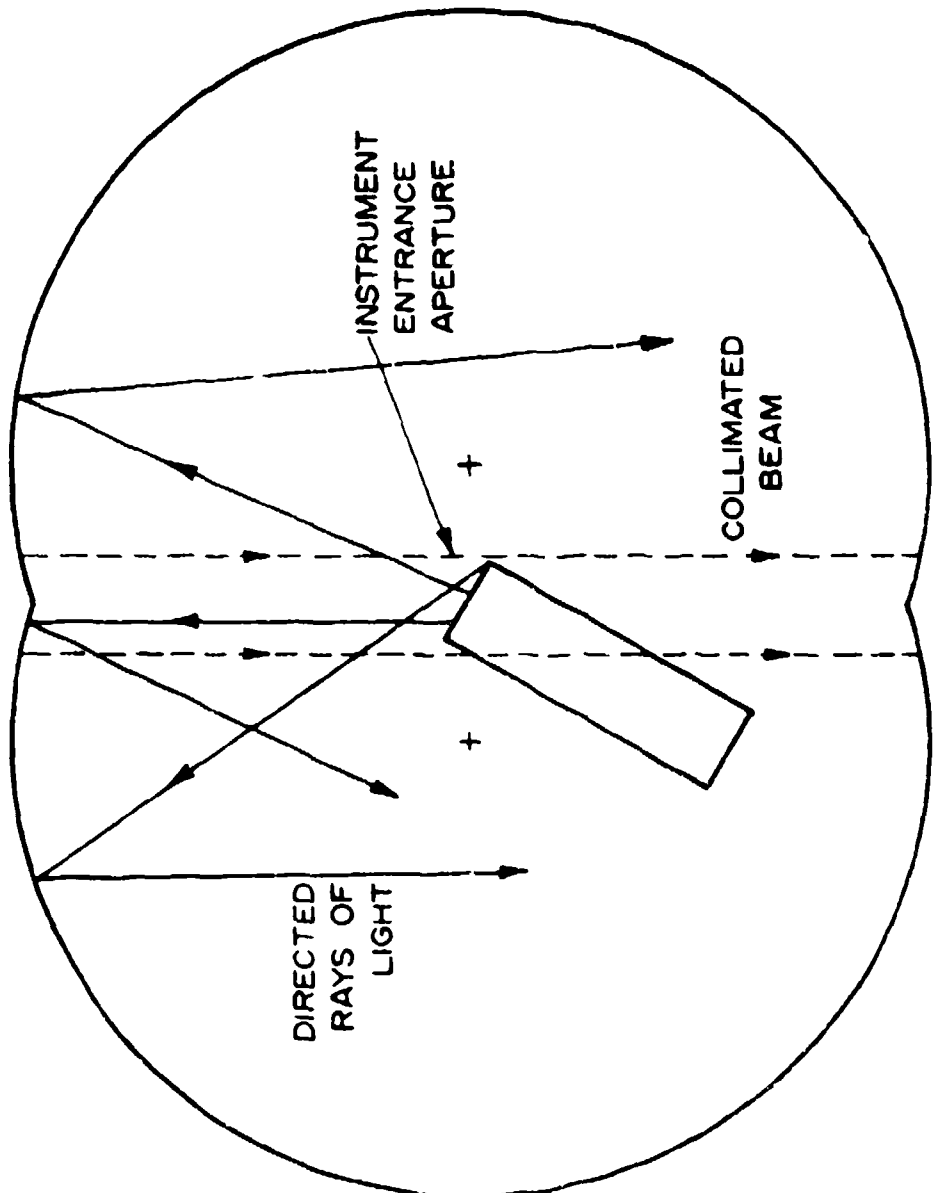
Figure 6. Simple ray trace of a modified circular specular chamber showing the excellent directional properties.

The principle of a clean room is to circulate air which has been cleaned by high efficiency filters through the work region without turbulence to ducts which return the air to the blower/filter unit where it is refiltered and recirculated. This air movement will carry any particulate matter out of the room to the filters if the air is moved through the room in a laminar flow fashion so that only a single pass is made through any given region of the room.

Five filter/blower units for a vertical flow clean room were obtained. These units are designed to meet class 100 clean room specifications, i.e., under the proper operating conditions there will be less than 100 particles of 0.5 μm and larger maximum linear dimension per cubic foot. A supporting frame in a size that the five filter/blower units could maintain laminar flow throughout the region enclosed by the frame was constructed and the units were mounted in the ceiling of the frame such that the ceiling was air-tight around the blowers. Partial walls extending from the ceiling down to about 20 cm from the floor were added to act as ducts to return the air to the filters. The blowers force the air down through the high efficiency filters. It flows in a laminar fashion vertically through the clean region, under the partial walls, and is forced through the return ducts back to the blowers as shown schematically in Figure 7.

The ducting walls, the ceiling, and the bottom screens of the filter/blower units are all painted a dull black. The floor of the enclosure is covered with a black shag carpet which was selected by test as the least reflective of the sample set. The shag presents a very rough surface with many absorbing pockets and is very efficient in trapping radiation.

A complete wall, including a tightly fitting door, was constructed to isolate the clean enclosure to maintain its cleanliness. The anteroom thus created is a convenient area to locate the electronics support equipment required to measure off-axis response. This inner door is also light tight so that the measurement is made in the absence of ambient light by the aid of remotely actuated equipment.

The specular chamber was made in the desired modified cylindrical shape by constructing a plywood rib structure of the appropriate shape and fastening 1.6 mm thick black acrylic sheet (Plexiglas G) to the inside. The specular walls
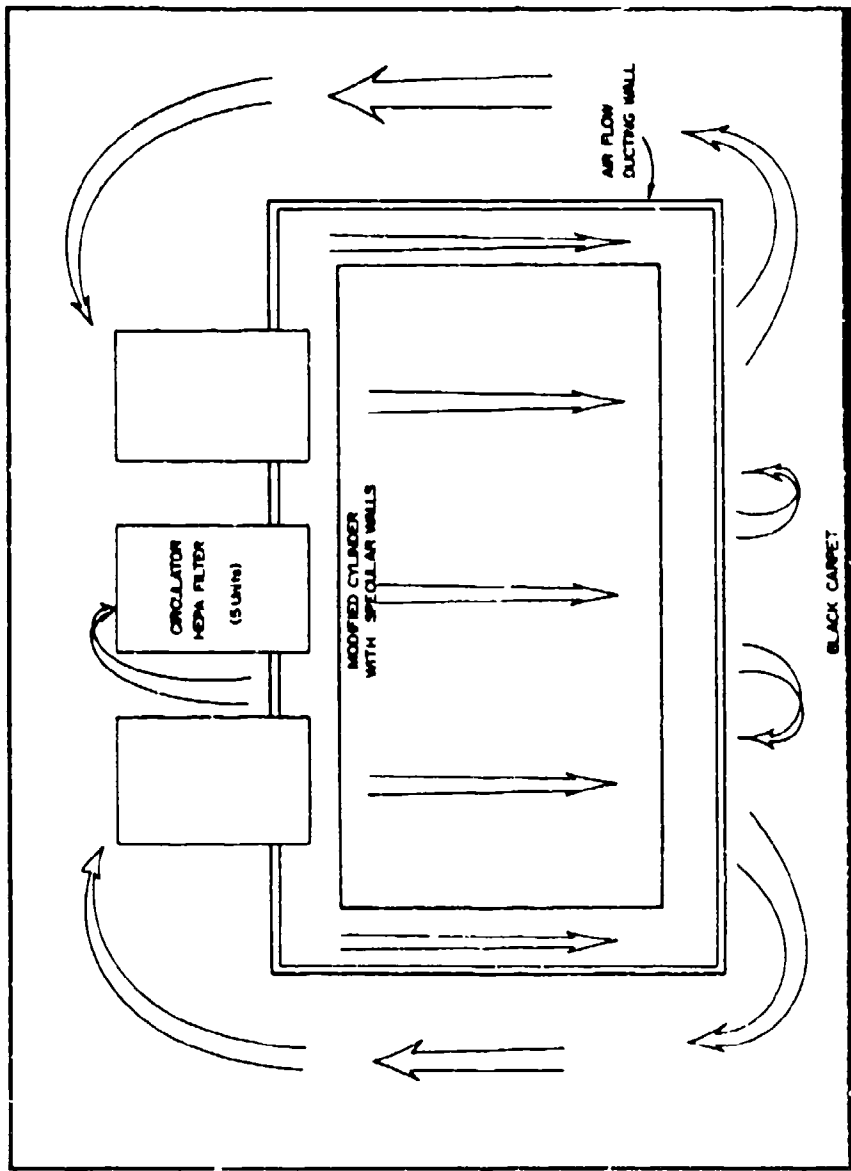
VERTICAL FLOW CLEAN ROOM

Figure 7. Schematic of air circulation in the vertical flow clean room.

are 190 cm high, the radii of the cylinders are 95.6 cm and the centers of the cylinders are spaced apart by 32 cm. The black acrylic plastic was selected as the specular lining material after testing indicated that it had high absorptivity and primarily specular reflectivity.

This shell is suspended 30 cm above the floor. Ports 11.4 cm in diameter were cut in the specular material at $\theta = 0^{\circ}$ and $\theta = 180^{\circ}$ in the vertical center of the chamber for the collimated beam to enter and exit so that the chamber itself would not scatter the collimated beam. A light trap is located outside the exit port to prevent any radiation from scattering back into the chamber.

A remotely actuated rotating platform is fixed to a hydraulic table which is used for the instrument mounting pedestal. This platform can be manually raised and lowered to compensate for any differences in height of the instruments being tested and can be rotated with remote azimuth readout to any desired angle. An instrument holder fixed to the rotating platform can be manually adjusted to elevation angles from -15° to $+15^{\circ}$.

The specular chamber is kept unobstructed and free from unnecessary scattering surfaces by locating the collimator and the light source outside of the specular walls and cutting slightly oversize entrance and exit ports in the specular walls to admit the collimated beam into and out of the chamber. This also keeps any radiation scattered off the edges of the collimator elements outside the chamber. A floor plan of the complete specular chamber for off-axis rejection evaluation is given in Figure 8. More details of the collimator, source, and sensing elements are given in the section dealing with the experimental evaluation of the chamber.
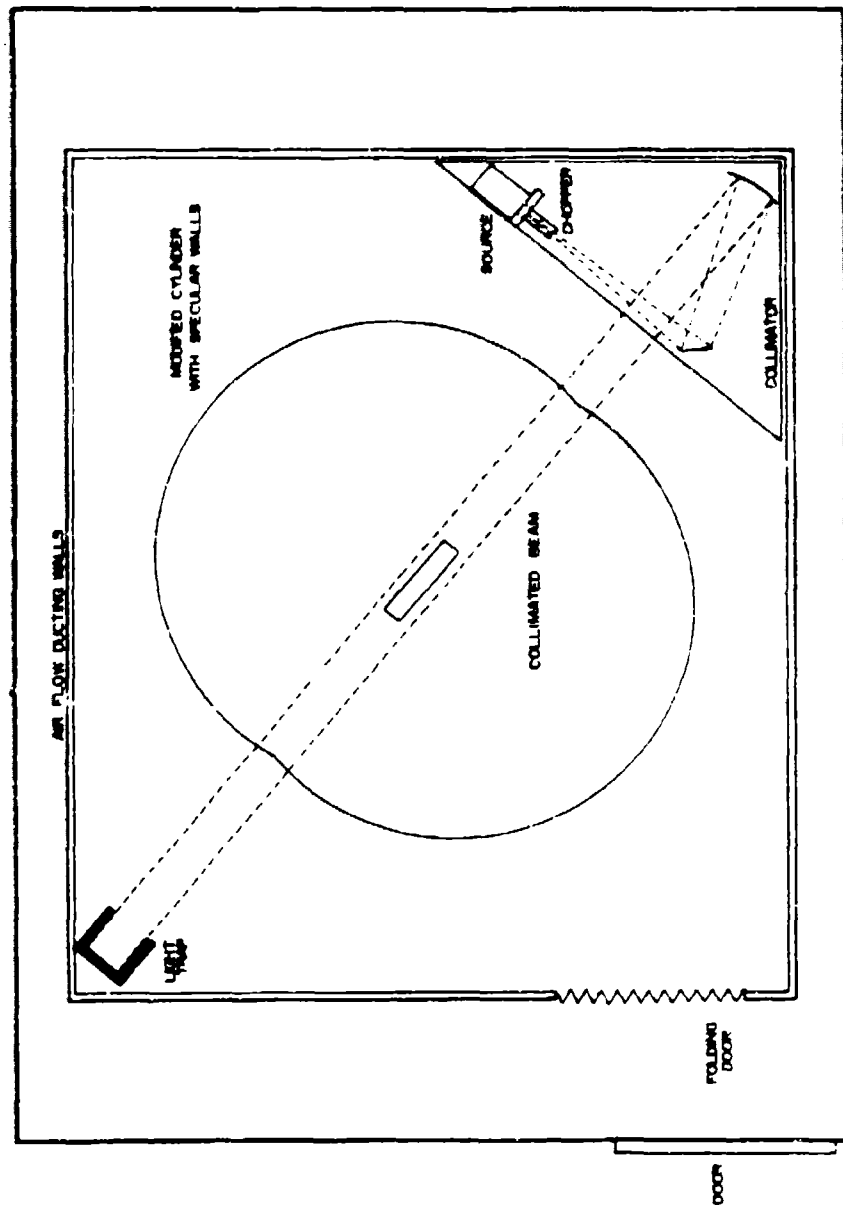
SPECULAR CHAMBER FOR OFF-AXIS REJECTION EVALUATION

Figure 8. Floor plan of the specular enclosure located inside the clean room.

THEORETICAL EVALUATION OF THE SPECULAR CHAMBER CONCEPT

Two Monte Carlo computer programs were used to evaluate the effectiveness of the specular chamber concept in suppressing scattered radiation. GUERAP (General Unwanted Energy Rejection Analysis Program) was modified and used to model the effective power scattered off the walls of both the specular design and a comparable chamber with diffuse walls. A new program SCAT was written to calculate the radiant power scattered by molecular and aerosol scattering processes from a collimated light beam to a baffled detector. These evaluations are now described.

Atmospheric Scattering Backgrounds

The off-axis rejection of a baffle can be limited by the scattering from the atmospheric molecules and aerosols in the region immediately in front of the baffle. The volume of interest is determined by the intersection of the collimated beam and the optical field-of-view cone, as shown in Figure 9. A small fraction of the power incident to this volume is scattered in the direction of the collecting optics where it is interpreted as signal. This scattering volume may produce a higher instrument response than the baffle scattering contributes, causing the baffle to appear to be less effective than it would be in a non-scattering (exo-atmospheric) environment. It is impossible to distinguish the atmospheric scattered signal from that produced by the baffle as installed so that the baffle is rotated about its entrance aperture which remains in the collimated beam as shown in Fig. 10.

However the scattering per unit volume of air can be measured independently of the baffle scattering by using the configuration shown in Figure 11. This scheme is hereafter referred to as a "scattering-column measurement." The baffle is moved back a large distance from the center of rotation so that the baffle is directly illuminated only when very close to on-axis. The only signal at the collecting optics is caused by the atmospheric scattering from the

36
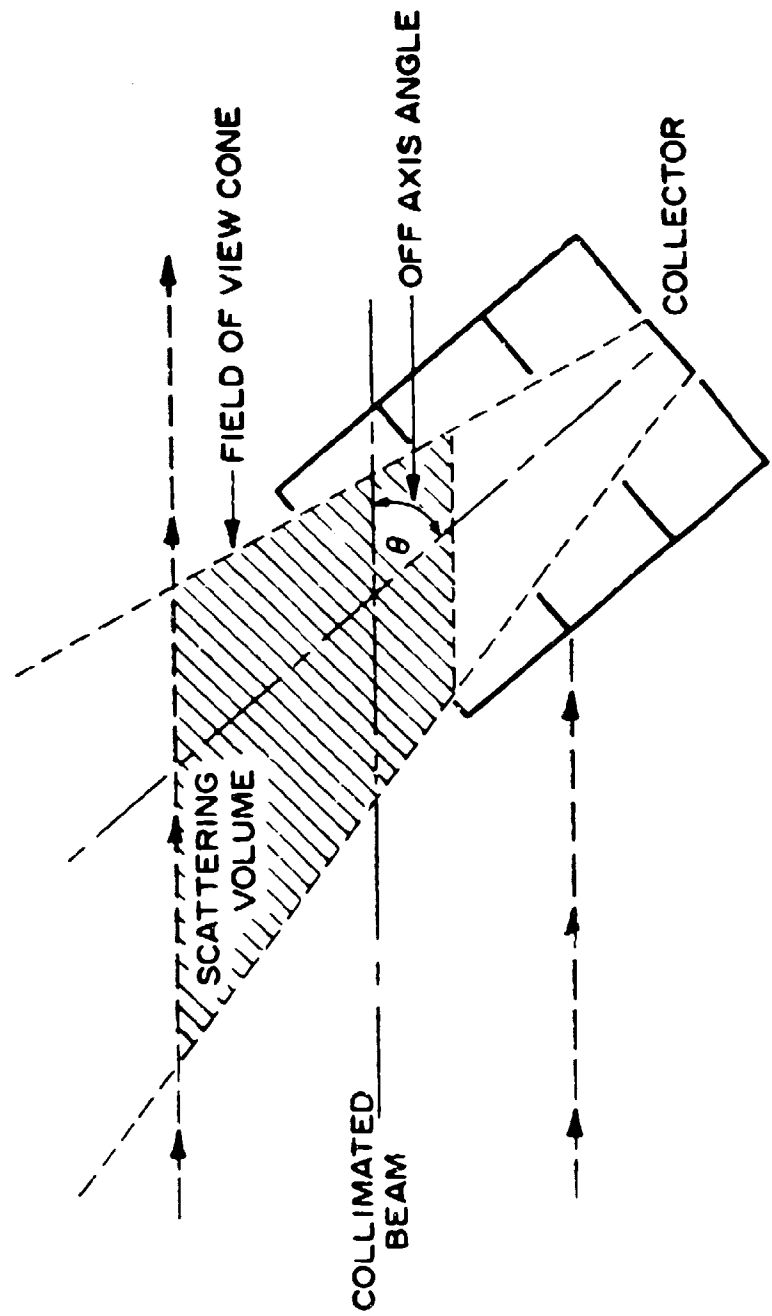
Figure 9. Horizontal cross section through the coplanar axes of the collimated beam and the field-of-view cone showing the scattering volume.

COLLIMATED BEAM

CENTER OF ROTATION
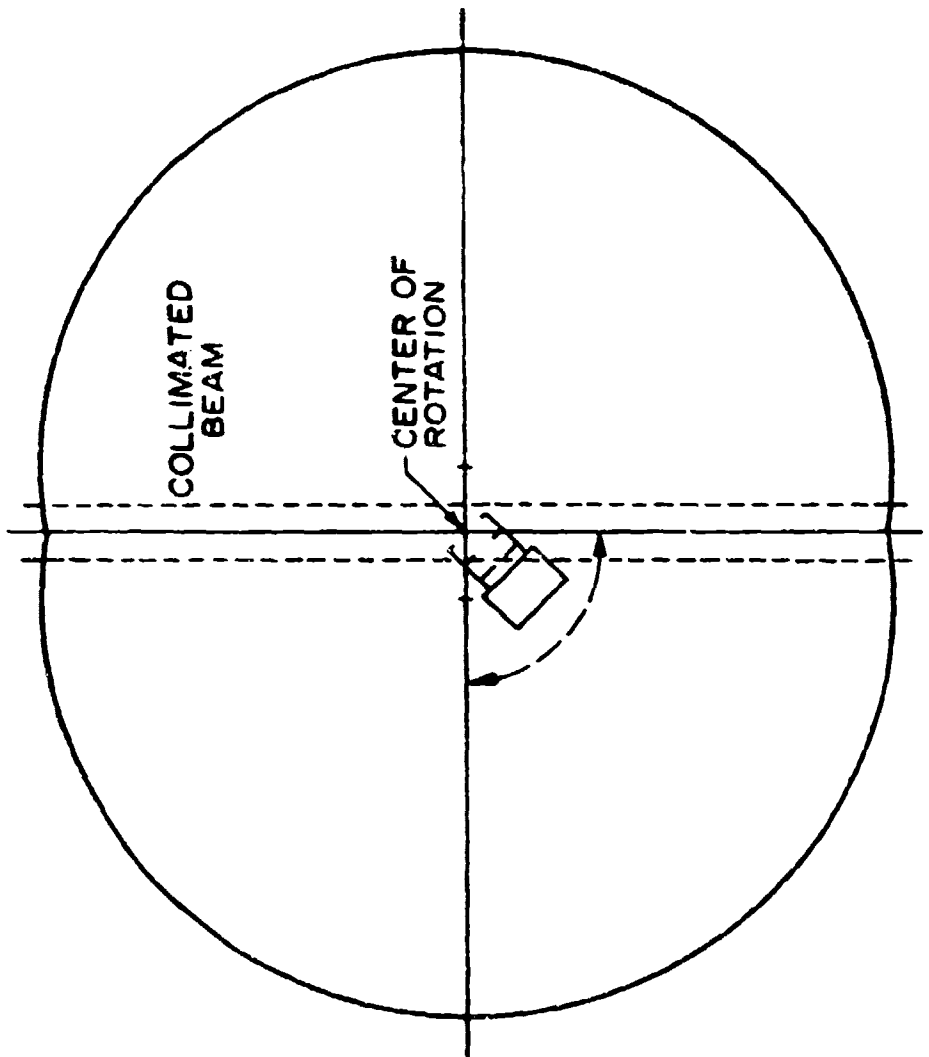
Figure 10. Schematic of the baffle measurement configuration; the baffle entrance aperture remains illuminated by the collimated beam.
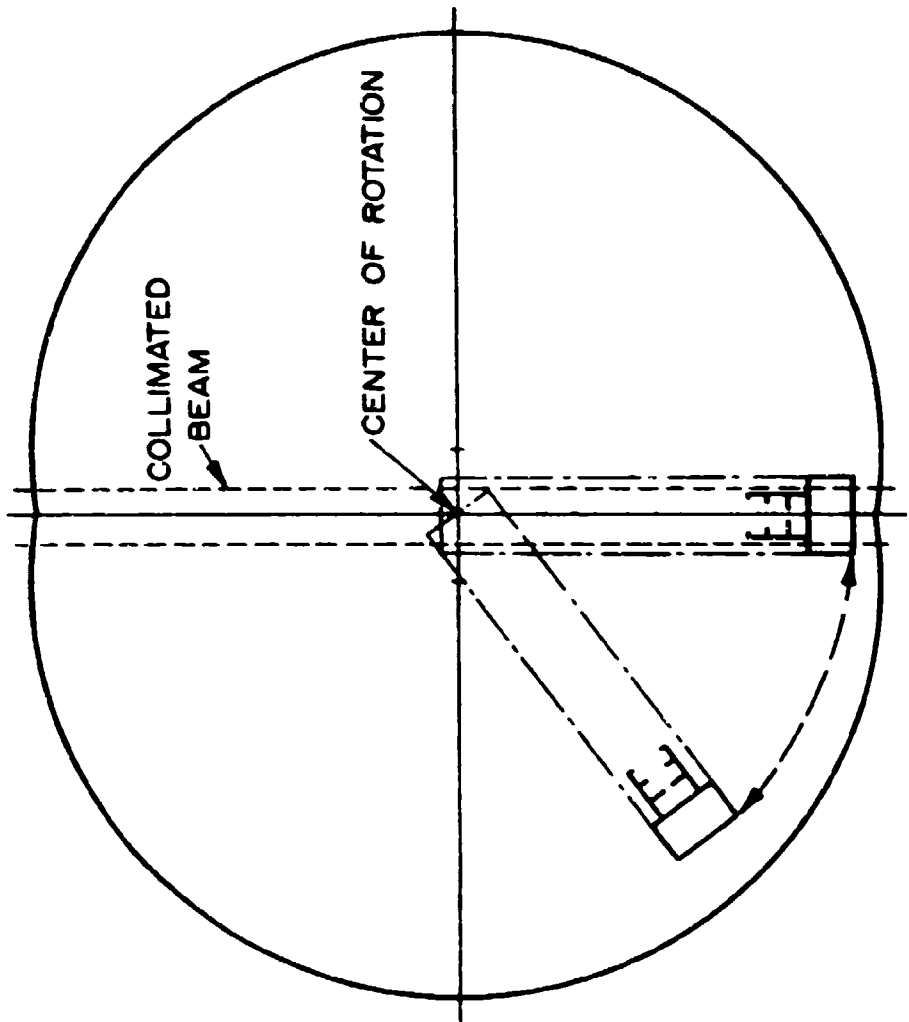
Figure 11. Schematic of the scattering-column configuration; the baffle entrance aperture moves out of the collimated beam.

scattering column, which is determined by the intersection of the collimated beam and the field-of-view cone (no signal arrives at the collecting optics from the chamber wall since the collimated beam strikes no surfaces within the chamber.) This configuration can be used to measure the scattering coefficients for the particular atmospheric conditions of a baffle test. These coefficients are then used to calculate the amount of power contributed by atmospheric scattering during an actual baffle measurement.

A computer program, SCAT, was written to predict the background power level produced by molecular or aerosol scattering (considered separately) for both the scattering-column and the baffle measurement configurations. The approach used to calculate the atmospheric scattering is given along with the resulting computer predictions.

General scattering calculations

The basic quantity of scattering theory is σ, the cross section of each scattering element, which is derived from electromagnetic field theory and has dimensions of cm^2/scatterer (Penndorf, 1957; Kondratyev, 1969). The volume scattering coefficient β is obtained by multiplying the cross section by N, the number of scatterers per unit volume,

$$\beta = N\sigma \qquad (cm^{-1}) \qquad (14)$$

The volume scattering coefficient is useful for calculating the attenuation of a beam of light as it passes through a length L of a scattering medium,

$$E_L = Ee^{-\beta L} = Ee^{-N\sigma L} , \qquad (watt\ cm^{-1}) \qquad (15)$$

where E is the initial arcance [irradiance] ($\phi\ cm^{-2}$) and E_L is the final areance after passing through the scattering medium.

The spatial distribution of the scattered flux is obtained by including a scattering phase function $P(\theta)$ (sr^{-1}) as a factor to account for the angular

40

dependence of the scattering. The product of the scattering phase function and the cross section is sometimes given as the angular scattering cross-section $\sigma_\theta(\text{cm}^2 \text{sr}^{-1} \text{scatterer}^{-1})$ (Penndorf, 1957).

The flux ϕ_e scattered from a scattering element to a collector which subtends a solid angle Ω_c from the scattering element is given by

$$\phi_e = \sigma_\theta E \Omega_c \qquad . \qquad (\phi) \qquad (16)$$

But E, σ_θ, and Ω_c are all functions of the location of the scattering element with respect to the collector and its position within the collimated beam. This positional dependence is denoted by e:pressing the quantities as functions of the position indicator S, so that

$$\phi_e(S) = \sigma_\theta(S) \ E(S)\Omega_c(S) \qquad . \qquad (17)$$

But,

$$E(S) = E_o E_r(S) \qquad , \qquad (18)$$

where E_o is the base areance and $E_r(S)$ is a normalized relative areance factor to account for any spatial variation in the illuminating beam. The solid angle Ω_c can be defined from

$$\Omega_c = \frac{A_c}{r^2} \qquad , \qquad (\text{sr}) \qquad (19)$$

where r is the distance between the collector and the scattering element and A_c is the area of the collector. Thus,

$$\phi_e(S) = \frac{\sigma_\theta(S) \ E_o E_r(S)A_c}{r^2(S)} \qquad . \qquad (20)$$

The total flux ϕ_T scattered by a volume V is found by summing the flux due to each scattering element in the volume,

$$\phi_T = \sum_{N_T} \phi_e(S) = E_o A_c \sum_{N_T} \frac{\sigma_\theta(S) E_r(S)}{r^2(S)} \quad , \tag{21}$$

where N_T is the total number of scattering elements in the volume. This may also be written as an integral,

$$\phi_T = \int_V \phi_e(S) N \, dv = E_o A_c N \int_V \frac{\sigma_\theta(S) E_r(S) dv}{r^2(S)} \quad , \tag{22}$$

where N is the density of scattering elements in the volume (scatterers cm^{-3}) and V is the scattering volume.

The evaluation of Equation (22) by numerical integration is very difficult; the quadratic equations of the surfaces whose intersection defines the scattering volume are difficult to cast into the form of limits on the volume integral. However, these equations are of a form such that it is very simple to determine if a particular point lies within the scattering volume. The solution of the summation form, Equation (21) is ideally suited for a Monte Carlo approach.

The flux collected when the collector is illuminated normally is

$$\phi_o = E_o A_c \quad , \qquad (\phi) \tag{23}$$

where the areance E_o is assumed to be constant over the collecting area[*]. Thus the ratio of the flux scattered at an angle θ to the on-axis incident flux is

---

[*] This assumption was measured to be valid for the particular cases described.

$$R(\theta) = \frac{E_o A_c}{E_o A_c} \sum_{N_T} \frac{\sigma_\theta(S) E_r(S)}{r^2(S)} = \sum_{N_T} \frac{\sigma_\theta(S) E_r(S)}{r^2(S)} \qquad (24)$$

It is undesirable to evaluate Equation (24) for the very large number of scattering elements in a typical scattering volume. Therefore, Equation (24) is evaluated at a large number of sample points in the volume and the sum is multiplied by the ratio of the number of actual scatterers to sample scattering elements.

A section of the collimated beam (which includes the scattering volume) is chosen as a control volume. A number of test points N_c is generated with uniform distribution within this control volume by a random number generator. Each point is tested to determine if it is included within the intersection of the surfaces which define the scattering volume. The number of test points which meet the inclusion criteria is tallied as N_s and the expression $\sigma_\theta(S) E_r(S)/r^2(S)$ is evaluated at each included test point and summed as Γ. Then,

$$R(\theta) = \frac{N_T}{N_s} \Gamma \quad , \qquad (25)$$

where N_T is the total number of scattering elements in the volume. But,

$$N_T = NV \quad , \qquad (26)$$

where N is the density of scatterers as before and V is the volume of the scattering region. The scattered flux ratio is now,

$$R(\theta) = \frac{NV}{N_s} \Gamma \quad . \qquad (27)$$

But the volume V can be determined from the Monte Carlo data as

$$V = \frac{V_c N_s}{N_c} \quad , \tag{28}$$

where V_c is the volume of the control region. Then

$$R(\theta) = \frac{NV_c}{N_c} \, \Gamma \quad , \tag{29}$$

or

$$R(\theta) = \frac{NV_c}{N_c} \sum_{N_s} \frac{\sigma_\theta(S) \, E_r(S)}{r^2(S)} \quad . \tag{30}$$

Equation (30) is statistically accurate provided that a sufficiently large number N_c of test points is chosen so that the scattering volume is uniformly filled with scattering points. By generating 5000 test points in the control volume there was an average of about four points/cm^3 in the scattering volume. The repeatability of the calculations is indicated by performing the calculations for 2500 points at a time and comparing these partial answers with the 5000-point ones. The resultant scattering ratio numbers were indicated to be accurate to about five percent. A listing of the computer program used for these calculations is given in Appendix B.

Rayleigh and Mie scattering

Values for N and σ_e for the cases of molecular and aerosol scattering must now be defined. The angular Rayleigh scattering cross section for a wavelength of .54 μm was calculated to be

$$\sigma_{R\theta} = 2.97 \times 10^{-28} (1 + 0.932 \cos^2\theta) \text{cm}^2 \text{sr}^{-1} \text{molecule}^{-1} \tag{31}$$

for "average" atmospheric conditions at USU. The average number density of air molecules has been calculated to be $N = 2.01 \times 10^{19}$ molecules cm^{-3}. The change in the above numbers for the normal range of pressure and temperature variations at USU was found to be about 5 percent which is about the same magnitude as the source areance fluctuations. Therefore, it was deemed proper to use average values rather than specific values for the specific dates of measurement. The effective wavelength of Rayleigh scattering for the source and detector used was found by normalizing the system composite response curve given in Figure 12 by weighting individual segments with the inverse fourth power of the segment wavelength. The sum was divided by the number of segments and the fourth root of the reciprocal was taken to find the effective wavelength of unit response for a narrow spectral bandwidth.

Volume scattering coefficients for aerosol scattering are given in a tabulation by McClatchey et al., (1972). A value of $\beta = 4.86 \times 10^{-7} cm^{-1}$ is given for a wavelength of .5145 μm at an altitude of 1-2 km for a "clear" atmosphere of 23 km visibility. The angular dependence is given by a normalized scattering phase function in a figure from which

$$p(\theta) = 10^{.3} - .0295\,\theta + 4.22 \times 10^{-5}\theta^2 + 3.97 \times 10^{-7}\theta^3 \tag{32}$$

was obtained by a curve fitting procedure.

The scattering phase functions given in Equations (31) and (32) demonstrate the differing angular dependencies characteristic of Rayleigh and Mie scattering. As evident from Equation (31), Rayleigh scattering is symmetrical about the 90° angle and is equally strong in the forward and backward directions. Large particles scatter mostly forward--the "Mie effect" contained in Equation (32) (Kondratyev, 1969). The angular distribution of Mie scattering is greatly elongated in the forward direction and is not symmetrical about 90°.
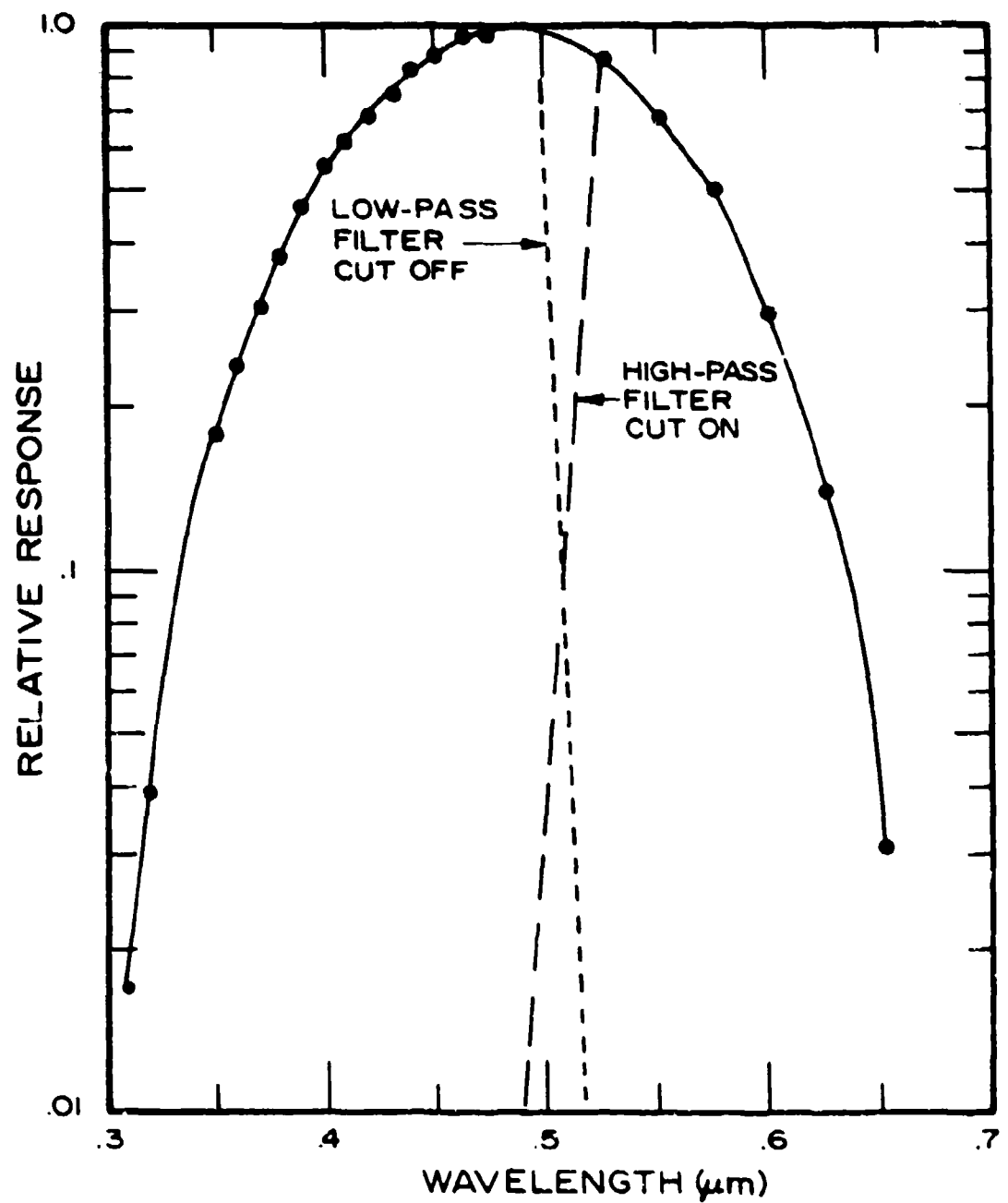
Figure 12. Composite system spectral response also showing the spectral filters used for the wavelength dependency tests.

46

<u>Results of predictions</u>

Predictions of the power scattering ratios for the scattering-column configuration using the above parameter values were computed and are given in Figure 13. Similar predictions were made for the baffle measurement configuration and these results are given in Figure 14.

These calculated numbers appear to agree very well with a general value published for atmospheric scattering by Leinert and Kluppelberg (1974). However, these authors did not specify an off-axis angle and the acceptance angle was ambiguously defined so an exact comparison is not possible.

Background Power Levels Contributed by Surface Scattering

A small amount of the power scattered from the front plate of a baffle may be scattered off the walls of the measured chamber back into the baffle entrance aperture. Thus, the baffle may appear to be less effective than it would be when applied in an environment where there are no scattering walls. It is impossible to measure the magnitude of this scattered contribution from the baffle measurement data. However, digital computer simulation techniques are easily adapted to distinguish between the power scattered off the enclosure surfaces and that striking the baffle entrance aperture directly from the collimated beam. The basic GUERAP program was modified to permit this differentiation.

<u>Prediction of surface scattering background power levels</u>

Four different chambers were modeled for the modified GUERAP program to allow comparison of the surface scattering from different materials and different configurations. Tests were made to determine the reduction in the background power level by changing from a square chamber with diffuse walls to the specially shaped chamber with specular walls. Three different configurations of the specular chamber were then modeled to study the effects of the particular specular material and chamber configuration chosen. The models were designed for ease of comparing materials and shapes, and not for predicting the absolute level of a particular measurement.
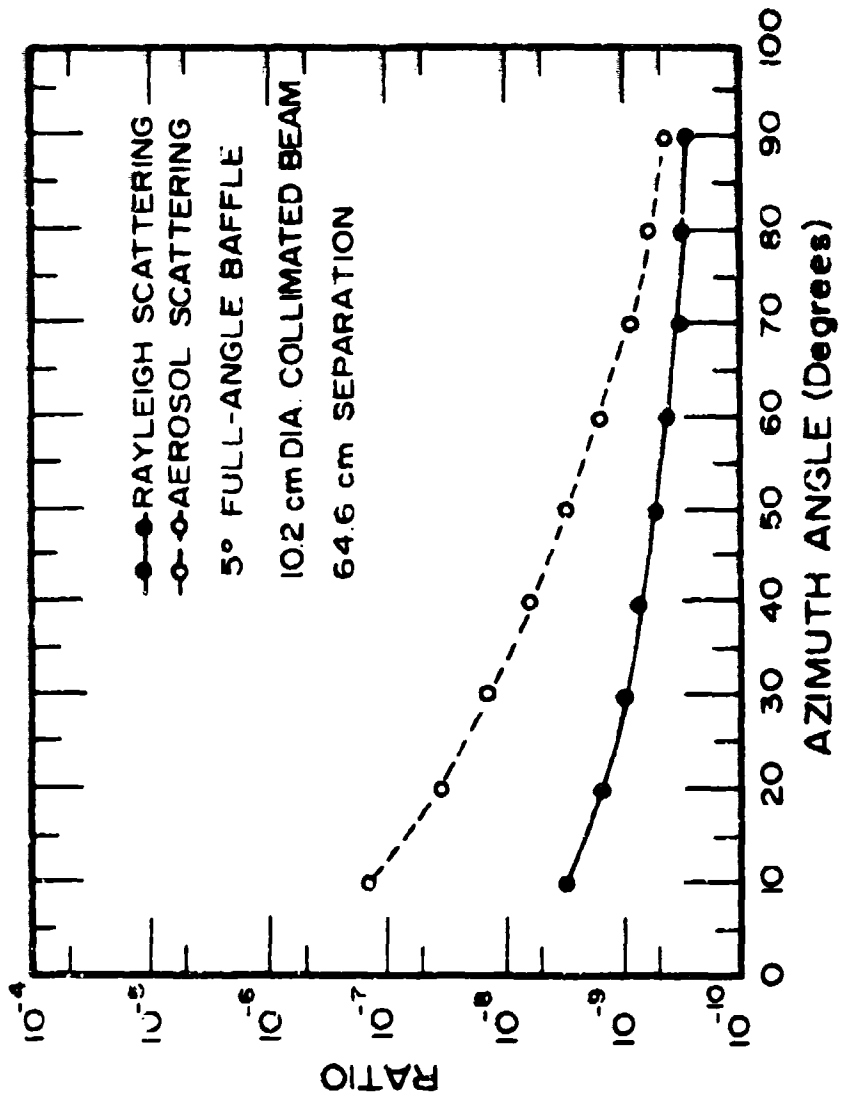
Figure 13. Predicted ratios of scattered to on-axis power for a scattering column measurement.

48
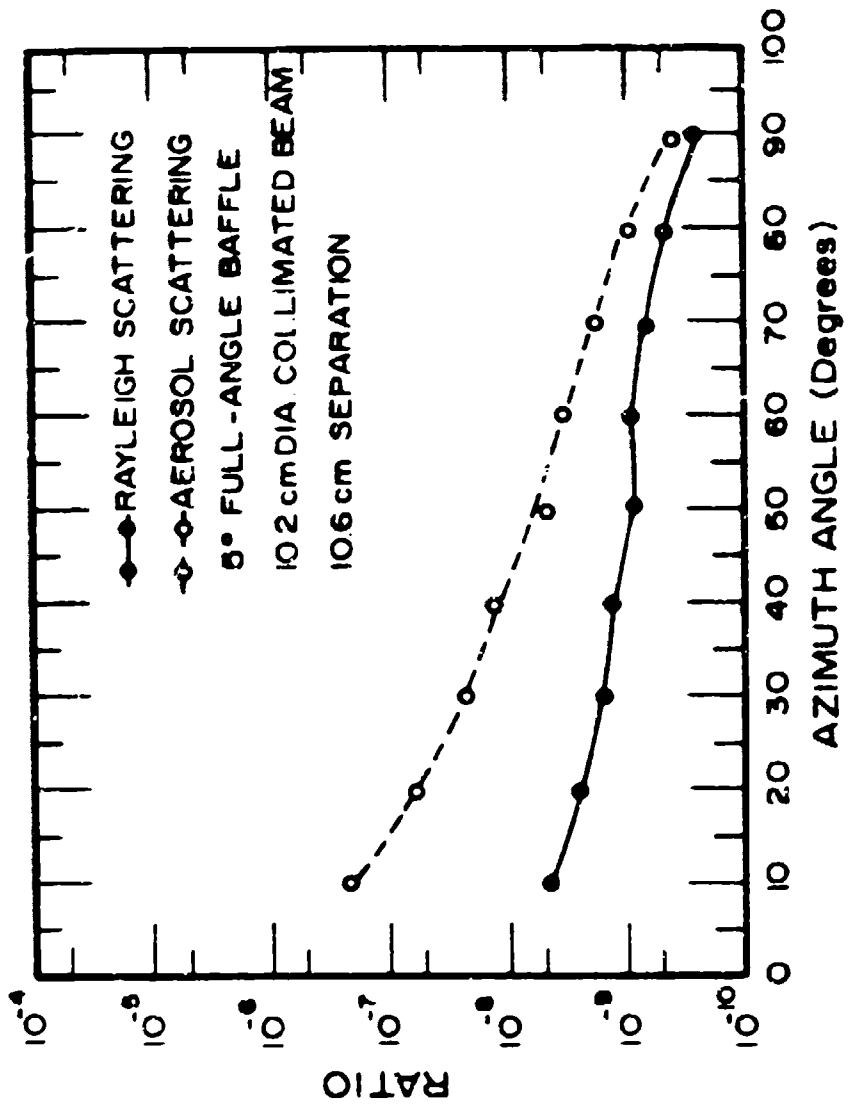
Figure 14. Predicted ratios of scattered to on-axis power for a baffle measurement.

The first model, known as SMC (simple modified cylinder), is shown in horizontal cross section in Figure 15. The walls, shaped in the modified cylindrical form, are modeled with the bidirectional reflectance-distribution function measured for the black plexiglass used in the actual construction. Approximations to the instrument platform and the baffle assembly are also included.* The off-axis angle of rejection $\bar{\sigma}$ is also shown in Figure 15. The angular response of the surface scattered radiation is expected to be approximately flat for angles greater than the baffle cutoff angle because of the cylindrical chamber shape. Therefore, only one angle was modeled. This angle was chosen at 45 degrees for each of the four models. Previous measurements had indicated that at this angle the results were being limited by chamber effects and not by the actual baffle rejection characteristics. A side elevation of the model is shown in Figure 16 which shows the exit port cut slightly larger than the collimated beam so that the chamber itself will not generate scattered power. The dimensions of this model are the same as the specular portion of the actual chamber constructed.

Model SQR, shown in Figure 17, is a square chamber of the same minimum dimensions as the simple modified cylinder but which uses diffuse wall reflectances. The side elevation of this model is the same as for model SMC, as are the baffle assembly and the instrument platform. SQR and SMC are both modeled with completely absorbing ceilings and floors so that the effects of the different wall reflectances are more directly demonstrated.

Model REAL was adapted from the SMC model by adding features to account for the radiation that escapes from the specular portion through the air-ducting spaces between the specular walls and the ceiling and floor as shown previously in Figure 7. The floor and ceiling surfaces are modeled

---

* The importance sampling plane noted in the figure is used in the model to allow the use of a special technique to give more efficient computer time utilization by forcing a statistically accurate portion of the scattered energy to be directed toward the baffle entrance aperture. The wall surfaces to the right of this plane are modeled with this special property.

50
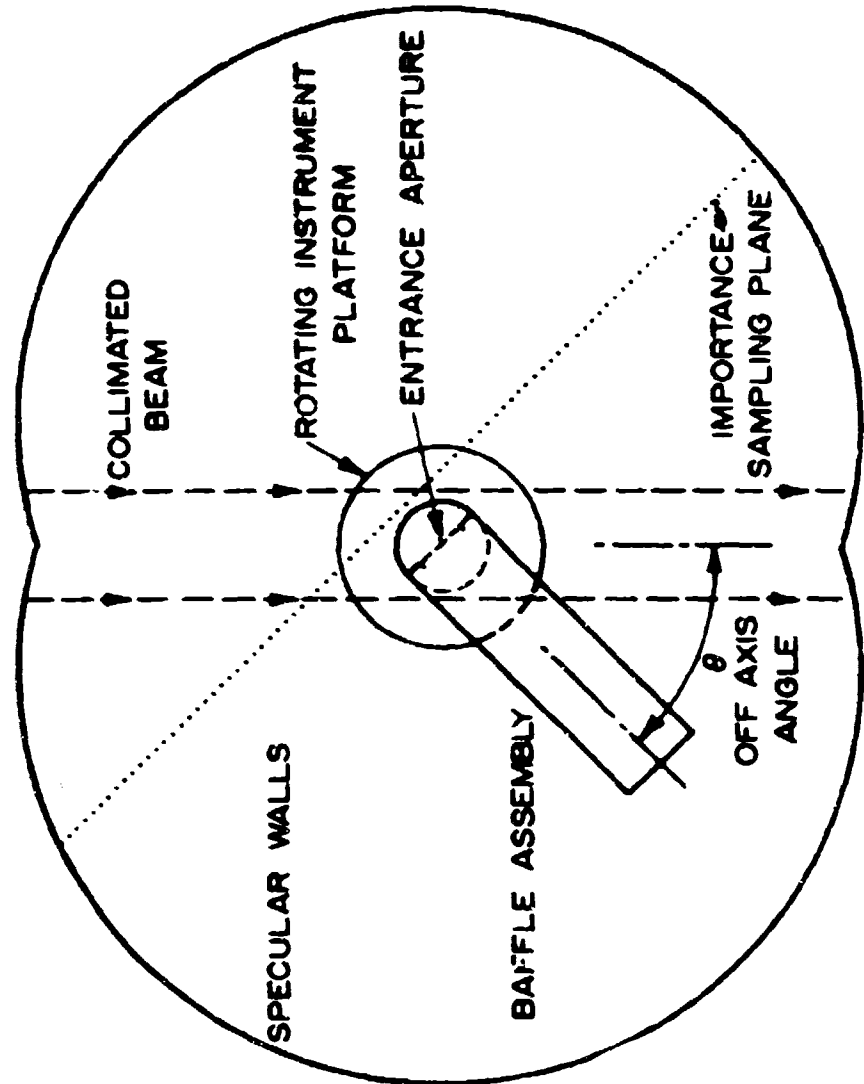
Figure 15. Horizontal cross section of Model SMC— Specular Modified Cylinder.
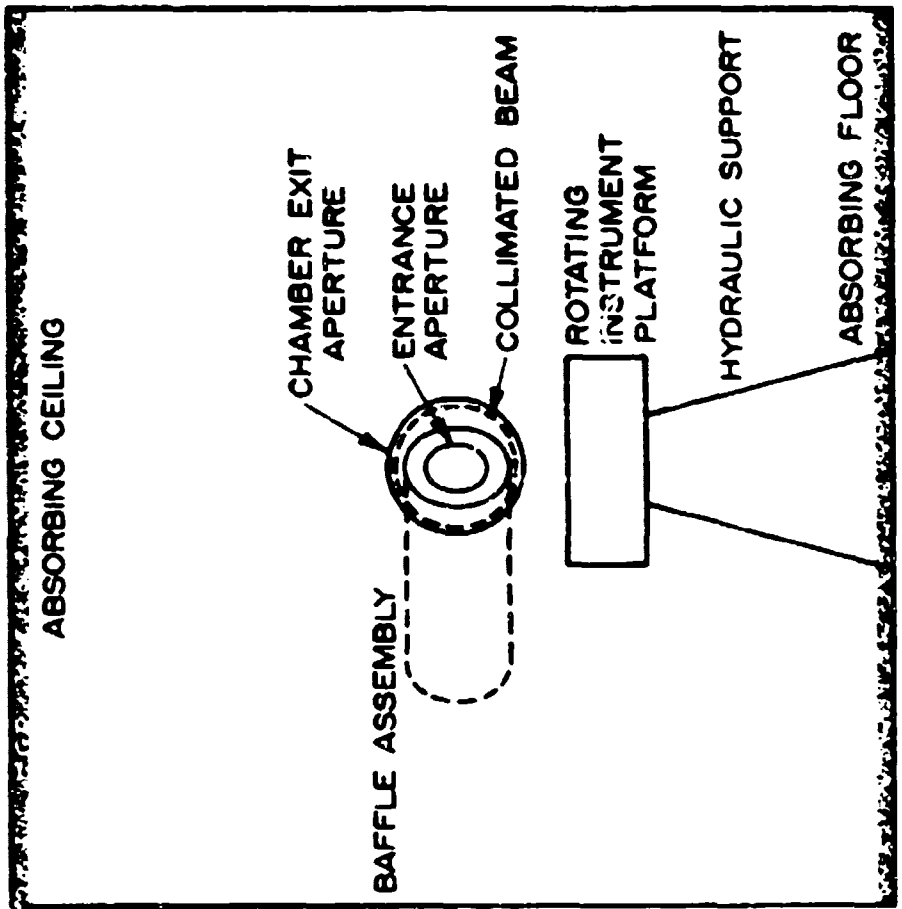
Figure 16. Side elevation of Models SMC and Model SQR.
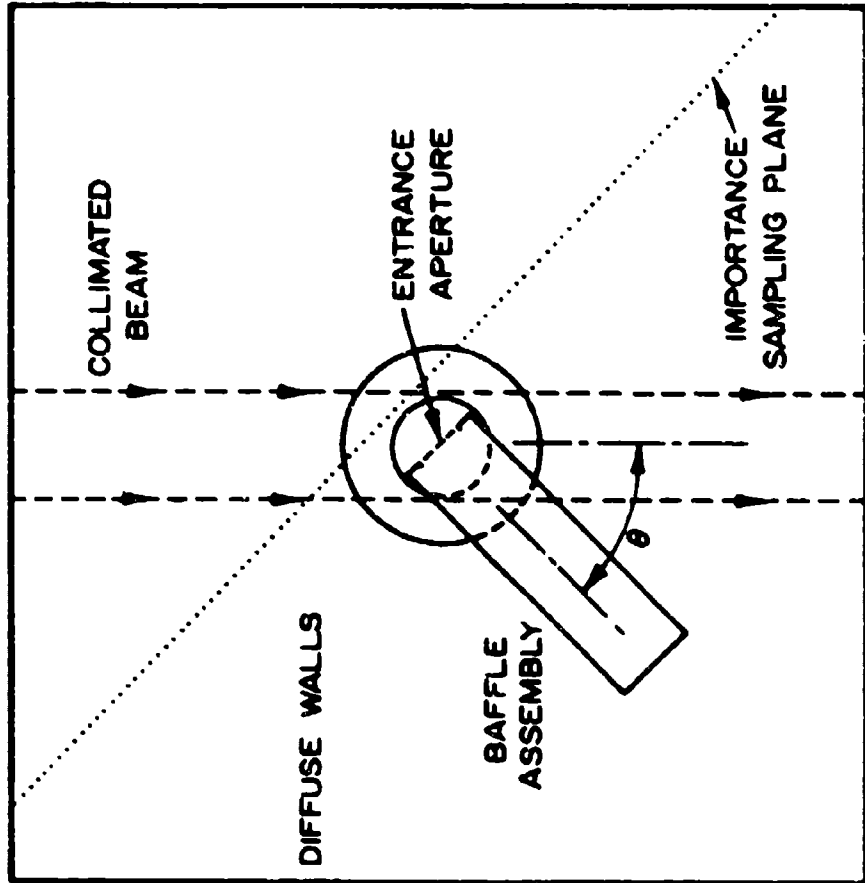
Figure 17. Horizontal cross section of Model SQR —Square chamber with diffuse walls.

by their measured reflectances.* Comparison of the results from models REAL and SMC allows determination if the practical realization is limited by the specular surfaces or by the diffuse ceiling and floor. This model allows radiation to scatter off the floor or ceiling back into the specular region.

Model REAL is modified to model SPEC by eliminating the diffuse component from the specular walls such that they become absorptive and specularly reflecting only. This allows determination if the diffuse component of the specular walls is significant to the chamber operation.

Results of surface scattering predictions

Two elements of the computer data output were most significant in predicting the background level due to surface scattering for the various models:

(1) The total power incident on the baffle entrance aperture due to back scattering off the enclosure surfaces, and

(2) the angular distribution of this scattered power where the angle is measured with respect to the normal of the baffle entrance aperture.
All of the data was normalized to unity on-axis power. Half-degree angular increments were used for the angular distribution tally over the interval from 0° to 12° and the interval from 12° to 90° was taken in one increment for models SMC, SQR, and REAL. Model SPEC used an increment of 4° over the interval from 0° to 80° and a single increment from 80° to 90°.

The values for the SMC model are within the predicted calculation error of the corresponding values for the REAL model when either the total scattered power, the scattered power over the region from 0° to 12°, or the scattered power over the region from 12° to 90° is considered. Thus, the SMC model will not be further mentioned as the REAL model has the same predicted characteristics. That there is no degradation in going from the model with the absorptive floor and ceiling to the model with the measured floor and ceiling

---

* The measured bidirectional reflectance-distribution functions for the various materials used in the chamber construction are given in Appendix D. The conversion of these measured values into parameters for use in the computer model is also given.

reflectances indicates that the chamber is sufficiently deep that the ceiling and floor aren't depreciating the performance of the specular walls.

The SQR model shows 3.2 times more scattered power than the REAL model when the total scattered power incident upon the baffle entrance aperture is compared. The REAL model scatters about twenty times less power than the SQR model when only the power in the interval from 0° to 12° is considered. Over the interval from 12° to 90° the REAL model shows an improvement of 2.9 over the SQR model.

The background power level due to surface scattering (as it would be measured by an actual baffle system) can be calculated by piecewise multiplying the predicted power distribution on the baffle entrance by the measured response of the baffle system. A sunshade baffle response with a 2.5° optical cut-off angle and a primary knife-edge angle at 12.5° (shown in the next section as Figure 27) was chosen as an appropriate baffle response to compare the various models. The angular distributions of the scattered power on the baffle entrances are such that the predicted response from the representative baffle system is a factor of 80 less for the REAL model than for the SQR model. The prediction for the REAL model is that this baffle will be limited by surface scattering at a level of 1×10^{-11} of the incident power when the baffle is oriented at an angle of 45° to the collimated beam, while a similar baffle in a square diffuse chamber would be limited at 8×10^{-10} of the incident power.

The SPEC model is interesting because the computer predicted no power (down to 10^{-15} of the incident power) incident to the baffle entrance at angles less than 44° to the baffle normal. Thus the predicted response to the sample baffle is also less than 10^{-15} of the incident power. The total power incident to the baffle entrance for the SPEC model is about 70 percent of that for the REAL model but it is all at angles far removed from the baffle normal and contributes very little to the total baffle response. Thus, the diffuse component of the specular wall bidirectional reflectance-distribution function does play a significant role in the chamber performance.

The REAL model showed a significant improvement over the SQR model in each of the three domains of comparison as indicated above. However, the absorption coefficient is actually minutely larger for the diffuse material than for the specular material. The difference in the performance of the materials as wall coverings then is determined by what happens to the unabsorbed radiation; whether it is specularly reflected or diffusely scattered. This is confirmation of the desirability of using specular material for the walls if the ultimate in reduction of the surface scattered background is to be achieved.

The results of modeling the surface scattering are summarized in Table 1. Because of the relatively small number of rays considered[*] the error bar in the first three columns is less than ± 25 percent. The error bar in the fourth column is estimated to be ± 50 percent because of the smaller number of rays striking the entrance aperture at angles sufficiently small to be significant in predicting the baffle response.

---

[*]There were 813 scattered rays striking the baffle entrance in the SPEC model which had the smallest number of rays. Because of the inefficient nature of Monte Carlo analysis the cost of test runs with a sufficient number of rays to generate much smaller error bars quickly becomes very large.

Table 1. Predicted power backscattered from enclosure surfaces to baffle aperture when baffle is oriented 45° to collimated beam (for on-axis incident power equal to one watt).

Model	Total Power (Watts)	Average Power 0° to 12° (Watts/degree)	Average Power 12° to 90° (Watts/degree)	Predicted Response from 5° full angle baffle (Watts)
SQR Square Diffuse	4.2×10^{-7}	17×10^{-10}	49×10^{-10}	5×10^{-10} *
REAL Real Chamber (measured reflectances)	1.3×10^{-7}	$.55 \times 10^{-10}$	17×10^{-10}	1×10^{-11} *
SPEC Perfectly Specular Chamber	$.89 \times 10^{-7}$	0 **	13×10^{-10} **	$\leq 10^{-15}$

* Because of few data points these values may be in error by 50%.
** There is no power incident at less than 44° to the baffle normal.

MEASURED PERFORMANCE OF THE SPECULAR CHAMBER

This section discusses the measurements used to qualify the performance of the specular chamber in reducing the background power due to atmospheric scattering and in directing the surface scattered radiation away from the baffle entrance. The experimental setup used in these measurements is described first. The second subsection discusses the techniques used and the results of the atmospheric scattering measurements. The measurement of the background power level due to surface scattering, including techniques and results is then discussed. Finally the extension of a baffle measurement below the chamber background level is described.

Experimental Equipment

The equipment used to measure the performance of the specular chamber can be divided into four functional groups:

1. Radiation source and collimator.
2. Radiation detector with a defined field of view.
3. Rotating instrument platform with angle indicators.
4. Control console with readouts.

Radiation source and collimator

A 500 watt tungsten-halogen lamp (G. E. type EHA which has a rectangular filament with an area much larger than the source aperture) is used as the source of radiant power. This lamp is mounted in a specially designed lampbox (with forced air cooling) which blocks all radiation except that passing to the variable speed enclosed chopper. The lamp is controlled by a variac; this combination has been found to regulate the output power to within 5 percent. The chopped light from the source is passed through an interchangeable aperture which controls the source power transferred to the collimated beam and also

the divergence of the beam. A baffled tube limits the divergence angle of the source to that needed to fully illuminate the collimator.

The collimator is made using a 10.8 cm diameter spherical first surface mirror with a 114 cm focal length. This spherical mirror has a minimum blur diameter as small as that of a diffraction limited parabolic mirror of the same size. A reflecting system was chosen for the collimator because of the reasons mentioned previously. An 8 by 10 cm folding mirror is used with the collimating mirror in a Herschel configuration to avoid any obscuration of the collimated beam. The source aperture for these tests was 0.136 cm, for which the divergence of the collimated beam is calculated to be less than 0.16 degree. Coma was also calculated and found to be much less than the divergence.

The areance uniformity across the beam was measured by co-aligning a photometer with the beam, and then shifting the photometer horizontally through the beam and noting the relative response. A plot of this measured areance is given in Figure 18. A normalizing procedure was applied to the measured areance distribution (assuming that the distribution was also radially symmetric in the vertical direction), and it was determined that the effective area of a collimated beam of uniform areance equal to the peak areance of the 10.2 cm diameter collimated beam was 80.5 cm^2. This corresponds to an equivalent normalized diameter of 5.75 cm. The areance variation across the beam is characterized by the equation

$$E(R) = .9923 - .00807R - .015R^2 - .0318R^3 + .00548R^4 , \qquad (33)$$

where R is the radius from the center of the beam in cm. This collimated beam areance variation was entered into the computer program used to predict the atmospheric scattering, so that these predictions would be based upon the actual measurement conditions.

The baffle measurements reported herein are subject to some systematic error because of this collimated beam non-uniformity. The edge of the baffle entrance aperture is not being illuminated by the same areance value that the
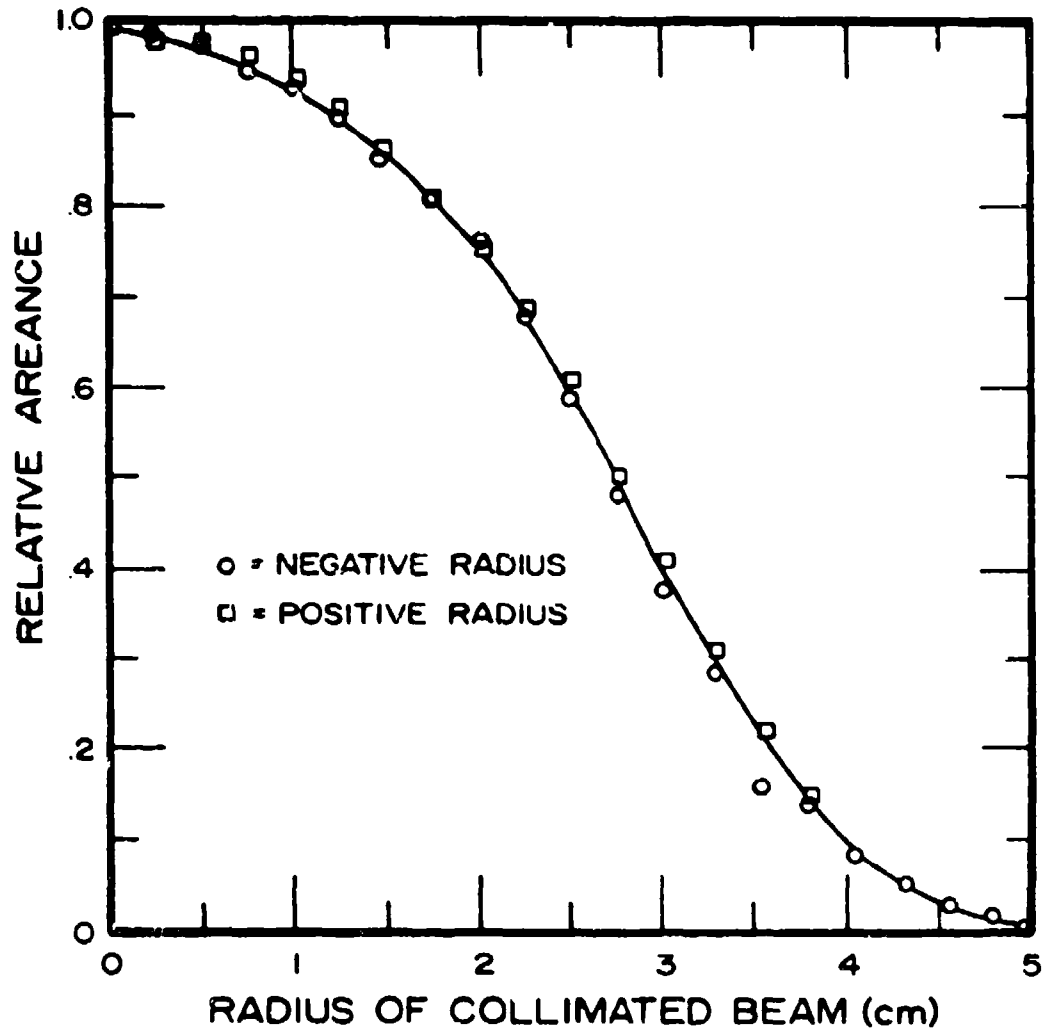
Figure 18. Variation of source areance with radius of collimated beam.

objective lens receives when the on-axis reference level is measured. Thus, the effective true reference level (as far as the baffle edge is concerned) is equal to the relative areance at the baffle edge radius. At 2.33 cm (the radius to the entrance aperture edge for the baffle used in all of the measurements), the local areance is only 0.68 relative to the central value.

This effect is reduced as the off-axis angle increases because the entrance aperture becomes an apparent ellipse when viewed from the collimator source. Thus, the apparent width of the entrance becomes 2.33 cm x $\cos\theta$, where θ is the off-axis angle. The apparent width at 40° is 1.78 cm, for which the relative areance is 0.81; the apparent height is still 2.33 cm. The power scattered off the baffle entrance edge for a 40° off-axis measurement will be low by a factor of between 1/0.81 and 1/0.68 i.e., about 1.35.

A correction for this error was not applied to any measurements because it is a function of the off-axis angle and of the incremental areance variation. Also, a similar error exists for each of the inner baffle edges and the proper weighting function for each of the edges is also a function of angle and is not known. The many interactions involved between the several knife edges and the non-uniform beam areance coupled with the higher baffle response at small off-axis angles where the non-uniformity effect is greatest lead to the postulate that the maximum relative error is less than 30 percent.

This same effect reduces the scattered light off the baffle front surfaces and from the atmospheric scattering because of the smaller relative areance of the outer regions of the collimated beam. For an optimum off-axis rejection measurement the collimated beam would be uniform and just large enough to barely overfill the baffle entrance aperture. The 10.2 cm diameter beam was used for the tests reported herein because it was more uniform out to the radius of the baffle entrance aperture than was the smaller diameter beam. The use of this larger than necessary diameter compensates for the nonuniformity of the collimated beam and the chamber limitations determined from these measurements are very realistic.

This experimental setup cannot be used to measure high rejection at angles less than 5°; the scattering off the collimator mirror and from the edges of the mirrors, source apertures and chamber entrance port would render the result meaningless. This setup is appropriate for the evaluation of sunshade baffles with the primary critical angles beyond about 8°.

Radiation detector

An RCA type 4517 photomultiplier tube in a special housing with an integral transimpedance preamplifier was used as the radiation detector for the qualification tests reported herein. This photometer assembly was fitted with a lens of 1.25 cm clear aperture and a field stop to produce a field of view with a 2.5^o half angle. This enabled the photometer to be used with a standard baffle from the NR-4 Dual Channel SWIR Radiometer which has critical baffle angles at 12.7^o and 40° and which has good off-axis rejection characteristics. The measured field of view of this combination is given later as Figure 27. All tests were performed using this baffled photometer; with one exception to be noted later, tne wavelength response was determined solely by the source and pm tube characteristics. The spectral response of this combination was given previously as Figure 12.

The performance of a baffle which had all of the inner surfaces painted with 3M "Nextel" 101-C10 Black Velvet Coating was compared with one which had been especially prepared with the Martin Marietta Black Surface applied to all of the inner surfaces. The Martin Marietta Black Surface baffle demonstrated an off-axis response a factor of two lower than the black painted baffle over the region from 16 to 40°. Therefore, the specially prepared baffle was used in all of the following tests.

Rotating instrument platform

A 25.4 cm mill table has been fitted with a variable speed motor to provide remote azimuth control. A precision ten turn potentiometer is coupled through a slip bearing to the rotating table and serves as a sensor

for remote azimuth indication. This angle indication is good to about ± 0.06 degrees. The slip bearing arrangement allows the angle readout to be zeroed independently of the rotating table position; this extends the useful range of the azimuth angle readout to the full 360 degrees of rotation without sacrificing the resolution of a 90 degree total range.

The photometer assembly is fitted to the rotating table by means of an instrument platform which allows the elevation angle to be manually read and adjusted. This platform also separates the photometer from the scattering surfaces provided by the rotating table. Appropriate switches and connections allow the rotating table to be read and controlled from inside the chamber as well as outside for ease in alignment and angular calibration.

Control console

A control console is located outside of the clean, dark region so that the measurements can be made remotely after the initial set up. This console controls the direction and speed of rotation for the instrument platform, and also houses a variable scale circuit for the angular readout. There is also a chopper speed control and the output circuitry for the chopper reference signal used for synchronous detection. The source areance control and photomultiplier tube high voltage supply are also located in the console. A Princeton Applied Research Model 186 Synchro-Het phase lock amplifier was used to demodulate the chopped signal and when used with the fold-back technique discussed earlier provided about eleven orders of dynamic range.

Measurement of Limitations Imposed by Atmospheric Scattering

Description of the measurement technique

The experimental equipment described above has been used with the specular chamber in a series of experiments to evaluate the performance of the facility and to determine the actual limitations present in the physical implementation of the concept. The atmospheric scattering was first measured using the

scattering-column configuration, (previously shown in Figure 11) with the lens aperture located 64.6 cm from the platform axis of rotation. The collimated beam was 10.2 cm in diameter.

The power indicated by the sensor was recorded on axis and at many off-axis angles. The total signal from these off-axis measurements beyond about 10° is due to atmospheric scattering. Once the baffle is rotated out of the collimated beam there are no other surfaces which can scatter the radiation. (The collimated beam is smaller than the entrance and exit ports cut into the specular walls.) The results of these measurements are plotted and compared with the predicted values in Figure 19.

This configuration is also useful for determining the magnitude of the signals scattered off the specular walls relative to the signal scattered by the atmosphere. When the baffle was at angles of 40 and 90° to the collimated beam, a section of black carpet was placed to block the beam ahead of the scattering volume and to scatter the light onto the chamber walls. When this was done the signal dropped about an order of magnitude from the purely atmospheric scattered signal, indicating that the scattered radiation off the walls is about an order of magnitude below the atmospheric scattering.

The baffle measurement configuration (see Figure 10) where the plane of the baffle entrance aperture is rotated about the axis of rotation of the instrument platform was next employed. The lens aperture was now 10.6 cm from the axis of rotation. The results of this measurement are plotted along with the predicted values in Figure 20.

The previous measurements indicated by the shape of the response that the atmospheric scattering was predominantly Rayleigh in nature. This was further demonstrated by utilizing the fact that Rayleigh scattering is inversely proportional to the fourth power of the wavelength while Mie scattering does not follow a fourth power dependency. The baffle measurements were repeated with two different wavelength filters to modify the spectral response of the basic source-sensor combination. A high-pass filter which blocks all radiation below 0.52 μm and a low-pass filter which blocks all radiation between
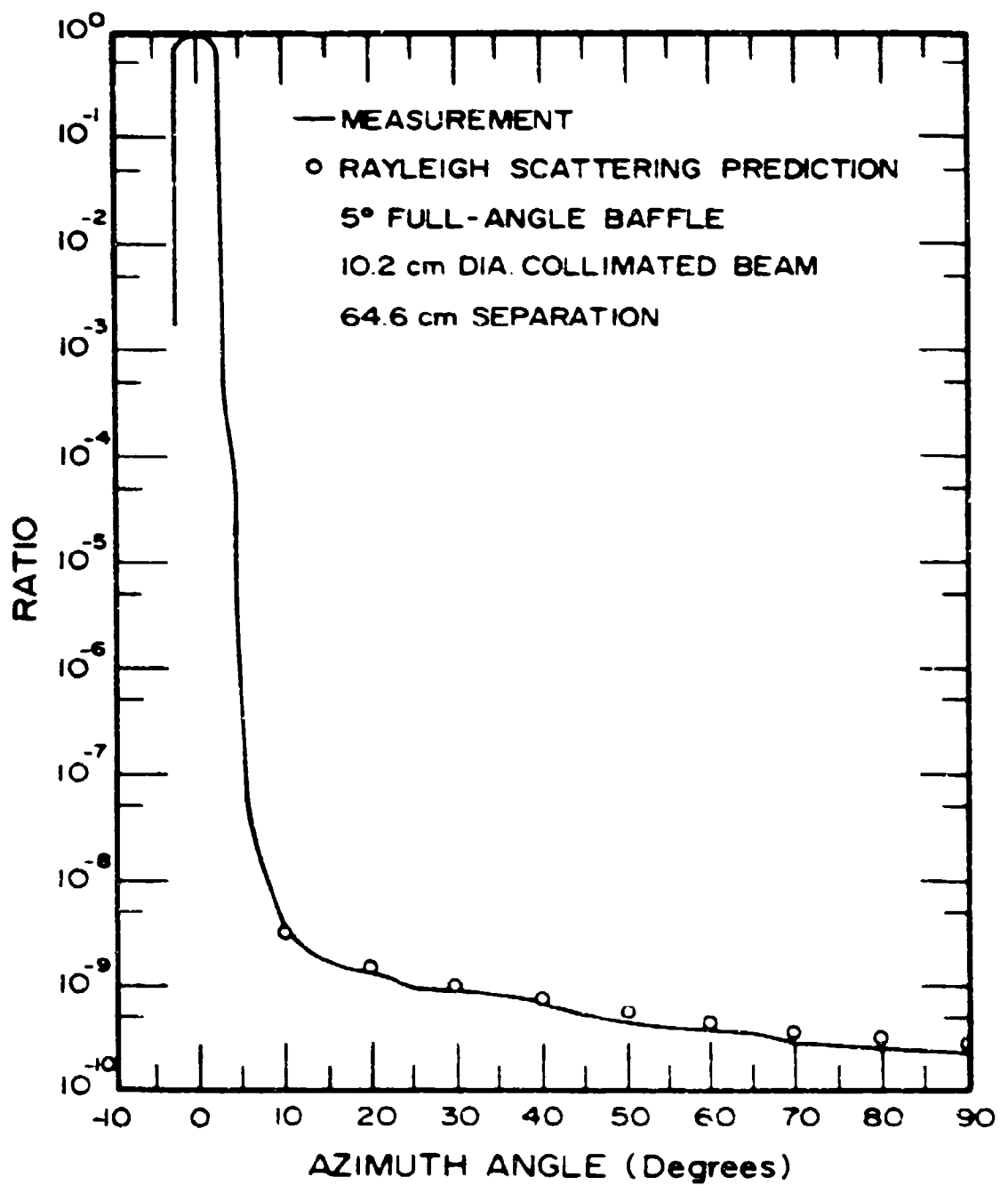
Figure 19. Measured and predicted ratios of scattered to on-axis power for a scattering-column configuration.
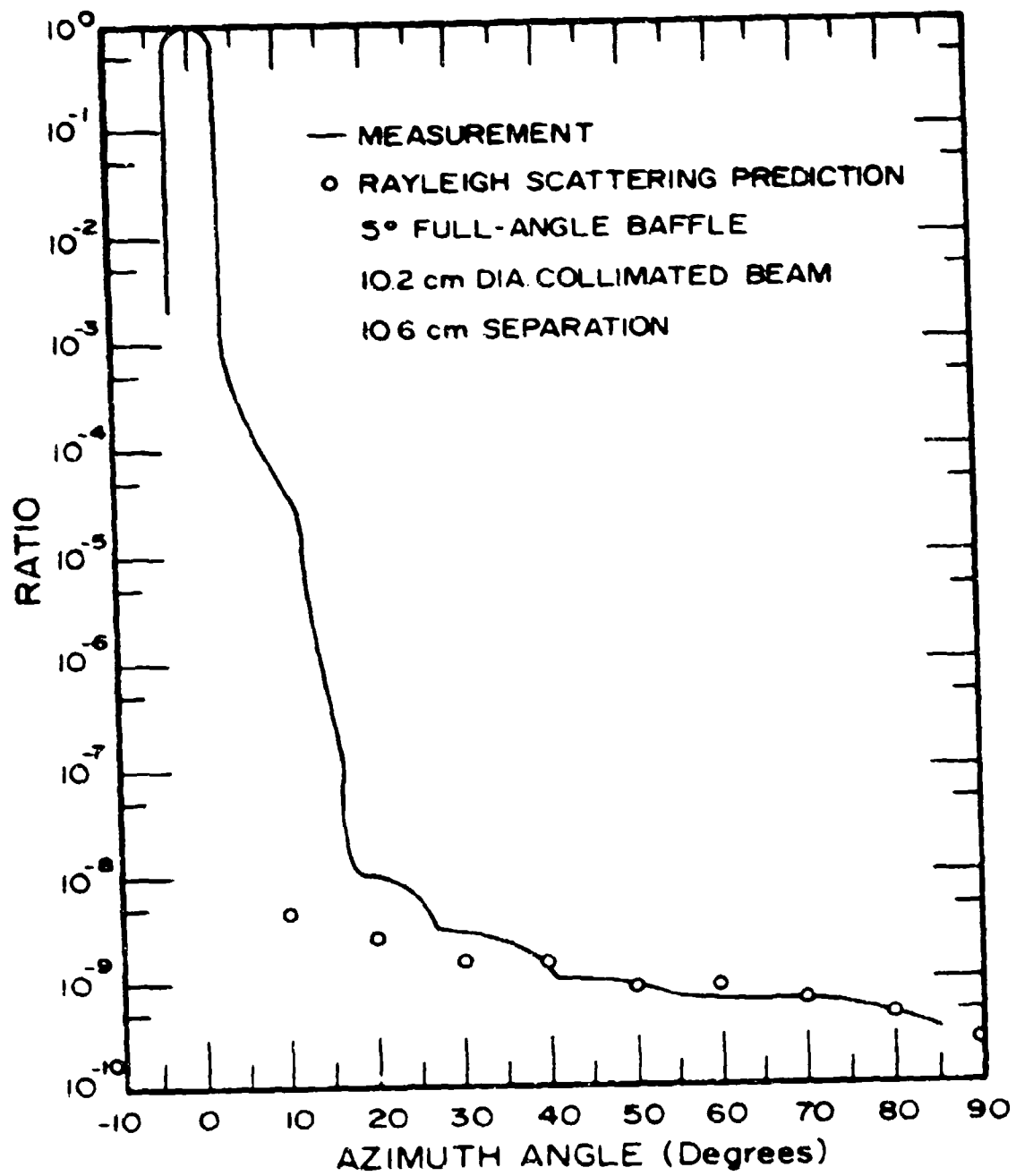
Figure 20. Measured and predicted ratios of scattered to on-axis power for a baffle measurement configuration.

0.50 and 0.67 μm were used. The relationship of these filters to the normal system response was previously shown in Figure 12. The results of this test are plotted in Figure 21.

Discussion of atmospheric limitation measurements

The measured results of both the scattering-column measurement and the baffle measurement configuration agree very well with the predictions obtained by considering Rayleigh scattering alone. Particularly significant is the fact that the shapes of the measured responses conform so well to the predicted shapes for the Rayleigh scattering situation. The scattering phase functions which determine the angular shapes of the scattered power ratios for Rayleigh and aerosol scattering are very different as was indicated in Figures 13 and 14. In addition to a more gentle slope, the Rayleigh scattering phase function is symmetrical about 90° whereas the Mie scattering phase function continues to decrease out to about 120°. This symmetry about 90° was observed in the measurements. The Rayleigh shape of response indicates that the clean-room techniques have eliminated any significant scattering from atmospheric aerosols. Measurements made before the air filtering system was operating, however, did exhibit a shape indicative of a combination of Rayleigh and aerosol scattering.

The values measured in the wavelength dependency test provide striking verification that the limiting background of the chamber is determined by Rayleigh scattering. The normalization technique previously used to determine the effective wavelength of the broadband system was used to determine effective wavelengths for the high-pass and low-pass filtered systems. Then inverse fourth powers of these wavelengths (.664 μm and .515 μm) were calculated; the ratio is 2.76. The average ratio of the two responses over the region from 40 to 70° * was 2.85 with the long wavelength having the smallest scattered power ratio. This is clear confirmation that the specular chamber performance is limited by molecular scattering.

---

* Inside of 40° the measured response is limited by the baffle itself, and for this particular test the measurements were not carried beyond 70°.
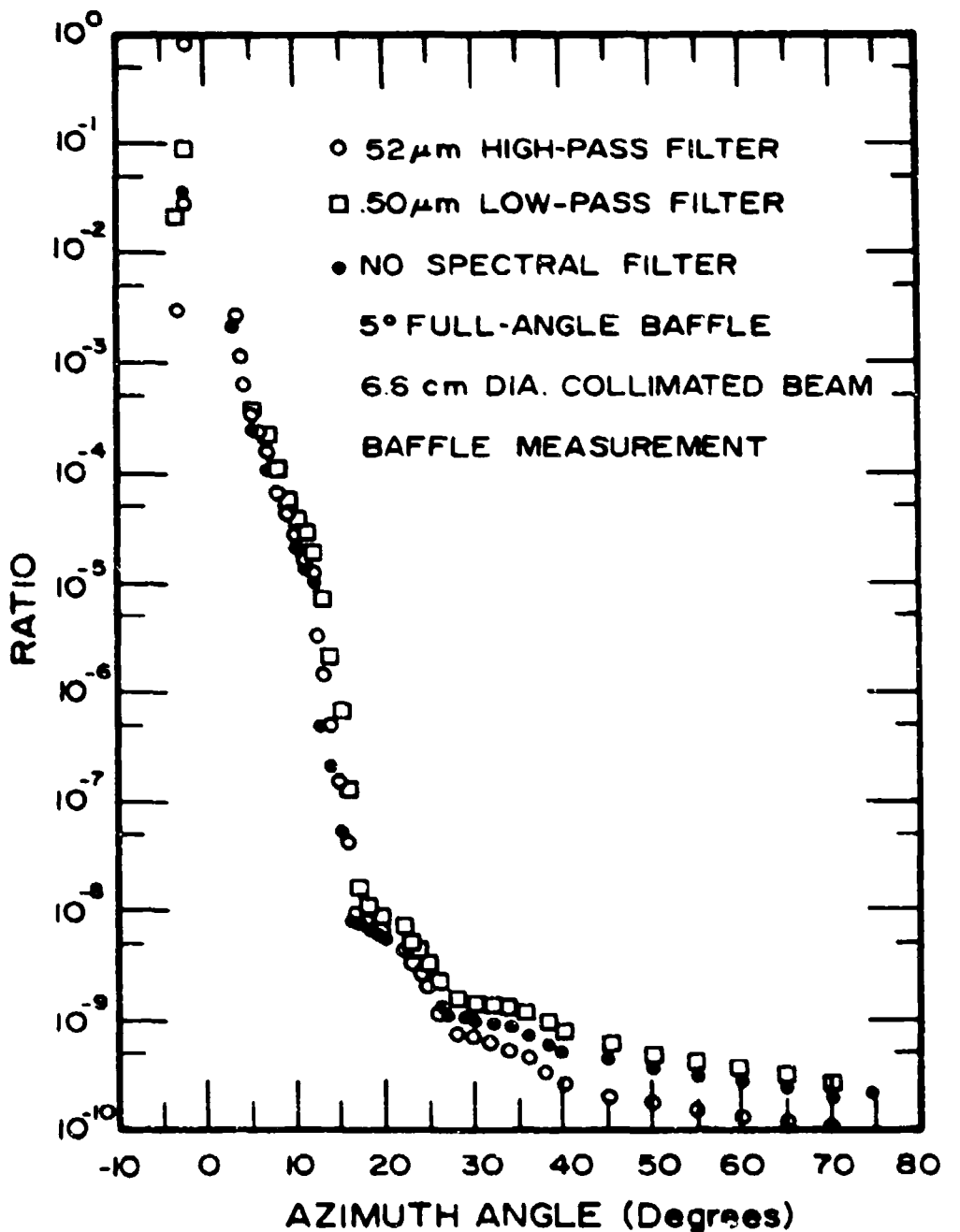
Figure 21. Measured ratios of scattered to on-axis power for the wavelength dependency test.

Experimental Determination of the Background Power Level
Produced by Surface Scattering

Off-axis rejection measurements can be limited because they are made in surroundings where the walls reflect radiation scattered from the front of the baffle back into the baffle entrance, thereby increasing the "signal" output. The baffle performance appears to be limited at a level higher than that actually due to the baffle construction. It is difficult to separate these chamber effects from the actual baffle performance in a conventional baffle measurement configuration. Therefore, special techniques were used to determine the power level of the radiation scattered off of the specular chamber walls.

Description of the measurement technique

A dummy baffle was inserted into the collimated beam in a standard measuring configuration and a second baffle, attached to the photomultiplier assembly but located out of the collimated beam, was used to measure the energy reflected off the walls, as shown in Figure 22. The baffle was used in this manner to determine the power scattered off the walls without the baffle performance entering directly into the measurement.

Both the scattering baffle and the sensing baffle were attached to the rotating instrument platform so that the angular variations could be measured. The scattering baffle was located 10 cm above the platform aimed downward at 3° below horizontal and the sensing baffle was located 10 cm below the platform aimed upward at 3° above horizontal so that any near specular reflections were received by the sensor.

This technique measured only the primary scattered light off the walls, i.e., the light scattered from the baffle outer surfaces into the measuring baffle after only one reflection off the wall. It was anticipated that the primary limitation of the practical implementation would be the diffuse component present in the bidirectional reflectance-distribution function. The ray traces had
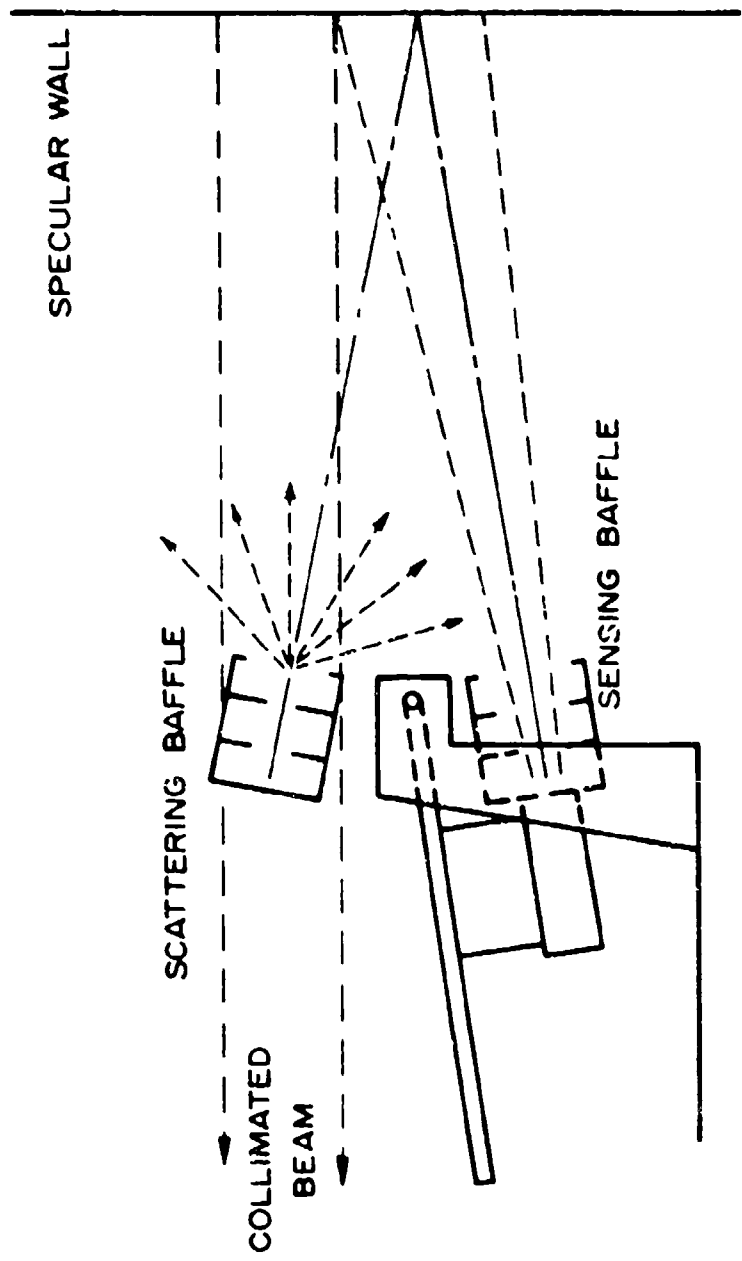
Figure 22. Mechanical configuration of scattering baffle/sensing baffle measurement.

Indicated that an absorptive and specular material with no diffuse component would successfully direct the scattered rays away from the baffle entrance.

Two different materials were used for the front surface of the scattering baffle so that the power scattered off the baffle to be reflected off the walls could be increased above the usual level. Comparing the change in the measured background power with the change in reflectance of the baffle covering provides an indication if the chamber is also being significantly limited by another mechanism in addition to surface scattering.

A standard baffle measurement was performed and then repeated with the front surface material replaced by white cardboard which has a much higher reflectance. This allowed determination of the comparative magnitudes of the background power due to surface scattering and the overall chamber background level from an actual baffle measurement.

Measured results

Scattering baffle/sensing baffle configuration

The results of the scattering baffle/sensing baffle experiment are shown in Figure 23. The measurement made with the standard black flock covering on the front surface is shown by the open circles. A corresponding baffle measurement is shown for comparison. The measurement was close to the signal-to-noise limit of the equipment when the black flock was used and thus was not carried beyond 40°. The surface scattered background signal is more than an order of magnitude lower than the corresponding baffle measurement data. This indicates that the baffle measurement is limited by atmospheric scattering and not surface scattering.

Measurements were also made with white cardboard replacing the black flock typically used over the baffle outer surface. These results are shown by the solid dots in Figure 23. The diffuse reflectance of the white cardboard was measured in a separate test using flat samples to be 176 times larger than that of the black flock. This number cannot be used directly as a measure of the difference in reflected power from the two baffles, however, as the white cardboard only covered the outside front of the baffle. The inner baffle blades
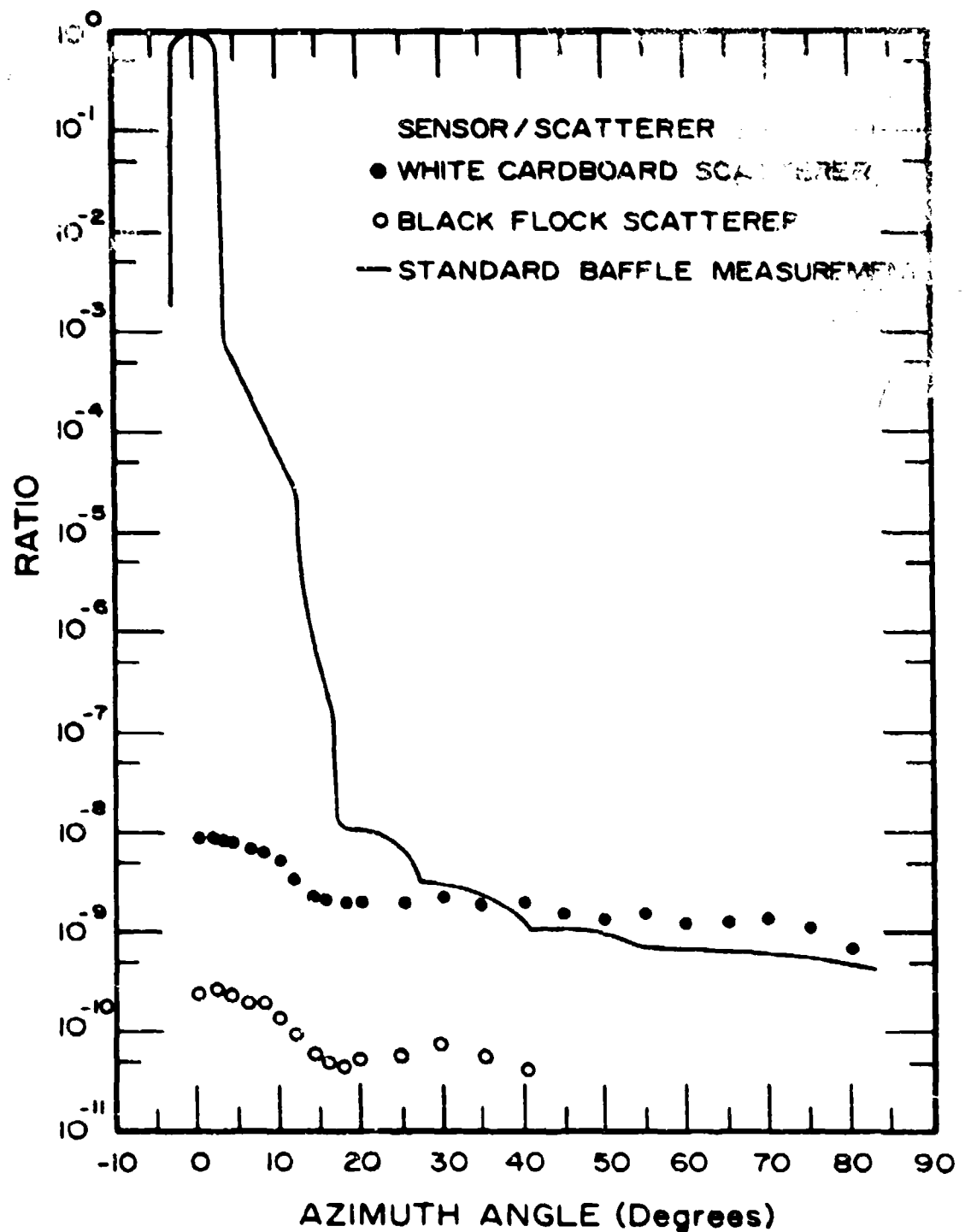
Figure 23. Measurements made using the scattering baffle sensing baffle configuration compared with a standard baffle measurement.

are visible from the front aperture of the baffle and although they are painted black they still contribute to the reflected power. The effective total reflectance for the baffle differs by only a factor of 37.5 when the relative areas and reflectances of the black flock/white cardboard region and the black painted regions are considered.

The white cardboard covered scattering baffle produced a scattered signal which averaged 39.5 times higher than that of the black flock covered baffle. This increase agrees very well with the calculated difference in effective reflectances of the two situations. This indicates that the surface scattering had been isolated from atmospheric scattering effects as desired. These measurements indicate that the background power at 40° due to surface scattering for a normal measurement is about 4×10^{-11} of the incident on-axis power.

Baffle measurement with increased reflectance.

The results from the baffle measurement configuration are shown in Figure 24, where the standard measurement is shown by the solid dots and the measurement with the white cardboard over the baffle face is shown by the open circles. The standard black flock baffle response beyond 26° when the chamber effects become apparent shows the angular shape characteristic of Rayleigh scattering. When the white cardboard was used the response became flat and departed from the Rayleigh shape. Thus, increasing the surface reflectance of the baffle face caused a transition from a measurement limited by Rayleigh scattering to one limited by surface effects. The angular response of the surface scattered radiation is expected to be very close to flat for angles greater than the baffle critical angle because of the cylindrical chamber shape. That there is not an increase of a factor of near 40 as was evident from the scatterer/sensor measurements is a further indication that the original baffle measurement was not limited by surface scattering effects. This baffle measurement with increased reflectance indicates that the background power due to surface scattering is in the range of about 4 to 9×10^{-11} of the incident on-axis power.
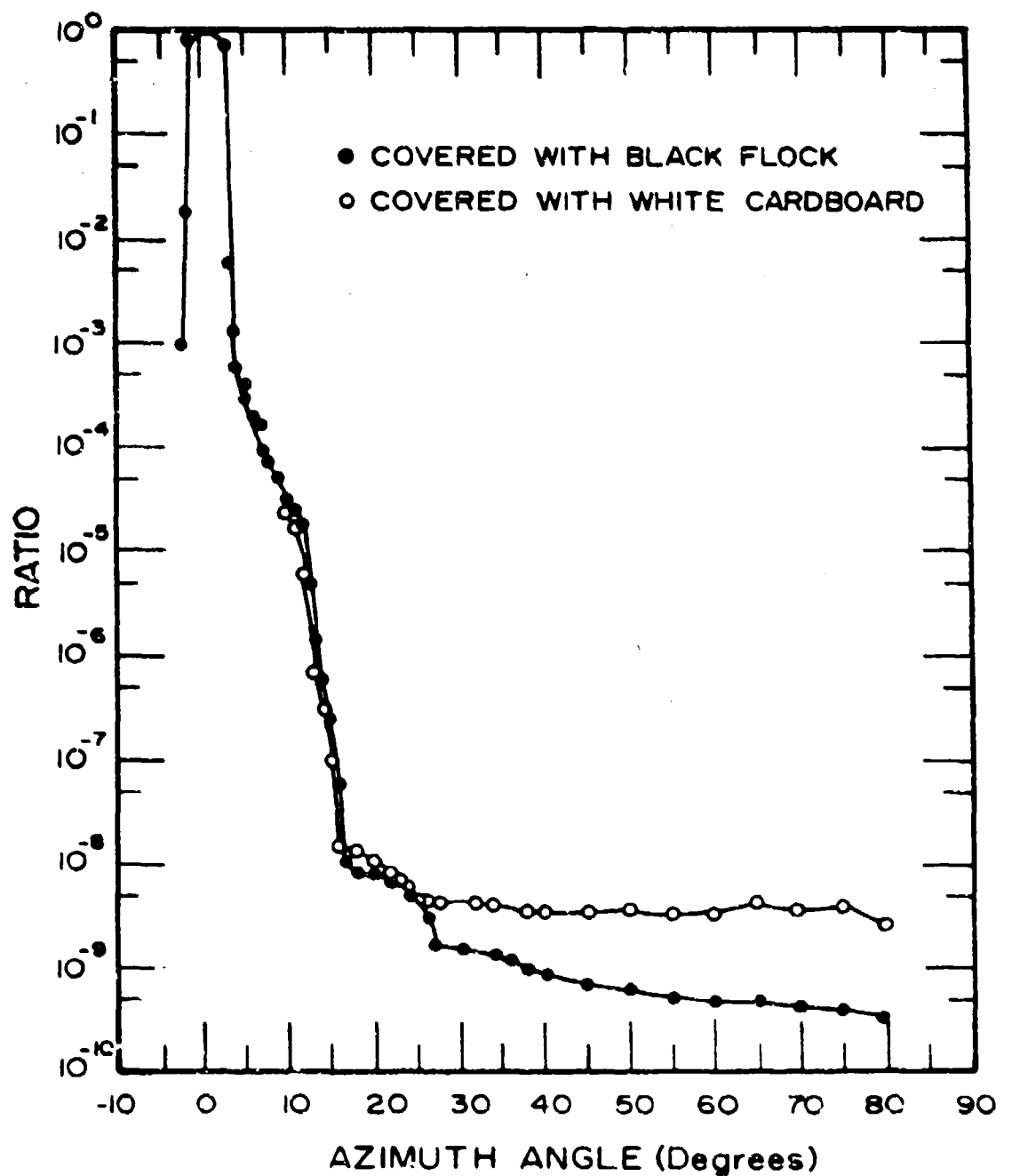
Figure 24. Baffle measurement with standard conditions and with Increased front surface reflectance.

It is interesting to note that the blocked beam tests made in conjunction with the atmospheric scattering measurements indicated that the surface scattering background would be in the range of 2 to 9 x 10^{-11} of the incident on-axis power.

Conclusion to measurements.

The above results are dependent upon the field-of-view characteristics of the measuring instrument and are for a 10.2 cm diameter collimated beam. The background levels will be higher for a wider field of view and will be smaller if the collimated beam diameter is reduced. Repeatability measurements indicate that the relative accuracy between any two test points measured during the same sequence is better than $\pm$ 10 percent. Measurement accuracy from one test to another should be within $\pm$ 20 percent. The background in the specular chamber due to atmospheric scattering is about one order of magnitude higher than that from surface scattering for a baffle measurement.

It is tempting to compare the above measured background levels of about 4 to 9 x 10^{-11} from surface scattering with those predicted from the GUERAP program. This comparison has little meaning, however, because the baffle model used in the computer program was made larger and much simpler than the real case because of the inefficient nature of the Monte Carlo technique. The computer models were used to compare different enclosures which it was not feasible to construct and measure. To model the actual baffle, the nonuniformity of source areance, etc., for the actual measurement conditions would have been very costly and beyond the funds available for this project.

Extension of Baffle Measurements

A baffle measurement can often be extended below the chamber background level by a two step process, provided that the optical field of view of the sensor

behind the baffle can be changed. This was accomplished with the baffle/sensor system used in this project, shown schematically in Figure 25.[*] A 0.5^O safety margin was included in this baffle design so that none of the knife edges are within the standard 2.5^O optical fov. The field of view can be widened to include these knife edges by increasing the field stop diameter. This degrades the off-axis rejection of the baffle, raises the response level at the various breakpoints and increases the separation between these breakpoints and the chamber ambient level.

The optical fov of the sensor was expanded to 7.5^O. The result of this measurement is compared with a standard measurement made with a 2.5^O optical fov in Figure 26. (Both of these measurements were made with a 6.6 cm diameter collimating beam.) The breakpoint at 40° off axis due to the primary knife edge moving out of direct illumination now occurs more than two orders of magnitude above its previous level. The effect of this knife edge is now more apparent because the breakpoint has been raised above the chamber background level.

The full extent of the falloff at 40° is still not known because once again the base level is determined by Rayleigh scattering and not the actual baffle performance. The shape of the two measurement curves beyond 40° is very similar although the level of the 7.5^O fov curve is higher because of the increased acceptance angle for Rayleigh scattering. This measurement indicates that the baffle response falls at least by a factor of 40 at the 40° critical angle, whereas this effect was masked by the background in the previous measurements. This result is combined with the 2.5^O fov measurement to produce the curve shown in Figure 27. We state with confidence that this baffle when used in a space environment will demonstrate an off-axis rejection exceeding eleven orders of magnitude at 40°.

---

[*] It is apparent from Figure 25 that major changes in the baffle response should be evident at off-axis angles of 12.7^O, 16°, 26°, and 40° in addition to the basic fov angle of 2.5^O. These breakpoints can be identified in many of the baffle measurements presented.

76
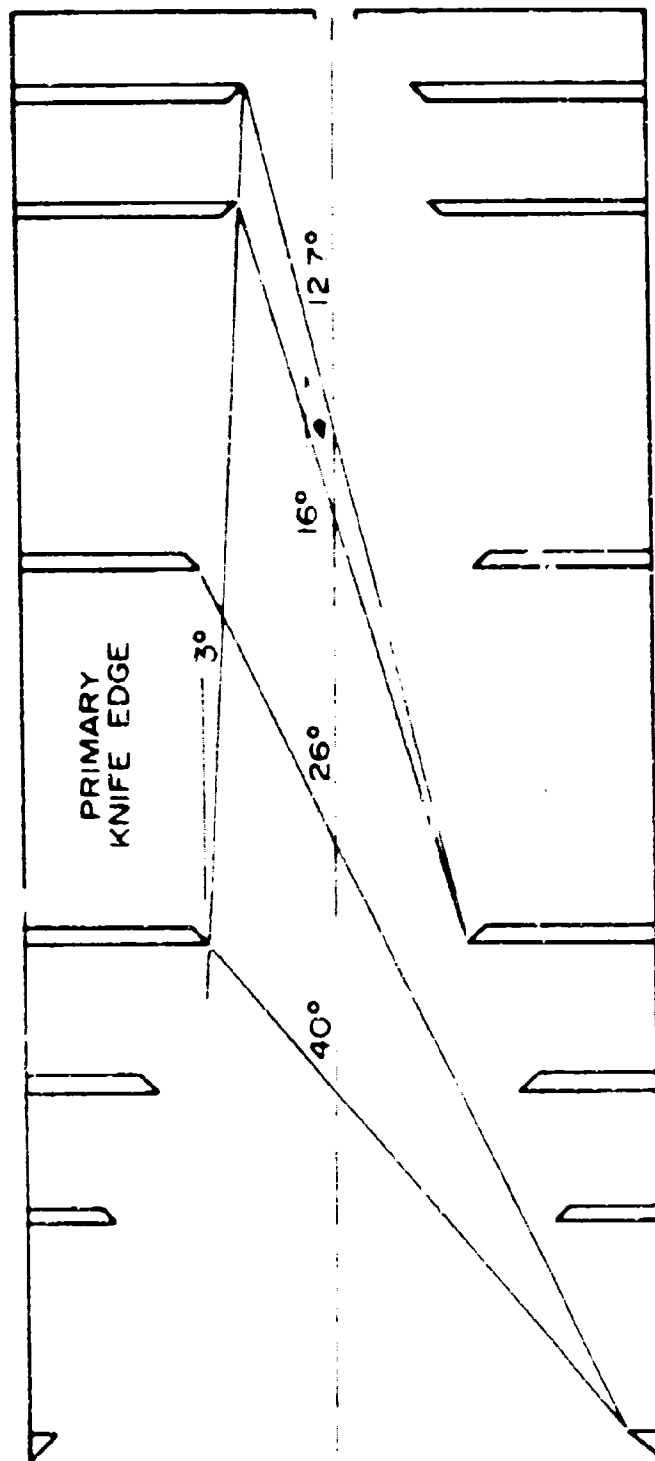
Figure 25. Schematic diagram of NR-4 baffle.
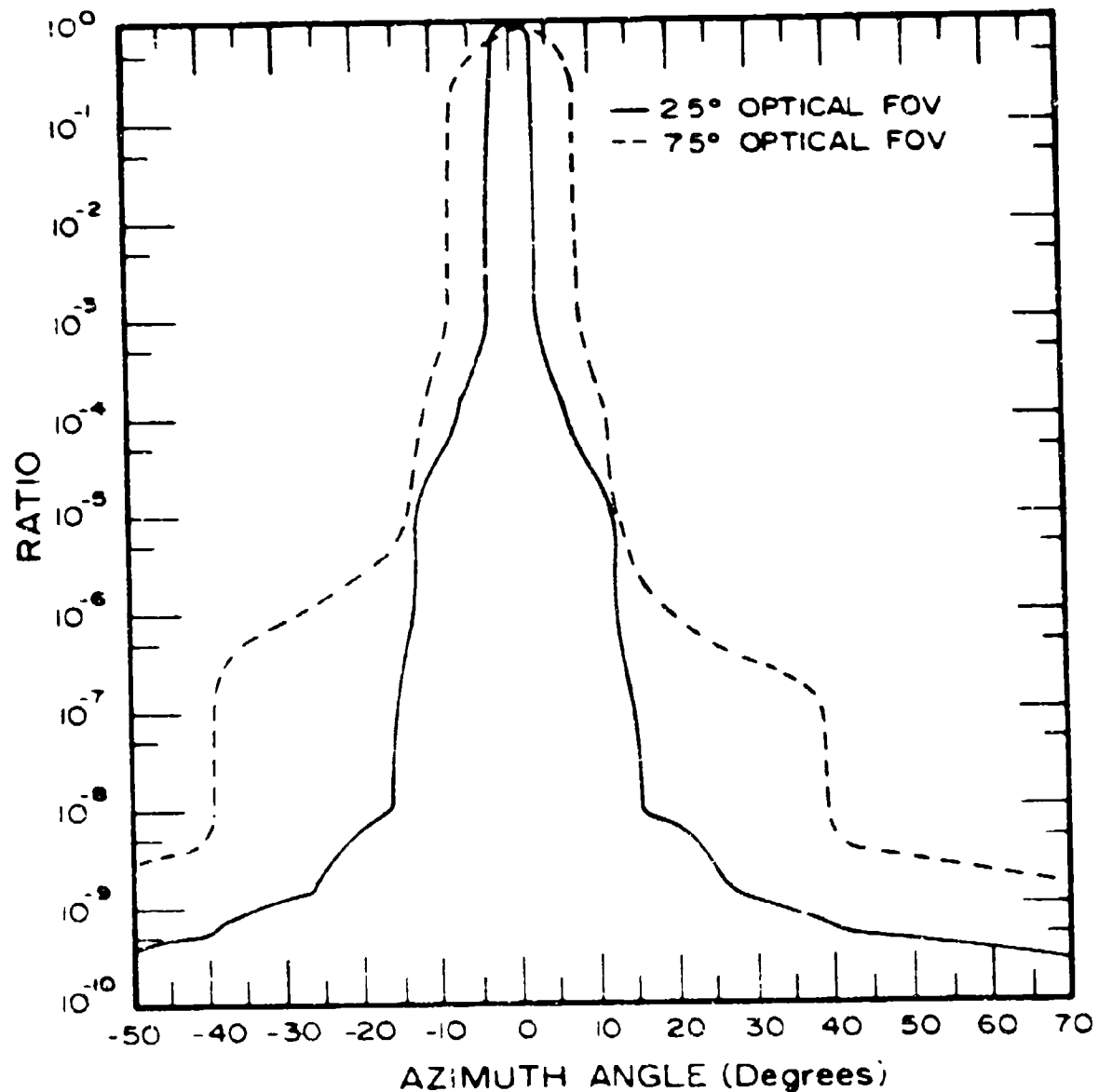
Figure 21. NR-1 baffle response as measured with 2.5° and 7.5° optical fields of view.
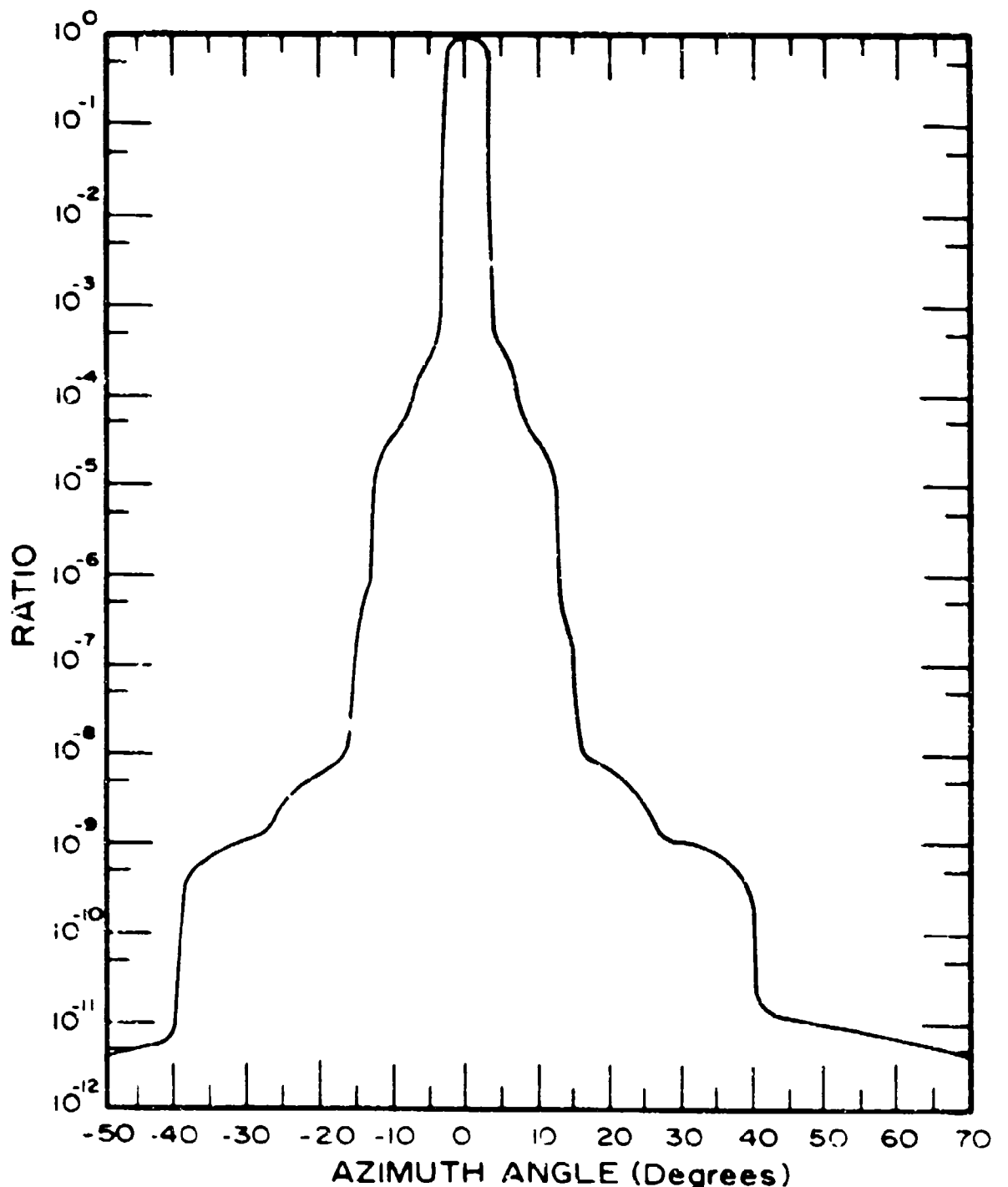
Figure 27. Predicted NR-1 baffle response for a space environment, extended

CONCLUSIONS

A special chamber for measuring the off-axis response of high-rejection optical baffling systems was designed and constructed. The background power level due to atmospheric scattering was reduced by using high efficiency particulate filters to remove the atmospheric aerosols and produce a clean room environment. The effects of surface scattering were reduced by using specular surfaces in a modified cylindrical shape to direct the scattered radiation away from the baffle entrance.

A theoretical evaluation of this chamber was performed by using two computer programs to separately model the atmospheric and surface scattering effects. This analysis indicated that removing the atmospheric aerosols would reduce the background power level by about one order of magnitude at 40°. The reduction is less at larger angles because of the steeper slope of the angular distribution for the aerosol scattering case as compared with the molecular scattering case.

The theoretical analysis of the surface scattering indicated that the modified cylindrical shape using specular surfaces provided a significant reduction in surface scattered power over a comparable square chamber with diffuse surfaces. The response predicted for a representative baffle with 2.5, 12.7 and 40° critical angles shows an improvement of a factor of 80 by using the specular walls, even though the absorption component of the bidirectional reflectance-distribution function for the two surfaces is nearly identical. The computer program indicated that the vertical extent of the special chamber was sufficiently large that the diffuse floor and ceiling did not degrade the chamber performance for most sunshade baffle measurements.

The specular chamber was also evaluated experimentally by a set of measurements designed to separate the atmospheric and the surface scattering effects. The measurements show excellent agreement with the predicted Rayleigh scattering levels. Also, the tests verify by the shape of the angular response and by the wavelength dependency that the atmospheric scattering is

due to Rayleigh (molecular) scattering; the air filtering process has effectively eliminated the aerosol scattering contributions to the background power. The background power at 40° off axis from a 10.2 cm diameter collimated beam into a baffle with 2.5, 12.7 and 40° critical angles is 1×10^{-9} of the on-axis incident power. This level drops to about 3.3×10^{-10} at 85°.

The background power from surface scattering effects is about 4×10^{-11} of the on-axis incident power. Thus, the molecular scattering dominates the surface scattering by a factor of about 25 for the particular baffle tested. The importance of using a low reflectance material to cover the outer surfaces of the baffle under test was demonstrated.

The chamber model used for the surface scattering predictions was not sufficiently refined; therefore, the measured levels did not agree well with those predicted. However, this program is very useful for comparing the effects of different materials and different shapes.

The background power level can be decreased by reducing the diameter of the collimated beam to just that needed to overfill the baffle entrance aperture. Direct measurements were made down to 5×10^{-10} of the on-axis incident power at 40° and down to 1.7×10^{-10} at 80° off axis. A two step process was used to measure a baffle response down to less than 1×10^{-11} of the on-axis incident power at 40° off axis. The background power level in the chamber could be reduced to the limit imposed by the surface scattering by evacuating the chamber down to a pressure of about 30 torr.

BIBLIOGRAPHY

Agnew, J.T., and R.B. McQuistan, 1953. Experiments Concerning Infrared Diffuse Reflectance Standards in the Range 0.8 to 20 Microns, Journal of the Optical Society of America 43:999-1007.

Aughey, W.H. and F.J. Baum, 1954. Angular-Dependence Light-Scattering— a High-Resolution Recording Instrument for the Angular Range 0.05-140°, Journal of the Optical Society of America 44:833-837.

Beckmann, Peter and Andre Spizzichino, (Eds.) 1963. The Scattering of Electro Magnetic Waves from Rough Surfaces, Pergamon Press, Inc., New York, 503 p.

Bennet, H.E. and J.O. Porteus, 1961. Relation Between Surface Roughness and Specular Reflectance at Normal Incidence. Journal of the Optical Society of America 51:123-129.

Blazey, R., 1967. Light Scattering by Laser Mirrors, Applied Optics, 6:831-836.

Boksenberg, A., F.W. Bullock, M.J. Esten, D.R. Flower, and G.C. Green, 1970. TD-1 Baffle System, Interim Report on S59, New Industrial Concepts Limited, London, 17 p.

Boksenberg, A., F.W. Bullock, M.J. Esten, D.R. Flower, G.C. Green, and J.W. Wybourn, 1971. TD-1 Baffle System, Interim Report on S2/68, New Industrial Concepts Limited, London, 14 p.

Bullrich, Kurt, 1964. Scattered Radiation in the Atmosphere and the Natural Aerosol. H.E. Landsberg and J. Van Mieghem, (Eds.), Advances in Geophysics, Vol. 10, Academic Press, New York, pp. 99-260.

Chou, T.S., 1972. GUERAP, (General Unwanted Energy Rejection Analysis Program), User's Manual, Honeywell Report No. UERTD TM 3366-008, Honeywell Aerospace Division, St. Petersburg, Florida, 110 p.

Chou, Tien, S., 1974. A Monte Carlo Approach to Optical Analysis, Optical Engineering 13:299-302.

Davies, H., 1954. The Reflection of Electromagnetic Waves from a Rough Surface, Institution of Electrical Engineers, Proceedings 101:209-214.

Fowles, Grant R., 1968. Introduction to Modern Optics, Holt, Rinehart and Winston, Inc., New York, 304 p.

Heinisch, R.P., 1971. Infrared Mirror-Scatter Measurements, Journal of the Optical Society of America 61:1225-1229.

Heinisch, R.P., and T.S. Chou, 1971. Numerical Experiments in Modeling Diffraction Phenomena, Applied Optics 10:2248-2251.

Heinisch, R.P., and C.L. Jolliffe, 1971. Light Baffle Attenuation Measurements in the Visible, Applied Optics 10:2016-2020.

Hostetter, G.R., D.L. Patz, H.A. Hill, and C.A. Zanoni, 1968. Measurements of Scattered Light from Mirrors and Lenses, Applied Optics 7:1383-1385.

Howell, John R., 1968. Application of Monte Carlo to Heat Transfer Problems, Advances in Heat Transfer, Vol. 5, Thomas F. Irvine, Jr., and James P. Hartnett, (Eds.), Academic Press, New York, p. 1-54.

Jones, R. Clark, 1963. Terminology in Photometry and Radiometry , Journal of the Optical Society of America, 53:1314.

Kasten, F., and E. Raschke, 1974. Reflection and Transmission Terminology by Analogy with Scattering, Applied Optics 13:460-464.

Kerker, Milton, 1969. The Scattering of Light and Other Electro-magnetic Radiation, Academic Press, Inc., New York, 666 p.

Klein, Miles V., 1970. Optics, John Wiley and Sons, Inc., New York, 647 p.

Kondratyev, K. Ya, 1969. Radiation in the Atmosphere, Academic Press, New York.

Leinert, C. and D. Klüpelberg, 1974. Stray Light Suppression in Optical Space Experiments, Applied Optics 13:556-564.

Look, D.C., Jr., 1965. Diffuse Reflection from a Plane Surface, Journal of the Optical Society of America 55:1628-1632.

MacQueen, R.M., 1968. A Balloon-Borne Infrared Coronagraph, Applied Optics 7:1149-1154.

Marette, G. and J.C. Gérard, 1976. Rocket-Borne Baffled Photometer: Design and Calibration", Applied Optics 15:437-439.

McClatchey, R.A., R.W. Fenn, J.E.A. Selby, F.E. Volz, J.S. Garing, 1972. Optical Properties of the Atmosphere (Third Edition), Air Force Cambridge Research Laboratories, AFCRL-72-0497, Bedford, Mass., 108 p.

Munis, R. H. and M. W. Finkel, 1968. Goniometric Measurements of Infrared Transmitting Materials, Applied Optics 7:2001-2004.

Newkirk, G. A. and J. D. Bohlin, 1963. Reduction of Scattered Light in the Coronagraph, Applied Optics 2:131-140.

Nicodemus, Fred E. and George J. Zissis, 1962. Report of BAMIRAC--Methods of Radiometric Calibration, The University of Michigan, Infrared Laboratory, IST, Ann Arbor, Michigan, ARPA Contract No. SD-91, Report No. 4613-20-R.

Nicodemus, F. E., 1970. Reflectance Nomenclature and Directional Reflectance and Emissivity, Applied Optics 9:1474-1475.

Nicodemus, F. E., 1973. Comments on: Chinese Restaurant Nomenclature for Radiometry , Applied Optics 12:904-905.

Orme, Gordon Reed, 1972. Measurement of Small-Angle Scatter from Smooth Surfaces, Ph. D. Dissertation, University of Arizona.

Penndorf, R., 1956. New Tables on Mie Scattering Functions for Spherical Particles, Part 6, AFCRC-TR-56-204(6), Geophysics Research Directorate, Air Force Cambridge Research Center, Air Research and Development Command.

Penndorf, Rudolf, 1957. Tables of the Refractive Index for Standard Air and the Rayleigh Scattering Coefficient for the Spectral Region Between 0. 2 and 20.0µ and Their Application to Atmospheric Optics, Journal of the Optical Society of America 47:176-182.

Schaeffer, R. C. and W. G. Fastie, 1972. Tilting-Filter Measurements in Dayglow Rocket Photometry, Applied Optics 11:2289-2293.

Schenkel, F. W., 1973. An Automatic Self Deployable High Attenuation Light Shade for Spaceborne Sensors, Journal of the British Interplanetary Society 26:589-596.

Shamsundar, N., E. M. Sparrow, and R. P. Heinisch, 1973. Monte Carlo Radiation Solutions—Effect of Energy Partitioning and Number of Rays, International Journal of Heat and Mass Transfer 16:690-694.

Smith, Warren J., 1966. Modern Optical Engineering, McGraw-Hill Book Company, New York, 476 p.

Spiro, Irving J., 1974. Radiometry and Photometry, Optical Engineering 13:G164-G165

84

Torrance, K. E., 1966. Off-Specular Peaks and Angular Distribution of Reflected Thermal Radiation, Ph. D. Dissertation, University of Minnesota, 157 p.

Wilson, William R. and Jack F. Wade, 1974. Compilation of Known Information on Martin Morietta Black Surface, Martin Marietta Aerospace, Denver Division, Denver, Colorado, 7 p.

Wyatt, Clair L., 1976. Theory and Methods of Radiometric Calibration, Electro-Dynamics Laboratory, Utah State University, Logan, Utah, 136 p.

Yap, B. K., 1974. Rejection of Out-of-Field Optical Sources, Optical Engineering 13:343-346.

APPENDIXES

Appendix A

Infrared Measurement

The specular chamber has been used to measure the off-axis response of a set of liquid-nitrogen-cooled short wave infrared radiometers with wavelength responses from 2.0 to 5.4 µm. The tungsten-halogen lamp was found to function effectively as a source out to at least 5.4 µm. The quartz envelope will not transmit well beyond about 4.3 µm, but the envelope itself becomes sufficiently hot to act as a blackbody radiator in the wavelength regions of interest. This experimental setup has also been used to measure the co-alignment between different channels of cooled instruments.

The measured response for NR-4-7, Channel 2, at 2.0 µm is shown in Figure A-1. The small "Wings" about three orders down at about 8° off axis have been identified as the scattering off the edges of the sapphire substrate used to mount the detector chip. The baffle is the same configuration as that used with the photomultiplier sensor for all of the measurements discussed in this report. The response is now being limited by the warm vacuum window as previously shown in Figure 3.
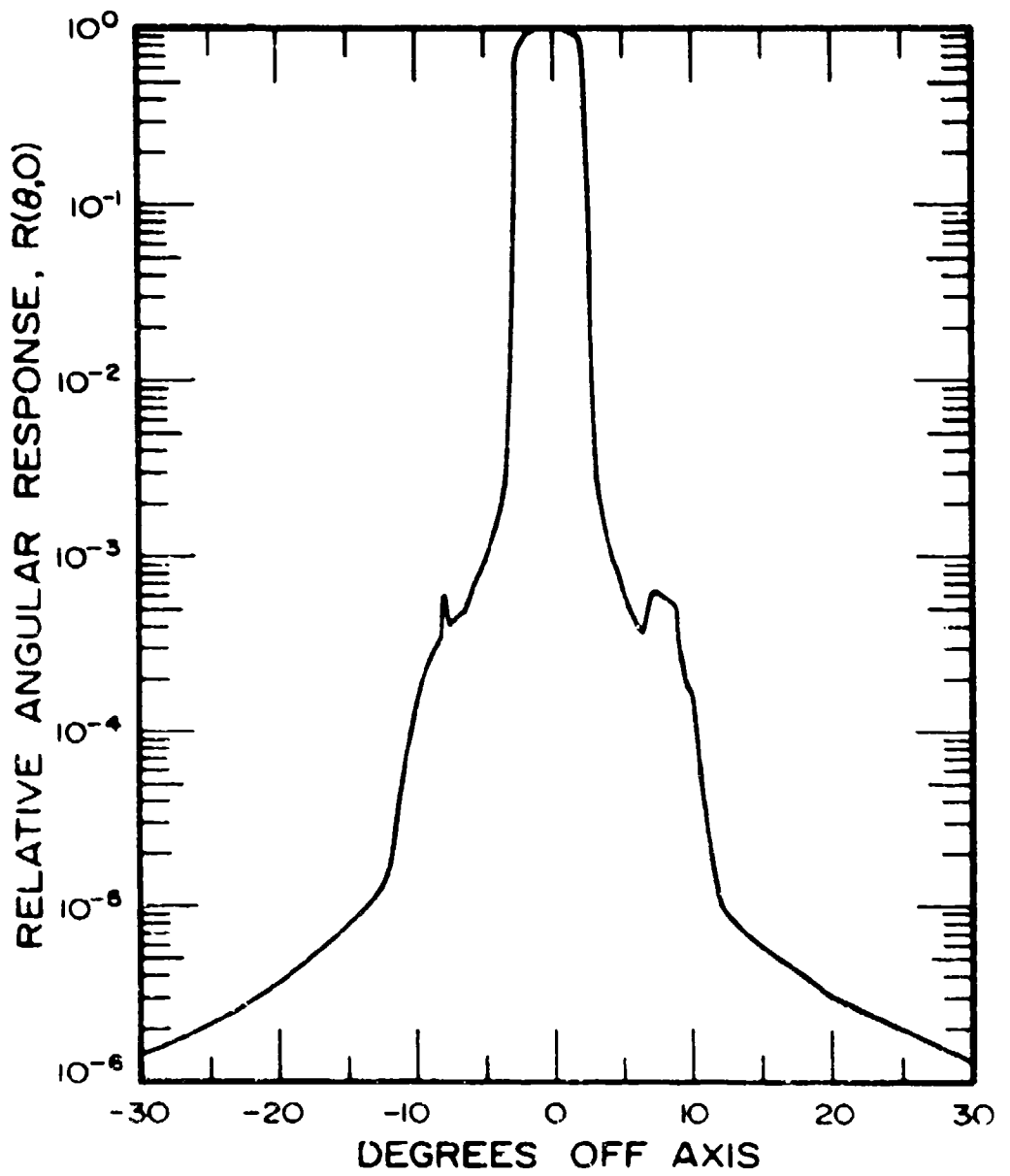
Figure A-1. Measured response of NR-4-7, Channel 2 at 2.0 μm.

Appendix B

Atmospheric Scattering Program

The basic approach taken to calculate the influence of atmospheric scattering on the measurement of the off-axis rejection of a baffle was discussed previously. A short description of some of the functional aspects of the computer program SCAT is now given to supplement the comment cards included in the program. A listing of SCAT and a sample page of output are then given.

The geometry involved was shown previously in Figures 9, 10 and 11. The system Z axis is chosen to coincide with the axis of the collimated beam with the light traveling in the negative Z direction. The origin of the system coordinates is taken to be the center of rotation of the measuring baffle. The extent of the collimated beam is defined by a circular cylinder whose equation is

$$X^2 + Y^2 = (RCB)^2 \quad , \qquad \text{inches}^2 \qquad (B\text{-}1)$$

where RCB is the radius of the collimated beam in inches.

The equation of the cone representing the field of view of the optical system behind the baffle, with the cone axis lying along the Z axis and the lens aperture placed at the origin, is

$$X^2 + Y^2 = \frac{(Z + 5.153)^2}{524.58} \quad , \qquad \text{in}^2 \qquad (B\text{-}2)$$

for a 2.5° half angle field of view. A coordinate transformation is made by translating the fov cone coordinates by a factor S(the separation between the lens and the center of rotation) along the Z axis and by rotating these coordinates by an angle θ (the off-axis measurement angle) about the Y axis. This locates the fov cone in its proper position with respect to the collimated beam.

The four intersections of the cone and the cylinder in the Y = 0 plane are next determined. The maximum and minimum Z values from these intersections

are denoted by ZMAX and ZMIN. The control volume is defined to be the section of the collimated beam lying between ZMAX and ZMIN. This control volume is determined for each off-axis angle so that it will be the minimum size necessary to include the desired scattering volume. This helps to make the Monte Carlo technique more efficient by eliminating many random points which are not necessary to define the scattering volume.

A loop is entered which generates random points with uniform probability density in the control volume by using a uniform random number generator. Each point is tested to establish if it lies within the fov cone and is thus a legitimate element of the scattering volume. The equation of the cone surface can be written in the form

$$f(x, y, z) = 0 \quad . \tag{B-3}$$

The value of the function $f(x, y, z)$ is negative for any (x, y, z) within the cone volume and positive for any (x, y, z) outside of the cone because of the quadratic nature of the equation. This provides a simple test for determining if a particular point of the collimated beam also lies within the fov cone. If the random point does not lie within the fov cone the program returns to the start of the loop and another random point is generated.

For those points which do lie within the cone, the effective areance at the point is determined using Equation (33) once the radius within the collimated beam is determined. A second random point is next generated with uniform density in the aperture of the lens and the distance between the two random points is calculated. The acute angle between the line connecting the two points and the Z axis is calculated so that the scattering phase function may be evaluated. An additional test is made to verify that the angle between the scattered ray and the baffle normal does not exceed the optical fov half angle.

Equation (24) for the ratio of flux scattered at an angle θ to the on-axis incident flux can be rewritten in terms of the computer variables as

$$\text{RATIO} = \sigma \sum_{N_T} \frac{\text{PCS} \cdot \text{E}}{\text{SS2}} \quad , \tag{B-4}$$

where σ is the scattering cross section, PCS is the scattering phase function, E is the relative arcance at the scattering element and SS2 is the square of the distance between the scattering element and the collection point. The quantity within the summation is tallied as PT, the counter CN of sample points included within the scattering volume is incremented, and the program loop is continued. Additional random scattering points are generated, evaluated, and tabulated until the limit set for the number of random test points is reached at which time the loop is exited.

A small section is inserted into the program at this point to separate the tabulations into two halves that can be compared as a means of indicating the accuracy of the Monte Carlo approximation. The remainder of the program calculates

$$\text{RATIO} = \frac{N \cdot \sigma \cdot \text{VOL} \cdot \text{PT}}{\text{LEMIT}} \quad , \tag{B-5}$$

derived from Equations (B-4) and (30), where N is the number density of scatterers, LEMIT is the total number of scattering points generated, and VOL is the scattering volume as determined from

$$\text{VOL} = \frac{\text{VC} \cdot \text{N}}{\text{LEMIT}} \quad , \tag{B-6}$$

as part of the Monte Carlo calculation. VC is the control volume.

The above procedure is followed for scattering column calculations. An additional constraint to the scattering volume must be considered for a baffle measurement calculation. This constraint is imposed by the front plate of the baffle which blocks part of the collimated beam from the fov cone as shown previously in Figure 9. The constraint surface appears as an elliptical

cylinder whose axis is parallel to the collimated beam. The major diameter along the Y axis is the 1.833 inch diameter of the baffle entrance aperture and the minor diameter along the X axis is 1.833 cos θ inches. The equation of this elliptical cylinder is

$$\left(\frac{X}{Cos\ \theta}\right)^2 + Y^2 = .9166^2 \quad . \quad in^2 \qquad (B-6)$$

An additional test is inserted in the pro ~ am for the case of a baffle measurement to verify that the potential scattering point is indeed illuminated and is not in the shadow of the front plate.

The formula used to calculate the angular Rayleigh scattering cross section $\sigma_{R\theta}$ was derived from one given by Penndorf, (1957), by applying the Lorentz-Lorentz law to account for nonstandard conditions,

$$\sigma_{R\theta} = \frac{5.325(n^2-1)^2(1 + 0.932\ Cos^2\theta)}{\lambda^4\ N^2} \qquad (B-7)$$

where n is the index of refraction and N is the number density of molecules, both for air at the temperature and pressure of the measurement. The above number was modified to allow english units in the program by including a factor to convert from centimeters to inches.

The cross section and scattering phase function used for aerosol scattering were those given by McClatchey et al., (1972). A listing of the program SCAT as configured for Rayleigh scattering is now given followed by a sample page of output for a Rayleigh scattering column calculation.

92

```
         H6700/P7700   F C R T R A N   C C M P I L A T I C N   M A R K   2.7.48C

 $SET ECB
 FILE 5=FILES
 C PROGRAM NAME = SCAT
 C PURPOSE
 C
 C    THIS PROGRAM USES A MCNTE CARLO TECHNIQUE TC CALCULATE THE RATIO CF
 C    PCWER SCATTERED BY RAYLEIGH SCATTERING FRCM A VOLUME CF AIR TC A
 C    SPECIFIC COLLECTOR SURFACE TO THE POWER INCIDENT ON THE COLLECTOR
 C    SURFACE IF THE SURFACE WERE ILLUMINATED NORMALLY BY THE COLLIMATED
 C    BEAM WHICH PRODUCES THE SCATTERED ENERGY.
 C
 C INPUT
 C
 C    A.   FIRST RECORD (3F10.3,A4)
 C         1.  RCB - RADIUS OF COLLIMATED BEAM.
 C         2.  A2 - DEFINED FROM X**2+Y**2+Z**2=A2.  RELATES TO THE HALF
 C             ANGLE FOV OF THE COLLECTOR WHICH IS 2.5 DEGREES.
 C         3.  S - THE DISTANCE BETWEEN THE CENTER OF ROTATION AND THE
 C             COLLECTOR SURFACE.
 C         4.  WHAT - BAFF - TEST CASE IS FOR A BAFFLE MEASUREMENT.
 C                    SCAT - TEST CASE IS FOR A SCATTER MEASUREMENT.
 C             START WHAT VALUE IN COLUMN 31.
 C    B.   SECCND RECORD (I10,6E10.3)
 C         1.  LIMIT - THE NUMBER OF POTENTIAL SCATTERING ELEMENTS TC BE
 C                     GENERATED WITH A UNIFORM PROBABILITY DENSITY WITHIN
 C                     THE CONTRL VOLUME, VC.
 C         2.  SEED - THE SEED NUMBER FOR THE RANDOM NUMBER GENERATOR.
 C         3.  E1,E2,E3,E4,E5 - THE COEFFICIENTS OF THE IRRADIANCE FUNCTION
 C                     FOR THE COLLIMATED BEAM -
 C                     E(R)=E1 + E2*R + E3*R**2 + E4*R**3 + E5*R**4
 C    C.   THIRD RECORD (I10)
 C         JJ - NUMBER OF DIFFERENT VALUES OF THETA TO BE RUN
 C         (JJ.LE.100).
 C    D.   FOURTH RECORD AND FOLLOWING (8F10.3)
 C         THETA(1)
 C         THETA(2)
 C         THETA(3)
 C            .
 C            .
 C            .
 C         THETA(JJ)
 C
 C OUTPUT
 C
 C    ALL CF THE INPUT PARAMETERS ARE OUTPUTTED.
 C    THE FINAL VALUE OF SEED IS ALSO GIVE SO THAT THE RUN MAY BE
 C    CONTINUED.
 C    THE OTHER OUTPUTS ARE EXPLAINED BY THE HEADINGS.
 C
 C THE SCATTERING VOLUME IS THE INTERSECTION OF A CYLINDER REPRESENTING
 C THE COLLIMATED BEAM OF LIGHT AND A CONIC REPRESENTING THE VIEWING
 C FIELD CF THE COLLECTOR.
 C
 C
 C


         DIMENSION AVER(3),A(3),PI(3),RATIO(3),THE(100),VOL(3)
```

```
      LOGICAL SCATER/.TRUE./
C
      READ(5,101) RCB,A2,S,BHAT
      READ(5,110) LIMIT,SEED,E1,E2,E3,E4,E5
      READ(5,110) JJ
      READ(5,120) (THE(I),I=1,JJ)
      IF(BHAT .EQ. 'BAFF') SCATER=.FALSE.
      WRITE(6,130) BHAT,RCB,A2,S,LIMIT

      WRITE(6,140) E1,E2,E3,E4,E5,SEED
      WRITE(6,150)
      DO 100 I=1,JJ
      THETA=THE(I)*3.1415927/180.
C
C     RESET PARAMETERS
C
      PT(1)=0.
      PT(2)=0.
      A(1)=0
      A(2)=0
C
C     DETERMINE THE INTERSECTIONS OF THE CONE AND CYLINDER IN THE
C     Y-Z PLANE.
C
      CS=COS(THETA)
      SN=SIN(THETA)
      A24=1./A2
      A=SN*SN-(CS*CS*A2I)
      SA2=(S*S.1533)*A2I
      RCS=RCB*CS
      RSN=RCB*SN
      E1=-2.*SA2*CS
      E2=-2.*RCS*SN-(2.*RSN*CS*A2I)
      C1=RCS*RCS-(RSN*RSN*A2I)-(SA2*SA2*A2)
      C2=-2.*SA2*RSN
      B=E1+E2
      C=C1+C2
      AA=1./(2.*A)
      SQR=SQRT(B*B-4.*A*C)
      Z1=(SQR-B)*AAI
      Z2=(-1.*B-SQR)*AAI
      B=B1-B2
      C=C1-C2
      SQR=SQRT(B*B-4.*A*C)
      Z3=(SQR-B)*AAI
      Z4=(-1.*B-SQR)*AAI
      ZMAX=AMAX1(Z1,Z2,Z3,Z4)
      ZMIN=AMIN1(Z1,Z2,Z3,Z4)
      ZDIF=ZMAX-ZMIN
      LEN=LIMIT/2
      VC=3.141593*RCB*RCB*ZDIF
      J=1
      ISTART=1
      ISTOP=LEN
   10 DO 90 LT=ISTART,ISTOP
C
C     GENERATE A RANDOM SCATTERING ELEMENT WITH UNIFORM PROBABILITY
C     DENSITY IN THE COLLIMATED BEAM FROM ZMAX TO ZMIN WITH ONLY
C     POSITIVE Y VALUES ALLOWED.
C
      ANGLE=3.141593*RANDOM(SEED)
```

```
      RAD=RCB*RANDOM(SEED)
      X=RAD*COS(ANGLE)
      Y=RAD*SIN(ANGLE)
      Z=(RANDOM(SEED)*ZDIF)+ZPIN
C
C     TEST RANDOM SCATTERING ELEMENT TO DETERMINE IF IT LIES WITHIN FOV
C     CONE AND HENCE WITHIN SCATTERING VOLUME.
C
      XX=-X*SN+X*CS
      ZZ=X*SN*Z*CS + S
      F=XX*XX+Y*Y-((ZZ+5.153))**2*A21
C     F IS NEGATIVE FOR POINTS WITHIN THE CONE.
      IF(F-.0001) 40,40,90
   40 IF(ISCATFR) GO TO 60
C
C     MODIFICATIONS TO SCAT TO MODEL THE CASE FOR A BAFFLE MEASUREMENT.
C
      IF(X-.0001) 50,60,60
   50 G=(X/CS)**2 + Y*Y - .0402
      IF(G-.001) 60,60,90
C
C
C     GENERATE A RANDOM POINT ON THE COLLECTOR SURFACE (APERTURE OF LENS
C
   60 ANGLE=6.283186*RANDOM(SEED)
      RAD=.225*RANDOM(SEED)
      XC=RAD*COS(ANGLE)
      YC=RAD*SIN(ANGLE)
C
C     CALCULATE THE POWER SCATTERED FROM THE RANDOM SCATTERING ELEMENT
C     TO THE RANDOM COLLECTOR POINT.
C
      SS2=(XX-XC)**2 + (Y-YC)**2 + ZZ*ZZ
      ANG=ABS(ZZ)/SQRT(SS2)
      IF(ANG-.99905) 85,65,65
   65 RR=SQRT(X*X + Y*Y)
      E=E1 + RR*(E2 + RR*(E3 + RR*(E4 + RR*E5)))
      ZET=Z*XC*SN+S*CS
      DEN=SQRT((X-XC*CS+S*SN)**2+(Y-YC)**2+ZET*ZET)
      CSS=ABS(ZET)/DEN
      FCS=1. + .932*CSS*CSS
      P=FCS*E/SS2
      PT(J)=PT(J) + P
   85 N(J)=N(J) + 1
   90 CONTINUE
      IF(J-1) 91,91,92
   91 J=2
      ISQRT=LEN+1
      ISECP=LIMIT
      GO TO 10
   92 CLEN=LEN
      CLEP=LIMIT
      DO 94 M=1,2
      IF(N(M)) 94,94,293
  293 CONTINUE
      CN=N(M)
      FPT=PT(M)
      R+110(M)=(1.51E-8)*VC*FPT/CLEN
      AVER(M)=PPT/CN
      VOL(M)=VC*CN/CLEN
   94 CONTINUE
```

```
      P(3)=N(1) + N(2)
      IF(N(3)) 99,99,295
  295 CONTINUE
      CN=FLOAT(N(3))
      PT(3)=PT(1) + PT(2)
      RATIO(3)=(1.51E-8)*VC*PT(3))/CLIM
      AVER(3)=PT(3)/CN
      VOL(3)=VC*CN/CLIP
   59 WRITE(6,160) THE(I),VC,(N(J),J=1,2),(VOL(J),J=1,2),(AVER(J),
     1 J=1,2),(RATIO(J),J=1,2),SEED,N(3),VOL(3),AVER(3),RATIO(3)
  300 CONTINUE
      WRITE(6,170) SEED
      STOP
C
C
C
  101 FORMAT(W10.6,A4)
  110 FORMAT(T10,6E10.3)
  120 FORMAT(MF10.3)
  130 FORMAT('1',10X,A6,' CALCULATION OF POWER FROM ATMOSPHERIC'
     1 ,' SCATTERING'///' RADIUS OF COLLIMATED BEAM= ',F4.2,10X,
     2 '& COEFFICIENT A2 OF CONIC EQUATION= ',1PE10.3,//
     3 ' DISTANCE FROM CENTER OF ROTATION TO COLLECTING SURFACE= ',E10.3
     4 ,//' TOTAL NUMBER OF SCATTERING ELEMENTS CONSIDERED= ',I6)
  140 FORMAT(//' IRRADIANCE DISTRIBUTION WITH RADIUS OF COLLIMATED BEAM'
     1 //10X,'E(R)= ',1PE10.3,' + ',E10.3,'*R + ',E10.3,'*R**2 +',E10.3,
     2 '*R**3 + ',E10.3,'*R**4'//' STARTING SEED= ',OPF10.0////)
  150 FORMAT(' ANGLE    CONTROL    NUMBER OF ELEMENTS    VOLUME OF THE SCA
     1TTERING',5X,'AVER. POWER SCATTERED PER        RATIO OF SCATTERING',
     2 ' POWER TO'/10X,'VOLUME',6X,'IN SCAT. REC.',15X,'REGION',17X,
     3 'SCATTERING ELEMENT',9X,'ON-AXIS INCIDENT POWER')
  160 FORMAT(//1X,F6.2,1PE11.3,5X,'(',I5,',',I5,')',3(7X,'(',E10.3,',',
     1 E10.3,')')//' SEED=',G14.4,T26,I5,T40,E10.3,T70,E10.3,T100,E10.3)
  170 FORMAT(//10X,'FINAL VALUE OF SEED=',G15.4)
C
C
 1000 FORMAT(//' Z1,Z2,Z3,Z4',4(G12.6,4X))
 1010 FORMAT(' LAST ARCCOS(COS)=',F10.3)
      END
```

SCAT CALCULATION OF POWER FROM ATMOSPHERIC SCATTERING

RADIUS OF COLLIMATED BEAM= 2.00   Z COEFFICIENT A2 OF CONIC EQUATION= 5.746E+02

DISTANCE FROM CENTER OF ROTATION TO COLLECTING SURFACE= 2.946E-01

TOTAL NUMBER OF SCATTERING ELEMENTS CONSIDERED=   5000

IRRADIANCE DISTRIBUTION WITH RADIUS OF COLLIMATED BEAM

E(R)= 9.925E-01 + -2.059E-02*R + -9.680E-02*R**2 + -5.212E-01*R**3 + 2.280E-01*R**4

STARTING SEED= 1234567.

ANGLE	CONTROL VOLUME	NUMBER OF ELEMENTS IN SCAT. REG.	VOLUME OF THE SCATTERING REGION	AVER. POWER SCATTERED PER SCATTERING ELEMENT	RATIO OF SCATTERING POWER TO ON-AXIS INCIDENT POWER
10.00 SEED=	5.102E+02 1.0010E+11	(751, 755) 1390	(1.539E+02, 1.541E+02) 1.559E+02	(1.380E-03, 1.327E-03) 1.355E-03	(3.127E-09, 3.075E-09) 3.101E-09
20.00 SEED=	2.600E+02 3.7275E+11	(745, 824) 1570	(7.100E+01, 7.992E+01) 7.555E+01	(1.106E-03, 1.387E-03) 1.380E-03	(1.735E-09, 1.605E-09) 1.579E-09
30.00 SEED=	1.552E+02 1.2430E+11	(811, 825) 1656	(5.180E+01, 5.123E+01) 5.342E+01	(1.291E-03, 1.306E-03) 1.297E-03	(1.804E-09, 1.007E-09) 1.007E-09
40.00 SEED=	1.125E+02 1.332E+11	(918, 860) 1778	(4.135E+01, 1.071E+01) 4.002E+01	(1.287E-03, 1.251E-03) 1.275E-03	(8.029E-10, 7.175E-10) 7.736E-10
50.00 SEED=	8.619E+01 5.5206E+11	(805, 945) 1930	(3.595E+01, 3.256E+01) 5.522E+01	(1.068E-03, 1.073E-03) 1.079E-03	(5.760E-10, 5.184E-10) 5.521E-10
60.00 SEED=	6.780E+01 3.3846E+11	(1086, 1068) 2156	(1.949E+01, 2.900E+01) 2.926E+01	(9.309E-04, 9.401E-04) 9.398E-04	(4.355E-10, 4.117E-10) 4.108E-10
70.00 SEED=	5.406E+01 1.9576E+11	(1216, 1222) 2438	(2.610E+01, 2.665E+01) 2.664E+01	(8.565E-04, 8.411E-04) 8.507E-04	(3.693E-10, 3.533E-10) 3.483E-10
80.00 SEED=	4.297E+01 3.039E+11	(1692, 1513) 3085	(2.969E+01, 2.690E+01) 2.502E+01	(0.867E-04, 7.819E-04) 7.892E-04	(3.022E-10, 3.999E-10) 3.110E-10
90.00 SEED=	1.576E+01 5.052E+11	(1832, 1777) 3510	(2.685E+01, 2.536E+01) 2.510E+01	(7.735E-04, 7.766E-04) 7.745E-04	(2.793E-10, 2.947E-10) 2.413E-10

FINAL VALUE OF SEED=   .56036017

Appendix C

Surface Scattering Program

GUERAP, the General Unwanted Energy Rejection Analysis Program, which was modified and used to model the different chambers and materials for surface scattering predictions, is too long (3500 statements) for a listing to be included. Certain additions have been made to increase the utility of the program for the present situation and the namelist titles and parameter names have been changed for the USU version which has been given the acronym RECAP for Radiation Energy Component Analysis Program. The basic format and techniques remain very similar to the original, however, and the reader can also understand RECAP by reading the documentation for GUERAP (Chou, 1972).

The input data used for the REAL model and the most significant portions of the output for this model are presented so that the reader can gain a more complete understanding of the capabilities of this program. The next two pages are input data, Table C-1 on the third page presents the angular ray count and energy distribution for model REAL, and other significant output data are summarized on the fourth page. Figures C-1 and C-2 are included to show the correspondence between the surface numbers described in the computer input data and the model configuration.

98

SCORE TEST WITH NONPERFECT SPECULAR SURFACES.
PRACTICAL IMPLEMENTATION USING MEASURED REFLECTANCES.

FILE NAME IS DATA/SCRREAL

ENDT1
1234567.

&BASICS
DELTAE 1.E-13, DEPRT=1.E-10, LRNF=7,   LEMIT=500,
NPRINT = 10,   NSEC   1,   RMAP 1.0,   WAVEL=.5,
ISPNT = 20,   ISEXT 31,   HAFOV =90.,   DIVANC=.1,
RINCR = .5,   ISTEPS =25,
&END

&DIFRCT &END

&GEOM IPLANE(1)=1,3,4,6,7,10,12,13,31,20,
IPLANE(11)=21,32,34,14,15,16,17,30,
ICONE(1)=2,5,8,9,11,33,18,19,22,
PL(1,1)=-10.5,0,0,1,0,0,5,
PL(1,2) -10.5,0,0,-22.5,0,0,5,5,
PL(1,7) -49.5,0,0,1,0,0,60,
PL(1,6) 42,0,0,-1,0,0,60,
PL(1,5)= 42,0,0,-49.5,0,0,60,60,
PL(1,4)= 37.5,0,0,-1,0,0,60,
PL(1,3)=-37.5,0,0,1,0,0,60,
PL(1,10)= 4*0,1,0,80,
PL(1,9)= 37.5,6,0,-37.5,6,0,37.625,37.625,
PL(1,8)=37.5,-6,0,-37.5,-6,0,37.625,37.625,
PL(3,11)= 50,0,0,-50,2.25,2.25,
PL(3,12)= 37.462,0,0,-1,2.25,2,
PL(3,13)= -37.462,0,0,1,2.25,
PL(1,14)= 37.5,0,0,1,0,0,60,
PL(1,15)= -37.5,0,0,1,0,0,60,
PL(3,20)= 37.462,0,0,-1,2,
PL(1,21) -22.5,0,0,-1,0,0,5,
PL(1,22)= -22.5,0,0,-49.5,0,0,2,5,
PL(5,31) .7071,.7071,1,
PL(5,32)= .7071,.7071,2.125,1,
PL(5,33) -11.314, -11.314,2.125,2.125,
PL(2,34)= -11.314,-11.314,0,-.7071,-.7071,2.125,
PL(2,30) 2.121,2.1213,0,.7071,.7071,100,
PL(1,16)= 42,0,0,-1,0,0,60,
PL(1,17) -49.5,0,0,1,0,0,60,
PL(1,18) 37.5,-6,0,-37.5,-6,0,37.625,37.625,

```
PL(1,19)  37.5,6,0,-37.5,6,0,37.625,37.625,
&END

&CNSTRT   NSTRT(1)   1,2,0,0,0,1,1,5,5,
NSTRT(10)  0,0,2,1,5,5,1,1,5,5,1,1,2,
NSTRT(30)  0,1,2,2,1,
KSIDSP(1,6)   30,                 KSIDSP(1,7) = 30,
KSIDSP(1,8)   4,3,30,10,11,       KSIDSP(1,9)   4,3,30,10,11,
KSIDSP(1,14) = 5,8,9,18,19,       KSIDSP(1,15) = 5,8,9,18,19,
KSIDSP(1,16) = 30,                KSIDSP(1,17)   30,
KSIDSP(1,18) = 4,3,30,10,11,      KSIDSP(1,19)   4,3,30,10,11,
KSTRT(1,6)    2,                  KSTRT(1,7) = 2,
KSTRT(1,8)    2,2,2,1,4,          KSTRT(1,9)   2,2,2,2,4,
KSTRT(1,14)   3,4,4,4,4,          KSTRT(1,15)   3,4,4,4,4,
KSTRT(1,16)   1,                  KSTRT(1,17) = 1,
KSTRT(1,18) = 2,2,1,1,4,          KSTRT(1,19)   2,2,1,2,4,
&END

&SYSTEM   NSFACE(1)   19,
ISFACE(1,1) = 9,18,8,19,16,17,6,7,13,31,32,33,
ISFACE(13,1)   1,5,14,15,2,12,20,21,22,34,
ISFTP(1,1) = 9*5,2,                ISFTP(11,1)   8*5,1,3*5,
KCOEF(1,1)   4*0,9*1,              KCOEF(14,1) = 3*0,6*1,
IMPSF(1,1)   1,                    IMPSF(3,1) = 1,
IMPSF(7,1) = 1,                    IMPSF(8,1)   1,
NIMPS(1)   1,          IMPORT(1,1)   31,          NRING = 5,
&END

&SURFCE
COAT(14,8)   32.99,2.845,          COAT(14,9)   32.99,2.845,
COAT(14,18)   32.99,2.845,         COAT(14,19)   32.99,2.845,
XCOAT(1,1)   .96324,.033,0,.00362,.00014,
XCOAT(1,2)   1,                    XCOAT(1,3) = .97,0,.03,
XCOAT(1,4) = .95,0,.05,
ICOAT(1,1)   8,9,18,19,            ICOAT(1,2)   5,14,15,13,
ICOAT(1,3)   1,2,7,12,17,21,22,32,33,34,
ICOAT(1,4)   6,16,
&END
EOF
```

108

Table C-1. Angular ray count and energy distribution on exit aperture for Model REAL.

Angle to normal (degrees)	Number of rays	Energy distribution
0.0 – 0.5	0	0.
0.5 – 1.0	0	0.
1.0 – 1.5	1	4.679 E – 15
1.5 – 2.0	1	6.211 E – 15
2.0 – 2.5	2	2.437 E – 12
2.5 – 3.0	2	2.771 E – 12
3.0 – 3.5	5	1.950 E – 11
3.5 – 4.0	2	8.463 E – 12
4.0 – 4.5	1	3.943 E – 12
4.5 – 5.0	1	3.649 E – 12
5.0 – 5.5	1	1.514 E – 15
5.5 – 6.0	4	2.987 E – 11
6.0 – 6.5	5	1.612 E – 11
6.5 – 7.0	8	1.392 E – 11
7.0 – 7.5	9	4.665 E – 11
7.5 – 8.0	10	1.838 E – 11
8.0 – 8.5	7	1.376 E – 11
8.5 – 9.0	5	7.986 E – 12
9.0 – 9.5	9	1.641 E – 11
9.5 – 10.0	6	1.711 E – 11
10.0 – 10.5	4	2.803 E – 12
10.5 – 11.0	5	7.482 E – 12
11.0 – 11.5	10	1.939 E – 11
11.5 – 12.0	4	5.166 E – 12
12.0 – 90.0	3348	3.277 E – 8

Significant computer output for Model REAL

Number of rays entering   500

Rays and energy through entrance aperture   6   1.800 E − 3

Rays through exit aperture   (1699, 1751)   3450

Energy through exit aperture   (3.768 E − 8,   2.837 E − 8)   3.303 E − 8

Attenuation   (6.635 E + 6,   8.811 E + 6)   7.570 E + 6

Rays not counted due to rays being ouside 90.00 degree fov or inside
the 0.100 degree divergent angle and their total combined energy

       Number of rays = 91   Total energy not counted = 91.0

Off-axis rejection   3.028 E + 7

Ranges for 90 percent confidence

     Standard deviation/(sqrt(N) average)   0.236

     Range of energy reaching target   2.524 E − 8   to 4.081 E − 8

     Range of attenuation   6.126 E + 6   to 9.904 E + 6

Maximum number of rays stored   18
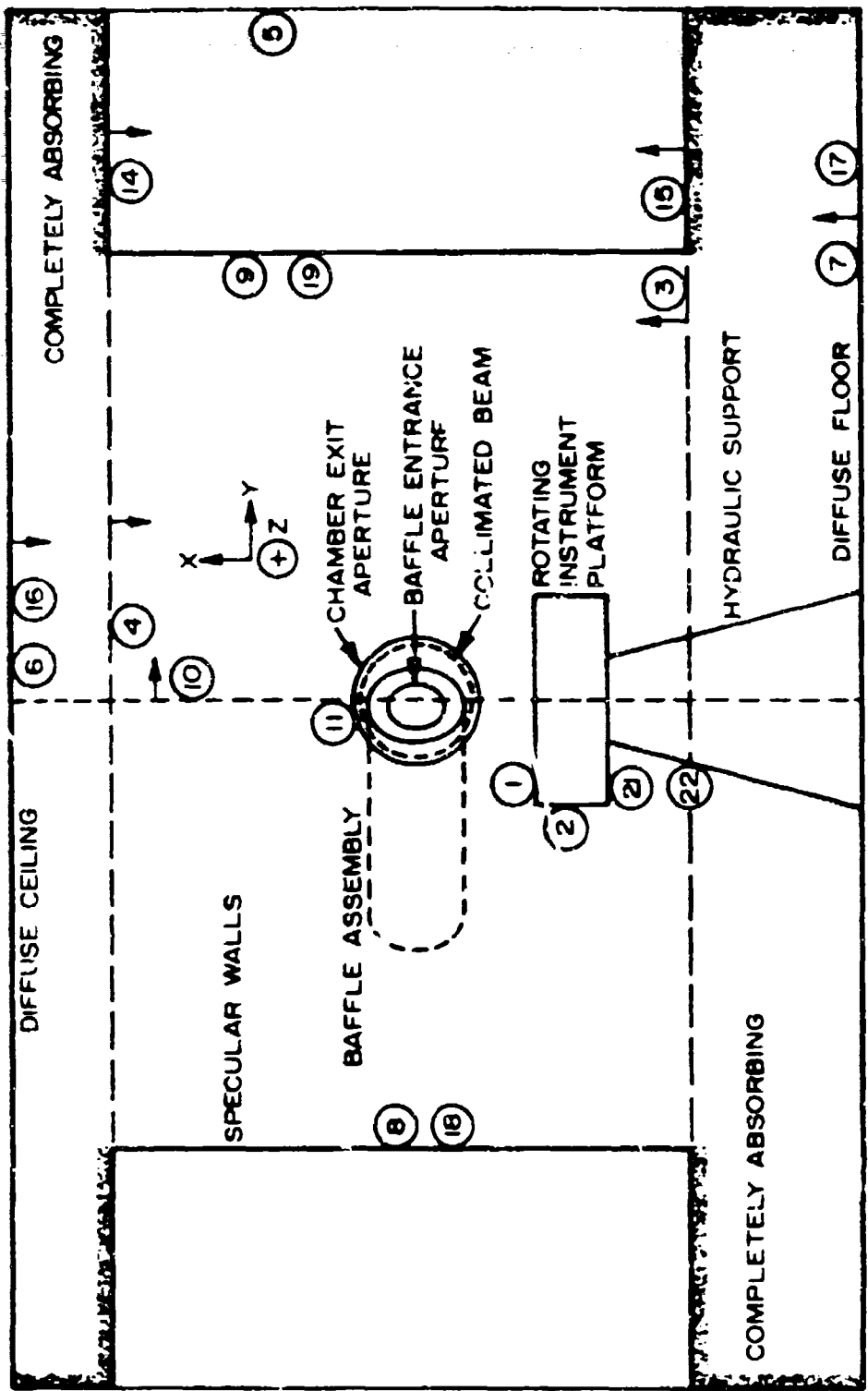
Figure C-1. Side elevation of Model REAL; the circled numbers correspond to surface numbers in the computer model.
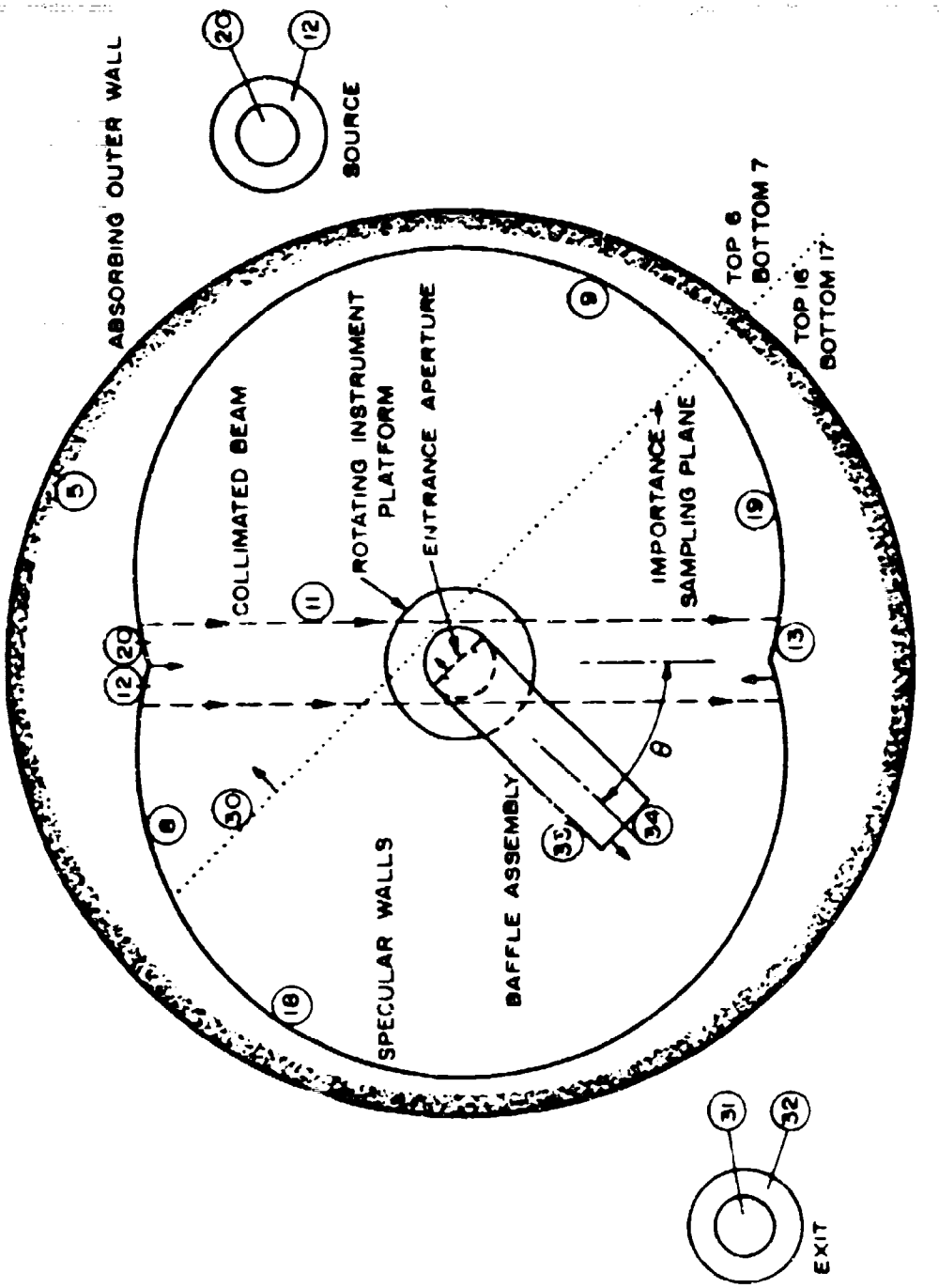
Figure C-2. Horizontal cross section of Model REAL.

Appendix D

Measured Reflectance Characteristics

The reflectance characteristics of the various materials used in the chamber construction were measured to obtain values to characterize the materials for the computer evaluation of the surface scattering effects. The measurement technique is described and the results are presented. The conversion of the measured values into hemispherical reflectance values is discussed and finally the special modeling of the near specular reflectance of the black specular plastic is given.

A special fixture was made to hold a flat material sample at the axis of rotation of the instrument platform independently of the platform motion. The sensor was moved to the rear of the instrument platform, 54 cm from the center of rotation and the on-axis response was measured as a reference before the sample was installed. The instrument platform was then rotated 175° from the on-axis position so that the sensor was viewing the illuminated portion of the sample, and the sensor was rotated about the fixed sample to measure the angular variation of the scattered power.

The results of these measurements are plotted in Figure D-1, where the scale refers to decibels below the on-axis incident power. The radiation was normally incident to the flat samples, and the angles are measured with respect to the incident radiation. The sensor baffle blocked the illuminating source close to on axis so that measured results are not directly available for this angular region. Several interesting facts are apparent from this figure.

The 3M "Nextel" Black Velvet Coating is very uniform in response out to about 70° away from the normal, indicating that this surface is very diffuse with incident radiation being scattered very uniformly over a large angle. The black shag carpet is much more absorptive than the black paint, (the angular non-symmetry is attributed to the nap direction of the carpet). The specular nature of the black plastic is very apparent. The black plastic is less reflective than the black paint for angles greater than 10°; for angles greater than 45° the
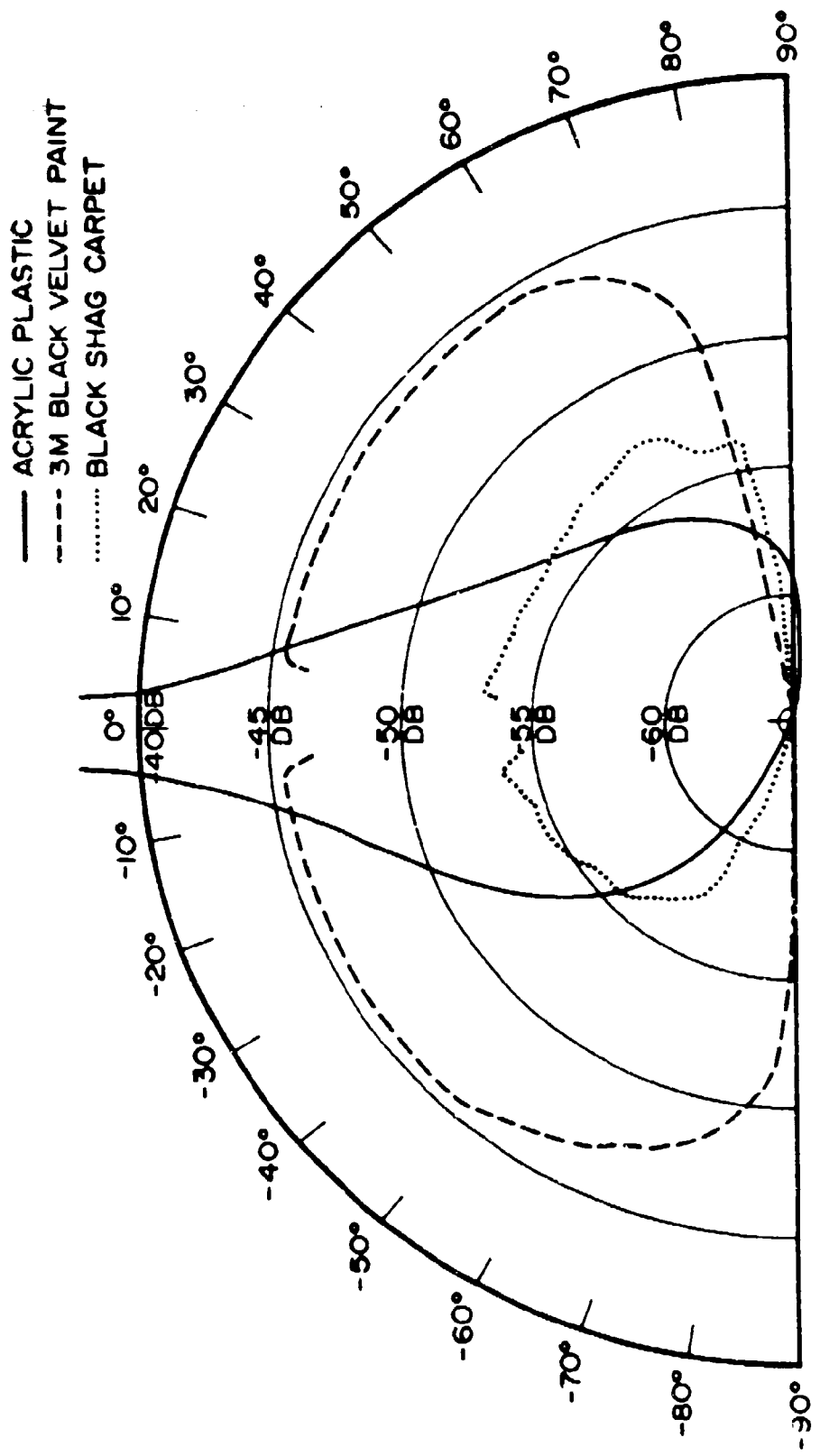
REFLECTANCE OF VARIOUS BLACK MATERIALS
(Decibels below incident power)

Figure D-1. Measured reflectances of the various black materials used in the chamber construction.

105

scattered radiation is even less than that of the shag carpet. The specular peak is not better angularly resolved because of the 5° angular width of the measuring optical system. The white cardboard used in the measured evaluation was also measured but its response was only 30 dB below the incident level and it does not fit on the scale chosen for the figure.

On axis, the sensor is responding to the source areance E,

$$dP_i = dE_i A_c \quad , \quad \text{(watts)} \tag{D-1}$$

where A_c is the area of the collector aperture. When the baffle is measuring the scattered energy, the sample appears as an extended source which fills the field of view and

$$dP_r(\theta) = dL_r(\theta) A_c \Omega_c \quad , \quad \text{(watts)} \tag{D-2}$$

where $L_r(\theta)$ is the apparent sterance of the extended source and Ω_c is the solid angle field of view of the sensor.

The ratio of the off-axis scattered response to the on-axis incident response is

$$R(\theta) \quad \frac{dL_r(\theta) A_c \Omega_c}{dE_i A_c} = \frac{dL_r(\theta) \Omega_c}{dE_i} \quad . \tag{D-3}$$

But $dL_r(\theta)/dE_i$ is the "bidirectional reflectance-distribution function" of Nicodemus, (1970), or the "reflection function" of Kasten and Raschki (1974) for normal incidence.

The hemispherical reflectance for normal incidence is obtained by integrating the reflection function over all reflection directions

$$\rho \quad \int \frac{dL_r(\theta,\phi)}{dE_i} \cos \theta_r \, d\Omega_r \quad , \tag{D-4}$$

where the integration is carried out over the full hemisphere. The measurements assume that the reflection characteristics are radially symmetric so that Equation (D-4) can be written as

$$\rho = 2\pi \int_0^{\pi/2} \frac{R(\theta)}{\Omega_c} \cos \theta \, d\theta \qquad . \qquad (D\text{-}5)$$

The hemispherical reflectances for normal incidence for the various materials measured were calculated by numerically integrating Equation (D-5) using the measured values for $R(\theta)$ and with $\Omega_c = 5.005 \times 10^{-3}$ sr as determined by previous measurements. The values of $R(\theta)$ were assumed to be constant over the region $-10° \leq \theta \leq +10°$ at the value of $R(10°)$ for the black paint and the black shag carpet. A special measurement was made to determine the shape of the response for the black plastic in the near specular region. The specular sample was illuminated at $20°$ away from the normal and the shape of the response in the near specular region was measured. The broadening effect of the wide measuring field of view was artificially removed and the response was allowed to peak in the specular direction.

The calculated values were corrected for the effects of the non-uniform source areance over the measured area to obtain the following reflectances:

3M black velvet paint	$\rho = 0.0268$
white cardboard	$\rho = 0.703$
black specular plastic	$\rho = 0.00958$

The values for the 3M black paint and the white cardboard are close to those obtained by others (Wilson and Wade, 1974), indicating that the technique and calculations are valid. The low value for the black specular plastic is indicative of the effectiveness of this material as a low reflectance wall covering.

A diffuse reflection coefficient of 0.03 was used for the diffuse surfaces modeled for the computer study; this allowed an absorption coefficient of 0.97. The specular surfaces require detailed modeling of the near specular reflection

characteristics. The measured specular response with the sensor broadening removed was plotted on semilog paper and then approximated by the sum of two exponential functions (straight lines on semilog paper). The coefficients of these exponentials (relative response versus radian angle) were used as the first two near specular components in the computer model.

The response curve as modeled above is sufficiently broad that it is not necessary to include a separate diffuse reflection coefficient for the black plastic. The specular component was measured to be 0.033 of the incident areance. The absorption coefficient of the black plastic was calculated to be 0.96324.